AN EXPERIMENTAL STUDY OF THE TURBULENT TRANSVERSE JET

Thesis by

David M. Kuzo

In Partial Fulfillment of the Requirements
for the Degree of
Doctor of Philosophy

California Institute of Technology

Pasadena, California

1996

(Submitted 6 October 1995)

Acknowledgement

This work was supported by the Office of Naval Research, grants N00014-93-1-1137, and N00014-91-J-1610.

ABSTRACT

An experimental study that examines the mean flow properties of the turbulent transverse jet using Digital Particle Image Velocimetry (DPIV) is reported.

This study examines various jet flows over a range of Reynolds numbers based upon jet velocity and diameter. Within this range it is documented that mean flow fields, identified as alternate mean flow states, other than the symmetric vortex pair exist. These alternate flow states are characterized by unsteadiness, asymmetry, and multiple streamwise vortices. Flow visualization shows that these alternate flow states are formed during initial jet roll-up, and persist far downstream without developing into the (expected) vortex pair. A map of the domain of existence, in velocity ratio - Reynolds number space, of these alternate states is provided, and a discussion of the underlying physics is included.

With this new understanding, selected symmetric jet flows at velocity ratios of 5, 10, and 20 are generated and studied using DPIV. The mean flow is quantified through measurements of vortex circulation, size, and impulse, and the relationship of these properties to the (initial) jet momentum flux is examined.

Table of Contents

Table of Contents

List of Symbols

A	Area, with the following particular subscripts: A_{jet} -- area of jet orifice, $A_{computation}$ -- the area over which a DPIV displacement vector is resolved, A_{plenum} -- area of jet plenum, see figure 3.
C	Indicating evaluation of a line integral about a closed contour.
D	Global length scale, defined in equation (2), page 4.
d	Jet diameter. *Also used to express differential in integral - differential expressions.*
I	Impulse, see page 45.
Jet Momentum Flux	Defined in equation (1), page 3.
L	Jet tube length, see figure 3.
R	Vortex equivalent radius, with the following particular superscript: R^* -- a reference area.
r	Radius.
Re	Reynolds number, with the following particular subscripts: Re -- *(unsubscripted)* based upon momentum-averaged jet velocity and d, Re_x -- based upon freestream velocity and boundary layer length.

Symmetry Parameter	Ratio of circulation of positive and negative vortices.
S	Vortex separation determined by peak vorticity, see page 35.
S*	Vortex separation determined by vorticity centroids, see note page 35.
u	Velocity, with the following particular subscripts: u_{jet} -- the momentum - averaged jet velocity, see page 3, u_∞ -- the freestream velocity.
Velocity Ratio	Ratio of momentum - averaged jet velocity to freestream velocity.
V	Maximum velocity in the cross section, see page 37.
v, w	Velocity components along Y - and Z - axes, respectively, with the following particular super/subscripts: v_o , w_o -- mean velocity, v' , w' -- perturbation velocity.
X, Y, Z	Coordinates for describing jet flow, defined in figure 1, with the following particular subscripts: Y_o , Z_o -- locations of vortex centers in the cross section.
Δ	A (flow) length, used on page 15.
δ	Differential.
ι	Elemental arc length in integral equation (3), page 29.
ν	Kinematic viscosity.

ω Vorticity, the curl of the velocity field.

ρ Density, with the following particular subscripts:
ρ_{jet} -- density of jet fluid,
ρ_∞ -- density of freestream fluid.

Γ Circulation, defined in equation (3) page 29, with the following particular super/subscripts:
Γ_o -- circulation at infinite value of equivalent radius, see page 31,
$\overline{\Gamma_o}$ -- circulation average (of absolute value) of positive and negative vortices.

Chapter 1
Introduction

This thesis reports on an experimental program undertaken at *GALCIT* - the *Graduate Aeronautical Laboratories (at the) California Institute of Technology*. This study was directed at furthering the understanding of the basic flow field of the turbulent transverse jet. It represents a small contribution to the focused effort at GALCIT directed towards the physical understanding of basic fluid flows such as jets, wakes, mixing layers, and boundary layers.

The transverse jet flow, the flow resulting from a momentum jet issuing perpendicular to a uniformly flowing stream is shown in figure 1. A similar flow is that of smoke issuing from a smokestack on a windy day, from which it is observed that the smoke quickly bends over in the breeze and is carried along by it. Although this example is not strictly a momentum-driven flow, the qualitative features are similar.

This flow has been studied scientifically throughout this century, and is presently a focal point for aerodynamic studies of aircraft, cooling applications, and combustion technology. Some of the earliest studies include those of Callagan & Ruggeri (1948), Ruggeri *et al.* (1950) and Jordinson (1956). A recent AGARD Meeting and Proceedings (1993) attest to the continuing interest in this flow field.

The coordinate system for describing the flow is shown in figure 1. Initially, the jet issues into the flowing stream along the positive Y - axis. As the flow bends over and begins convecting with the freestream, the jet traces out a path in the X - Y plane

called the jet trajectory. At the same time the flow spreads laterally in the Z - and Y - axis directions. The view in the Y - Z plane is referred to as the jet cross section.

From the earliest studies it was apparent that the striking feature of this flow was its vortical nature. Like a vortex ring created by a momentum puff, the transverse jet generates a vortex pair whose axis, far downstream, is approximately parallel to the X - axis. Many studies of the transverse jet focus on the behavior seen in the cross section. This is so because the effect of the transverse jet, namely a force acting on the flowing stream, produces a steady vortical motion in the cross section. Experimentally this feature has been noted by Kamotani & Greber (1972), Durando (1971), and Broadwell & Breidenthal (1984), while theoretically it has been described by Abrahmovich (1963), LeGrives (1977), and Snel (1974) as well as a host of other works.

Since these first insights into the flow, the richness and subtlety of this phenomenon have been made evident. Judging from smoke or dye visualization the transverse jet appears to be concentrated only in that region marked by the tracer, called the jet body in figure 1. Starting with the work of McMahon *et al.* (1964) and others, however, it became evident that there is a vortex shedding-like phenomenon which develops at the origin of the transverse jet, resulting in a *vortex array* which co-exists with the main body of the jet. Sometimes referred to as the vortex wake or jet wake, see figure 1, it is now appreciated that this vortex array resides in a narrow region centered about the plane Z = 0, and extends from the plane Y = 0, to the outer boundary of the jet body (Kuzo & Roshko 1984), the implication being that the jet flow is not simply that region traced-out by the jet body. Instead, the jet region spans from the bounding wall to the outer boundary of the jet body. Flow visualization reported by Kuzo & Roshko (1984), reproduced in figure 2, illustrates the extensive

nature of this vortex array. The sources of vorticity for, and the frequency of formation of these vortices are issues which are currently the focus of research activity (*e.g.*, see Fric & Roshko 1994).

The dynamic parameter characterizing this flow is the Jet Momentum Flux. Dimensionally equivalent to the transverse force, per unit time, acting on the flowing stream, this quantity is defined as

$$\textbf{Jet Momentum Flux} \equiv \int_{A_{jet}} \rho_{jet} \; u.u \; dA \tag{1}$$

where u is the jet velocity, ρ_{jet} is the density of the jet, and A is an area with A_{jet} in particular the area of the jet. From this definition, a *momentum - averaged* jet velocity, $\mathbf{u_{jet}}$ can be defined as,

$$\rho_{jet} \; u_{jet}^{\,2} \; A_{jet} \equiv \int_{A_{jet}} \rho_{jet} \; u.u \; dA$$

While the flow behavior near the origin may depend upon the boundary conditions, such as jet geometry and the state of the boundary layers, far from the origin the flow can be described in terms of this transverse force (Broadwell & Breidenthal 1984). A global length scale (**D**) can be defined from the ratio of the Jet Momentum Flux and the freestream momentum flux density as,

$$D^2 \equiv \frac{\int_{A_{jet}} \rho_{jet} \; u.u \; dA}{\rho_\infty \; u_\infty^{\,2}}$$

or, using the momentum-averaged jet velocity,

$$D \equiv \frac{u_{jet}}{u_\infty} \left(\frac{\rho_{jet}}{\rho_\infty}\right)^{1/2} A_{jet}^{1/2} \tag{2}$$

where u_∞ and ρ_∞ are the velocity and density of the freestream. Expression (2) introduces the **Velocity Ratio** as

$$\text{Velocity Ratio} \equiv \frac{u_{jet}}{u_\infty} \quad .$$

The flow will also depend upon the Reynolds number, the ratio of inertial to viscous forces in the flow. For this study, the Reynolds number, **Re**, will be defined as

$$\text{Re} \equiv \frac{u_{jet}\, d}{\nu}$$

where ν is the kinematic viscosity of the freestream and d is the jet diameter of the issuing jet, *i.e.*, $A_{jet} = \pi/4\, d^2$. This is the commonly defined Reynolds number for the ordinary jet, an axisymmetric jet issuing into a quiet surroundings. The local Reynolds number, based upon local velocity and length scales of the transverse jet, decreases as the flow evolves (Broadwell & Breidenthal 1984). As this local value of Reynolds number is difficult to measure, and since Re is related to this local value, Re will serve to characterize this flow.

All phenomena discussed herein are concerned with the flow field occurring far from the origin which, in practical terms, means after the jet flow has turned over and is being convected with the freestream. Following examples in the literature, the far field is usually defined as that region where the jet trajectory follows power-law behavior, see Pratte & Baines (1967). This power-law behavior in the jet trajectory is approximately realized once the flow has turned about 45° along the flowing stream, which occurs roughly at the streamwise location $X \sim D$.

As mentioned, this flow has been the interest of many studies, both experimental and analytical, over the course of this century. Yet, due to the inherent difficulties of geometry, progress in the experimental understanding of this flow has been slow. As in the ordinary jet, it is of interest to measure and understand the transfer of mass, momentum, and energy, to or from the surroundings.

The geometric difficulties are several. For one, the jet flow initially issues into the flowing stream transversely. Within a short distance, however, the body of the jet traces a path that tends to coincide with the direction of the flowing stream. In a short span of space the jet changes from issuing perpendicular to the flowing stream to being convected by, and moving on a trajectory nearly parallel to, the freestream direction.

A second geometric difficulty is encountered when defining what measurements are sufficient and adequate to characterize the flow. For the ordinary jet, from arguments of symmetry, the mean properties can be adequately measured along a diametric cut of the flow. This simplifies measurements of a three dimensional phenomenon to a two dimensional domain. The reader is referred to Townsend (1956). The transverse jet does not allow for such simplification. Although from arguments of symmetry the left half of the jet should be the mirror image of the right half in the cross section,

further simplification can become an unseen source of error, because the transverse jet flow is a three-dimensional phenomenon.

Beyond this three-dimensionality, an additional factor is present. Analytic descriptions of the transverse jet are typically given in terms of vorticity, the curl of the velocity field. Direct measurement of vorticity, although an active line of research, is not developed to the point that it is commonplace in the laboratory. To accurately compute vorticity from the velocity requires an accurate measurement of the two components of the velocity field, with the derived vorticity field results dependent upon the accuracy of the velocity measurement.

Digital Particle Image Velocimetry (DPIV), see Willert & Gharib (1991), a technique only recently made available, provides a way to determine the vorticity field of the transverse jet. Although a new laboratory technique, DPIV is now sufficiently mature to allow the experimentalist to overcome those difficulties described in the preceding paragraph. The technique, based upon imaging the motion of particles suspended in and following the flow, provides a measure of particle displacement during the imaging time. From this displacement, the velocity and vorticity fields are calculated by numerical techniques.

The present work is among the first to use DPIV to examine the transverse jet. The study was limited by the current state of the art of DPIV technology, with finite light-shuttering capabilities limiting temporal resolution and with the finite spatial resolution of CCD cameras imposing spatial limitations. Unique techniques had to be developed for a successful study of this flow, including imaging techniques for convecting flows.

This study measures several fundamental properties of the transverse jet, including the strength of the vortices characterizing the flow (as measured by circulation), and the size of these vortices. The impulse of these vortices is determined. All of these quantities have, in the past, been inferred from theoretical arguments. This work complements those studies with laboratory results.

Chapter 2
Experimental Details

The experiments, designed to provide mean and dynamic characteristics of the velocity and vorticity fields, were performed in water. Water as a fluid medium has a distinct advantage for DPIV as it facilitates a uniform dispersion of particles.

For this study, optics were immersed in the flow. Again, the water medium proved to be advantageous in that the water-proof optics successfully withstood prolonged immersion. A similar setup in air would probably be susceptible to optical contamination, resulting in degradation of the DPIV image and loss of accuracy.

2.1 Physical setup

A free-surface water facility, available at GALCIT and originally designed by M. Gharib (1983), was used for all DPIV measurements presented herein. This facility is a recirculating type with a total capacity of 4000 liters, with a test section 18 inches by 18 inches in cross section and approximately 5 feet in length. Driven by an in-line centrifugal pump, the speed of this facility was varied by adjustment of the DC current provided to the pump motor. Typical useful speeds are in the range of 8 - 60 cm/sec. Flow management devices located in the upstream contraction section helped break up and minimize freestream turbulence (see Gharib 1983 for measurement of freestream turbulence levels).

A surface plate was installed in the test section of the facility for the purposes of this study. This plate minimized difficulties with surface waves, and provided a known boundary condition for the injection geometry of the jet flow. With this plate, a flush-mounted jet injection geometry was used. Readers unfamiliar with the different wake phenomena occurring with flush injection and protruding injection are referred to McMahon *et al.* (1971).

The surface plate was made from a single piece of 0.5 inch plexiglas, see figure 1. The leading edge of this surface plate was machined with an elliptical shape of aspect 3 - to - 1 . This elliptical leading edge allowed for the flow transition from a free-surface flow to one bounded by a solid surface. Constructed to fit snug against the facility sidewalls, it was supported from the top by fourteen hangers attached to overhead hardware from the tunnel. The surface plate was securely fastened and became an integral part of the flow facility.

The surface plate was positioned such that the bottom surface of the plate, *i.e.*, that surface in contact with the water, closely followed the level traced out by the free-surface without the plate present. No geometric allocation was made for blockage effects created by the presence of the additional boundary layer on the surface plate.

Care was taken throughout the course of the measurements to insure that the free-surface was clean. As such, the boundary layer on the surface plate commenced at the elliptical leading edge of the plate.

The surface plate was provided with several access ports on the centerline, see figure 3. The first of these access ports, located 8 inches from the elliptical leading edge, was used for mounting of the jet tube.

The jet flow was generated by a separate facility. A pressurized supply was constructed for the purposes of providing a range of jet flow rates. The supply utilized the same fluid as the free-surface channel, *i.e.*, $\rho_{jet} = \rho_{\infty}$, with both drawn from the same supply. A stainless steel pressure vessel of 1 gallon capacity served as the reservoir for the jet supply. A gas driver, either compressed air for moderate pressure levels or compressed bottled nitrogen for high pressure levels, provided the flow rate and was applied to the top of this steel pressure vessel. The pressure was set by a regulator, and a constant bleed flow was maintained to insure efficient operation of the regulator, see figure 3.

Mindful that a blow-down facility of gas and water can experience oscillations, design efforts were expended to insure that these oscillations were minimized. The total volume of compressed gas used as a driver was kept at a minimum by using small, short tubing segments. The flow was controlled by a valve located in the liquid side of the reservoir, not the gas driver side. The entire system was highly damped. During system development a transducer was incorporated into the gas driver side and measurements showed that the oscillations rapidly decayed within one second.

The jet flow was switched off - on by a pneumatically operated valve at the discharge end of the pressure vessel. This pneumatic valve was operated by an electric solenoid such that the jet operation could be controlled by a preset timer, or could be operated manually using an electric switch. In operation the timer was used, allowing researcher attention to other (optical) details just prior to data acquisition. The timer could then be set to some limiting value such that the pressure vessel was never run to complete emptiness, which would allow air to exit the jet nozzle.

Downstream of this pressure vessel and master valve, the flow was delivered to

the test section using a flexible pressure hose. This hose had an internal diameter of 1 inch, a length of 10 feet, and was lined with teflon to facilitate chemical reaction experiments which were not part of the present investigation. This hose allowed the pressure vessel, related timing circuitry and controlling valves to be positioned at a convenient location in the laboratory.

The jet nozzles, which were tube stubs of very small length to diameter ratio, were attached to this delivery hose using a plenum. This plenum, also of 1 inch internal diameter, allowed for settling and transition of the flow to the nozzles via a 45° geometric contraction. The internal geometry of the plenum and nozzle is illustrated in figure 3. The nozzles used for this study are summarized in table 1. The jet nozzles were of such small dimensions that no effort was made to measure boundary layer profiles of the issuing flow. Instead the velocity profile was assumed to be a top hat profile, with u_{jet} taken to be equal to the mass flux averaged velocity.

$\mathbf{d}$ *inch*	$\frac{\mathbf{L}}{\mathbf{d}}$ †	$\frac{\mathbf{A_{plenum}}}{\mathbf{A_{jet}}}$ †
0.093	10.4	116.
0.191	5.71	27.4
0.30	3.85	11.1

Table 1. Nozzles used for jet flow.

† See figure 3.

During data acquisition, laboratory procedure followed the below order. The required flow conditions of Re and velocity ratio were determined by data requirements. This determination allowed for selection of the freestream velocity u_∞ and of the jet velocity. The jet velocity was set by adjusting the driver pressure. No flow regulation was done downstream of the pressure vessel. A calibration of total flow volume measured over a metered time was used to measure the jet velocity, with the freestream velocity measured using DPIV. With the jet and freestream velocities selected and set, attention turned to last minute details of flow conditions in the water channel. The upstream flow management devices, namely screen, perforated plates, and honeycombs, were thoroughly inspected for the presence of unwanted blockages and obstructions. With this assured, attention turned to identification and removal of any unwanted obstructions in the test section. These later obstructions were, for the most part, air bubbles trapped beneath the surface plate, but there was always the possibility of optical contamination on the sidewall and bottom which would have diminished optical acuity. Next, particle concentration and suspension in the facility were issues, with extensive effort given to assuring correct particle count levels. This level was set mostly by hands-on experience: too-small a particle count made for poor image correlation during processing, while too-high a count diminished image quality due to (light) scattering. Following all of these inspections and corrections (if necessary), sufficient time was allowed for the flow to become steady-state if a disturbance was created during any modification or correction. Once optimum conditions had been established, room lights and any other extraneous light sources were doused, and attention turned to the optical procedures for data acquisition.

As the above outlined procedure required several hours, it is clear that one data

set per day was the rule, with the remainder of the time spent in preparation or data processing.

2.2 Optical setup

Details of Digital Particle Image Velocimetry (DPIV) are described by Willert & Gharib (1991) and Willert (1992). Only details beyond those presented in these references are described herein. The particles used throughout this study were 10 μm glass spheres coated with silver ("Conduct-O-Fil" from Potters Industries Inc, Carlstadt, NJ). Illumination was provided by a Spectra Physics Argon Ion laser (model 95-3), with optics used to generate a thin sheet of light (sheet thickness estimated at 0.3 - 0.6 mm.).

Recorded images, from a NTSC camera, Texas Instruments multiCAM CCD (model 1134 P/GN), were recorded directly onto optical laser disks (Sony LVM 3AA0/3) using Sony Recorder-Processor LVR-5000A & LVS-5000A. The framing rate of the camera was the standard video rate 30 Hz., resulting in a temporal bandwidth of 15 Hz. (two frames for one displacement field measurement). The actual time separation between image pairs was specified by strobing the laser illumination source, which was accomplished using a blade-type beam chopper (NM Laser Products, Sunnyvale, CA).

DPIV processing involves the computation of two-dimensional displacement fields by cross-correlating spatial subsamples (windows) of adjacent images, resulting in the mean displacement vector for that particular subsample. Incrementally moving this subsample window throughout the entire image results in a displacement field (to the resolution of the sample window and increment) for the entire image. Division of

the displacement field by the selected time separation gives the velocity field associated with the two images.

Cross-correlating using Fast Fourier Transform (FFT) algorithms, displacement computation, and the calculation of the velocity and vorticity fields, were done using available software from the Center for Quantitative Visualization (CQV). For optimum performance, each region over which the FFT is performed requires a minimum number of particles. Since each (imaged) particle (optically) occupies one or more pixels of the digital image, it can be appreciated that the FFT computation area must be of a finite size. Realizing that present CCD technology is limited to approximately 10^6 pixels, and devoting 3 pixels per particle times 10 particles with a fifty percent image occupation ratio, then the FFT computation area is approximately 10^{-4} of the total imaged area. All results presented herein used a subwindow size of 32 by 32, with an increment of 8 by 8. The time separation between images was selected to optimize the cross-correlation between images.

The primary view of interest for this study was the jet cross section. Imaging this view for DPIV necessitated innovative techniques to insure good image correlation. Since image correlation required correlating patterns of particles in adjacent images, it was absolutely necessary that particles remain in the field of view for both images of the image-pair. Further, since the mean flow is convecting through (and out of) the image plane, the above requirement can be met, for a stationary illumination source, only for temporal separations less than the illumination thickness divided by the convection velocity. Such (short) temporal steps were inadequate for the present study because in such short time steps the particle displacement is typically much less than one pixel.

A novel technique was devised and used, for the first time in the course of this study, to successfully extend the time step to acceptable levels. By sweeping the light sheet source with the convecting flow during image pair acquisition, successful correlation was attained. Between image pairs the sheet location was reset in preparation for the next image pair acquisition. This is illustrated in figure 5. With the time steps involved, the total sweep stroke was less than 1 cm.

Imaging of the jet cross section was done by mounting a small (3 inch diameter) front surface mirror onto a stiff, streamlined support that was inserted into one of the instrumentation access ports of the surface plate (figure 3). With the plane of this mirror at 45° to the Y - Z plane, the imaging camera was located along the side of the facility, enabling a distortion-free image of the jet cross section.

Finite spatial resolution is expressed in practical terms in figure 6, which shows the spatial resolution for the measurements presented in chapter 4 and 5. Although DPIV provides information about particle displacements in the imaged plane, there are still limitations on its capabilities. In particular, the spatial resolution was inadequate to resolve the smallest turbulent scales in the flow -- the Kolmogorov scale. Following Hinze (1975), the Reynolds number of the flow is related to the ratio of the largest eddies of the flow and the Kolmogorov scale, *i.e.*,

$$Re^{3/4} \sim \frac{\Delta\, large}{\Delta\, Kolmogorov}$$

or, rearranging,

$$\Delta\, Kolmogorov = \Delta\, large\ \ Re^{-3/4}$$

and estimating that for the present measurements the largest scales, $\Delta\, large$, range in

value from tens to hundreds of jet diameters (increasing in value further downstream), while the (local) Reynolds number ranges from ten thousand down to one thousand (decreasing with downstream distance), it can be appreciated that the smallest scales can range from 0.001 d to 1 d -- a range several orders below that measured.

As already discussed, the primary emphasis of this study is the measurement of the jet vorticity field. Figure 7 shows a normalized histogram distribution of the vorticity levels in the freestream typical for all measurements presented in this work.

Chapter 3
Basic Flow Field Dynamics

An important aspect of the behavior of the transverse jet, illuminated during the course of this study, is discussed in this chapter. This aspect is the existence of mean flow fields which do not constitute a vortex pair -- an aspect that has not been previously reported in the research literature. A description of these alternate mean flow states is given in this chapter as well as a discussion of some distinguishing features.

The existence of these alternate states can be verified visually either by Laser Induced Fluorescence (LIF) or particle imaging, using a thin illumination sheet in the cross section. For a range of Re and velocity ratio values -- the parameter space for these alternate states -- the jet is not a vortex pair. Without a map of this parameter space, however, generating or even finding these alternate states is a tedious process.

To quantify this parameter space, DPIV analysis is used. Due to the vastness of this parameter space, it is not feasible to document all possible flow states. Rather, extensive DPIV data records (several thousand consecutive images in length) were analyzed for selected flow conditions. This data will be used to illustrate three features of these alternate flow states.

The first feature, *unsteadiness*, will be described using *loci plots*. A loci plot shows points of vorticity maxima/minima in the cross section. Although not providing as much information as a vorticity plot, loci plots will illustrate the dynamic nature, or unsteadiness, of these alternate flow states.[1]

[1] Unsteadiness, in the present context, is used to describe the varying spatial location of the vortices in different realizations of the flow.

Figures 8a and 8b are loci plots for jet flows of velocity ratio 10, each plot having a pair of points (different symbols are used to distinguish between positive vorticity maxima and negative vorticity minima) for each image pair of the data record. In figure 8b the characteristics of a vortex pair are seen. There is a segregation of positive vorticity maxima in the negative half-plane and negative vorticity minima in the positive half-plane with a symmetric distribution about Z/d = 0, and the points are locally concentrated.

Figure 8a shows quite a different distribution. In the top plot of figure 8a there is a migration of the maxima/minima points across the line Z/d = 0, resulting in an intermingling of negative vorticity minima where only positive vorticity maxima are expected, and vice versa. This migration results from a vorticity field that is unsteady. The lower plot of figure 8a, on the other hand, shows a strong segregation of points, but in an asymmetric distribution. *Asymmetry* is the second feature of these alternate flow states.

Since the velocity ratio is a constant in figures 8a and 8b, this unsteadiness and asymmetry is a function of Re only. A progression from unsteadiness to a steady vorticity distribution occurs as Re increases. During this progression in the value of Re the vorticity field can be asymmetrically distributed, and the vorticity distribution can be concentrated or dispersed.

The vorticity fields for these loci plots help explain these observations. For values of Re like those for figure 8b, the mean vorticity and velocity fields show a symmetric vortex pair. Figure 9 shows the mean vorticity and velocity fields for a flow corresponding to the top loci plot in figure 8b. The vortex pair is symmetric about Z/d = 0 (which was evident in the loci plot) and the accompanying velocity field

clearly shows the vortex pair. Figures 10a, 10b, and 10c are 1-second, consecutive realizations of the flow in figure 9. A turbulent character is evident in the fluctuating gradients, and a slight asymmetry about Z/d = 0 is seen, but the mean flow in figure 9 is relatively symmetric and steady.

Contrast this with figure 11, showing the mean vorticity and velocity fields corresponding to the top loci plot in figure 8a. The mean vorticity and velocity fields are seen to be asymmetric about Z/d = 0, and the vortex orientation is tipped. In addition, another vortex is seen in the cross section. This vortex has a lower trajectory, as indicated by smaller Y/d location of the vortex center, than the anticipated vortex pair. The presence of this additional vortex is a third feature of these alternate flow states, namely, the existence of *multiple vortices* (number of vortices exceeding the expected two) in the mean flow. Those vortices in excess of two will be called *tertiary vortices.*

Sequential 1-second flow realizations, shown in figure 12 a-c, for this flow show these multiple vortices in a striking manner, as numerous tertiary vortices are seen. In addition to showing turbulent characteristics, there is a dynamic shifting in the flow patterns between flow realizations. The flow field is essentially reorienting from side to side, and the unsteady nature of this flow can be appreciated. Unlike the flow in figures 9 and 10, the mean for this flow is not a symmetric vortex pair.

A small increase in Re generates a flow that is relatively steady yet highly asymmetric, as seen in figures 13 and 14. The 1-second realizations of figures 14 a-c again show the hallmarks of turbulence, but the unsteadiness characterizing the flow in figures 11 and 12 is notably absent. Further increases in Re beyond the value in figures 13 and 14 result in the highly symmetric and steady flow similar to those

shown in figures 9 and 10.

The asymmetry of these flow states can be quantified by forming the ratio of the circulation of the two vortices that would be (mistakenly) identified as the vortex pair -- namely those furthest out in the flow. To compute the value of circulation, measurement of which is discussed in detail in chapter 4, the 90% vorticity contour is used. The circulations measured for the data in figures 9, 11, and 13 are compiled in figure 15, along with the replotted mean vorticity contours.

Defining the **Symmetry Parameter** as (absolute value of) the ratio of circulations, and selecting the numerator/denominator to stay within the range

$$0 \leq \textit{Symmetry Parameter} \leq 1 \quad ,$$

calculations of this value for the flows in figure 15 are compiled in table 2.

	Symmetry Parameter	**Re**
Figure 9	$\frac{42.3}{43.5} = 0.97$	7250
Figure 11	$\frac{8.11}{12.19} = 0.65$	2079
Figure 13	$\frac{10.03}{25.33} = 0.40$	4371

Table 2. Computed values of Symmetry Parameter for velocity ratio 10 .

Similarly, Symmetry Parameter can be computed for selected 1-second realizations of these flows. When plotted, values of the Symmetry Parameter show a functional behavior with Re, as seen in figure 16, of a decreasing value of Symmetry Parameter with increasing Re until, at a *critical* value of Re, a dramatic jump to Symmetry Parameter ~ 1 occurs. Unsteadiness also varies with Re: approaching the critical Re the unsteadiness decreases while beyond critical Re the unsteadiness (relatively to those flows below the critical Re) is negligible.

Re	**d**	$\mathbf{u_{jet}}$	Re_x
	inch	$\frac{cm}{sec}$	
7250	0.093	307.	6.2×10^4
2079	0.093	88.	1.8×10^4
4371	0.093	185.	3.8×10^4

Table 3. Flow settings for demonstration of critical Re.

The tertiary vortices are also shown in figure 15, along with measurements of circulation for these tertiary vortices. In all cases the sum of the circulations is zero, suggesting that all of the identified vorticity comprises the jet flow and is not associated with boundary layer vorticity along the bounding surface at $Y = 0$.

A different definition of Symmetry Parameter, for example the ratio of the two strongest vortices in the cross section, would produce a different functional dependence than that shown in figure 16. This is of little consequence for the present

discussion.

Table 3 summarizes the flow settings for figures 9 - 14.

3.1 Extension to other velocity ratios

The aspects of these alternate mean flow fields, namely, *unsteadiness, multiple vortices, and asymmetry*, have been described, and measurements similar to those discussed above were made for velocity ratios at 5, 15, 20 and 25. Additionally, flow visualization studies were conducted for ratios as high as 55.

Because of the large parameter space involved, and the large effort required for analysis, it is not feasible to present all measurements in detail here. In all manners, the alternate flow states observed for these various velocity ratio values were similar **except** that the critical value of Re varies with velocity ratio. The findings are summarized in figure 17a illustrating the behavior of critical Re. Noteworthy is that the critical Re, for the range of velocity ratio studied, spans from several thousand to well above ten thousand.

The behavior illustrated in figure 17a is somewhat counter to intuitive reasoning. Since the strength of the jet vorticity is related to the strength of the issuing jet flow -- the force that generates these vortices -- the higher the velocity ratio, the stronger these vortices. The need for an increasing value of Re with increasing velocity ratio required to generate a symmetric flow therefore seems not to be a Reynolds number issue, but rather one of vorticity dynamics.

It is noted that the variation with velocity ratio seen in figure 17a collapses to a single curve when multiplying Re by the velocity ratio. This parameter, (Re)(velocity

ratio) = $u_\infty d / \nu$, the cross flow Reynolds number, has a critical value in the range 600 - 800 for the data compiled. This is illustrated in figure 17b. However, other observations made in this laboratory for jet flows generated by fully-developed pipe flow have a critical value of several thousand in this modified parameter, suggesting further study is required before a definitive critical value is specified.

A different perspective on the existence of these alternate states, in velocity ratio - Reynolds number parameter space in shown in figure 17b.

Very high values of velocity ratio are quite difficult to measure with accuracy in the laboratory. This latter restriction is of little importance for practical applications as there is no immediately obvious application for a jet flow of velocity ratio of several hundred. However, the limit of very high velocity ratio values has a theoretical implication that will be addressed in chapter 6 .

3.2 Underlying physics

A complete understanding of the physical processes underlying this noted behavior is beyond the scope of the present study. However, some observations are noteworthy.

Two related issues are considered: how does the jet, conceptually a symmetric phenomenon, choose sides; and, why are some jet flows asymmetric.

As noted, asymmetry occurs with random orientation, with the asymmetric flow patterns occurring with equal probability in either the plus or minus z-axis orientation. The jet Reynolds numbers, Re, on the order of tens of thousands, are well beyond the transitional Reynolds number for the ordinary jet (which is on the order of one

thousand). The Reynolds number of the boundary layer along the bounding surface, listed in table 3, is relatively constant and somewhat below the laminar-turbulent transition value. That evidence seems to indicate that boundary layer transition is not responsible for these observations.

Chapter 1 alluded to the many subtleties associated with the transverse jet, especially concerning the vorticity field near the point of injection, see Foss (1980) and Fric & Roshko (1994). This region involves vorticity generation, stagnation points, and possibly separated flow. Among these features is the presence of a horseshoe-vortex wrapping around the jet at the origin. It seems likely that asymmetries in this vortex may be responsible for side-selection of the asymmetry. What creates asymmetries in this horseshoe-vortex is not clear, nor is the sensitivity to freestream conditions clear. These boundary conditions contribute to the orientation of asymmetry, but probably not to the existence of asymmetry. The reason for the apparent splitting of vorticity in the cross section may have more to do with vorticity dynamics and impulse than boundary conditions, as evidenced by the behavior of critical Re with velocity ratio.

One may speculate why the existence of these alternate flow states, given the large number of studies of the transverse jet, has not been previously reported, even with some asymmetric behavior being evident in previously published results.

One reason may be the difficulty in noting this asymmetry. It has been observed during this study that only small concentrations of initial jet fluid are seen in these tertiary vortices. Also the flipping from side-to-side of some of these flow states makes flow-seeding for visualizing difficult. Only with the selective viewing capabilities of LIF or DPIV is it easy to note these alternate states. Because of the distant proximity

of these tertiary vortices from the expected vortex pair, studies using point measuring techniques tend to not cover the regions occupied by tertiary vortices. Indeed, even with a field measurement capability like DPIV, the critical necessity of measuring in the entire cross section had to be realized (and it was).

The assumption that the flow field must be a vortex pair probably hindered many studies. Most cases of jet visualizations using smoke or dye show such complexity that the ability to see a vortex pair underlying this complexity is highly questionable. Even more misleading, when observing highly dispersive flows, such as steam-laden stacks in an atmospheric wind, much of the highly mixed stream evaporates, leaving only a skeleton-like remnant of those parts of the jet that are not so energetic. It may be for these reasons that the vortex array remained obscured for so long.

Reporting of flow field asymmetry might well have occurred earlier had previous studies noted irregularities seen in the cross section. Figure 18 shows flow visualization in the cross section from early exploratory work showing an unsteady asymmetric flow state illustrating that these alternate states are detectable in the cross section. Comparison is invited between the images in figure 18 and the unsteady, asymmetric flow state shown in figures 11 and 12 a-c.

It is also possible to detect these states from the side view. These alternate states show an early roll-up of vorticity as the jet issues transversely to the flow, an example is shown in figure 19. This early roll-up means that these tertiary vortices are formed first, followed by roll-up of the vortex pair. Apart from this aspect, no marked change in mean jet behavior was noted. No experimental evidence was obtained that these tertiary vortices merge with the vortex pair at some later downstream location.[2]

[2] The tertiary vortex in figure 19 has moved out of the plane of illumination further downstream.

Chapter 4
Mean Vorticity Measurements

As discussed in chapter 1, the transverse jet is usually described in terms of the vorticity field. This chapter will present measurements of the vorticity field for transverse jet flows at various velocity ratios and streamwise locations. Efforts were made to insure that these measured flows were steady, symmetric mean flow states.

Previous measurements of mean vorticity have been reported by Moussa *et al.* (1977). These measurements, however, were very near the origin, before the jet flow had aligned with the freestream direction.

Three velocity ratios are presently examined, those of 5, 10, and 20 (nominal values). The flow settings are listed in table 4 .

Velocity Ratio	**Re**	$\mathbf{u_{jet}}$ $\frac{cm}{\text{sec}}$	**d** *inch*
5	6138	80.6	0.30
10	9993	206.	0.191
20	13,087	554.	0.093

Table 4. Flow settings for vorticity measurements.

For each setting of the velocity ratio in table 4, several streamwise locations were measured. These streamwise stations are tabulated in table 5.

Velocity Ratio	**X** *inch*	**X/d**
5	5.5	18.3
	12.25	40.8
	22.25	74.2
10	5.5	28.8
	9.4	49.2
	16.5	86.4
	21.375	112.
20	6.85	73.7
	10.7	115.
	17.75	191.
	22.625	243.

Table 5. Streamwise locations of cross section measurements.

The mean vorticity fields for these measurements are shown in figure(s) 20 as contour plots, with the spatial variables normalized by the jet diameter. The vorticity in each plot is normalized by the maximum (absolute value) vorticity, with the contours shown in 5% increments. Ideally, each vortex would show the same number of contours.[3] However, a lack of symmetry was often seen between the positive and negative vorticity distributions. This lack of symmetry is manifested in the peak vorticity level for the positive and negative vortex, shown in figure 21. Here it is seen, for

[3] Each vortex would show 19 contour levels, the 20^{th} level usually only shows as a point.

example, that for a velocity ratio of 20 the maximum vorticity for the positive vortex is always higher than the negative vortex, with the result that in figure 20c there are more contours for the positive vortex (shown as dashed curves) than for the negative vortex (shown as solid-line curves).

This lack of symmetry is due to the fact that the values of Re for these flows is only slightly higher than the critical Re, with the result that the flow retains a slight propensity to generate tertiary vortices. The presence of these tertiary vortices, evident in the instantaneous vorticity fields, accounts, for example, for the notable elongation of the negative vortex in figure 20c. As described previously, the side on which these tertiary vortices occur is driven by the boundary conditions of the flow. These boundary conditions varied from day to day and, as a result, on one day for velocity ratio 20 the positive vortex has higher vorticity levels, while on another day for velocity ratio 10 the negative vortex had higher (absolute) vorticity levels.

It would have been desirable to use flow settings that far exceeded the critical Re for the given velocity ratio, thereby producing highly symmetric flow fields (and presumably the asymptotic flow states for the transverse jet as Re tends towards infinity). However, the upper limit of Re that could be resolved by DPIV was limited by the available hardware. The present results were the maximum values of Re that could be resolved with current DPIV technology.

In spite of this slight lack of symmetry, the results in figure(s) 20 show many of the expected characteristics of a vortex pair. The vortices are well defined, with a sharp separation along the midplane at Z/d = 0. As will be pointed out later, in figures(s) 20 one can note the turbulent growth of these vortices, as well as the jet trajectory. These features will clearly illustrate, in a qualitative manner, the flow evolv-

ing as expected for a turbulent vortex pair.

In general, the contours in figure(s) 20 are quite smooth and regular. However, at the furthest streamwise stations this smoothness somewhat degrades. At these stations the vorticity, especially at the lower contour levels, is comparable to freestream levels of vorticity (see figure 7), and it is presumed that this degradation is due to freestream turbulence.

4.1 Measurement of circulation

A primary goal of this study is to measure vortex circulation -- the strength of the vortices. This measure and information of its dependence on the jet parameters is of value in understanding the overall behavior of the jet.

Circulation can be determined from either the vorticity or velocity field as

$$\Gamma \equiv \int_A \omega \, dA \equiv \int_C u \cdot d\iota \quad . \tag{3}$$

Using the area integral in (3), it is of paramount importance to select the proper and adequate area over which the integration is performed. It has already been noted that the vortex is diffuse, and that there is ambient vorticity in the freestream. These factors contribute to the difficulty in measuring circulation, since it is necessary, for a correct measure, that the integration area contain all of the vortex while excluding any freestream contributions. Additionally, the integration area should only include one vortex of the pair, as integration over the whole cross section would be zero.

With these cautions, and mindful of the intricate contour patterns in figure(s) 20,

it is natural to utilize an integration area that coincides with the lowest vorticity contour of a vortex. Yet this is not a feasible approach, since the lower vorticity contours are corrupted by freestream turbulence.

To circumvent this difficulty, a construction is utilized in the following manner: the integration is done over successively larger vorticity contours for each vortex. Doing so, an interesting and useful feature is noted, see figure 22: the measured circulation is proportional to vorticity[4]. That is,

$$\Gamma \mid_{\omega} = \int_{0}^{A} \omega \, dA \quad \propto \quad \omega$$

or

$$\frac{d\,\Gamma}{d\,A} \quad \propto \quad \Gamma \quad ,$$

indicating an exponential functional dependence of circulation on integration area[5]. Solving and applying boundary conditions, it is seen that this functional behavior is,

---

[4] Caution is used in fitting a line to these points. At low levels of vorticity, (unwanted) contributions from the freestream can be anticipated, and these points may not fall along the line.

[5] This can be seen by taking the differential of the above integral expression: i.e.,

$$\bar{\omega} \; \delta A \quad \propto \quad \delta\omega$$

mindful of the mean value theorem of Calculus. Alternatively, it can be understood going in the reverse direction:

$$\Gamma(r) = \pi \int_{0}^{r} \omega \, dr^2$$

$$\Gamma(\omega) = \int_{0}^{\omega} \omega' \frac{dr^2}{d\omega'} \, d\omega'$$

$$\Gamma(\omega) = \omega \frac{dr^2}{d\omega} = const.$$

$$\Gamma \sim 1 - e^{-A} \quad .$$

It is evident from figure(s) 20 that these vortices are not circular. Rather, the shape of these vortices is elongated in the Y/d direction. It has already been noted that some of this elongation is due to the occasional presence of tertiary vortices. However, even when no tertiary vortices are present some elongation is noted. Measuring the eccentricity (height/width) of the contours in figure(s) 20, as a function of contour level, it is seen that the elongation in the Y - axis direction is approximately 20 - 40% (20% being a better estimate since tertiary vortices probably pushed this value towards 40%), see figure 25. Therefore, for analytical purposes it appears necessary to describe the vortex area as something other than circular. As a first step, a spatial variable is defined as

$$R \equiv (A/\pi)^{1/2} \quad ,$$

called the *equivalent radius.*

Using this, the exact functional dependence of circulation on the equivalent radius is

$$\frac{\Gamma}{\Gamma_o} = 1 - \exp -(\frac{R}{R^*})^2 \quad .$$

where Γ_o is the total circulation of the vortex, evaluated at an equivalent radius of infinity. However, the value of Γ_o can be directly evaluated as the y-intercept in the linear analysis in figure 22. With Γ_o known, R^* can be fitted. Doing so, the fitted values of Γ_o and R^* are shown in figure 24. Using this analysis, values of Γ_o can be determined without the necessity of evaluating an integral as the area approaches

infinity.[6]

Using this analysis procedure, all of the vorticity data collapses to the Gaussian (Error) function as seen in figure 23. The values of Γ_o, as stated earlier, are of importance in understanding the basic physics of this flow, and will be considered further at the end of this chapter.

The value R^* is a fundamental measure of the jet flow, being proportional to the vortex size (see figure 23). Figure 24 quantifies the size of these vortices, and provides an indication of the growth of the flow.

A lack of agreement in figure 23 is noted as R approaches the vortex edge. It has been stated previously that near the edge of the vortex freestream vorticity effects can be expected. It is interesting that, in figure 23, this effect appears to always constructively adds to the measured circulation. This is surprising in light of the fact that both signs of freestream vorticity are equally probable. This finding, seemingly inconsequential as it only involves regions at the edges of the vortex, can have one of three explanations: 1) that this additive effect is due to some physical effect of like vorticity attracting; 2) that it could be due to the interaction with the other vortex; or 3) the assumption of a linear relationship in figure 22 is inadequate[7].

---

[6] For verification of the fit, this expression can be rearranged to:

$$\frac{R}{R^*} = \sqrt{-\ln\left(1 - \frac{\Gamma}{\Gamma_o}\right)}$$

The data from the top of figure 22 is plotted according to this rearrangement, and the results are shown in figure 22 (bottom) where the rhs of this expression is the ordinate of this graph. The fit is excellent, except for those regions at large R, where freestream vorticity (presumably) affects the results.

[7] This discrepancy is traceable to the selection of Γ_o in figure 22. There is no physical reason why the distribution must be Gaussian, and as a result the forcing of the endpoint of the distribution to this profile could result in a value of circulation that is too low.

The analytic description of the circulation, and the good fit seen in figure 23, suggest that the vorticity distribution can be determined. From (3), the vorticity distribution can be calculated as

$$\omega = \frac{d\,\Gamma}{d\,A} \quad .$$

Substituting for Γ , the vorticity distribution becomes,

$$\omega = \frac{\Gamma_o}{\pi} \frac{\mathrm{d}}{\mathrm{d}R^2} \left(1 - \exp\left(- \frac{R^2}{R^{*2}} \right) \right)$$

Carrying out the differentiation gives,

$$\omega = \frac{\Gamma_o}{\pi} \frac{1}{R^{*2}} \exp - \left(\frac{R^2}{R^{*2}} \right) = \frac{\Gamma_o}{A^*} \exp - \left(\frac{A}{A^*} \right)$$

with $A^* = \pi R^{*2}$, showing that the vorticity is a Gaussian distribution in the equivalent radius.

The measured vorticity distributions along a line Z = constant and through the vortex center are shown in figure 26 for data from all cross sections. Good agreement between the vorticity distribution and the analytic expression is seen, but with a slight overshoot (5 - 10%) at the peak, with some scatter at the edges. The latter is considered the result of freestream vorticity.

Likewise, a similar fit can be made along a line Y = constant and through the vortex center. This distribution is shown in figure 27 , and shows a notable deviation from the analytic expression.[8]

---

[8] To clarify this deviation in figure 27, the Z - axis coordinate for the negative vortex is multiplied by (-1).

This noted deviation can be understood by considering two Gaussian vortices of equal but opposite strength with centers separated by a distance *S*. The resulting vorticity field is the superposition of these vortices, seen in figure 28, where a destructive interaction occurs in the region between the vortices.

The degree of agreement between the analytic expression and the measured profiles indicates that the non-circular geometry of the vortices is not crucial, although a more in-depth analysis of the vorticity distribution would consider this. Further, these results show the usefulness of the equivalent radius in describing these vortices.

4.2 Additional vortex measurements

To generate figures 26 and 27, a determination of the location of the vortex center, (Z_o, Y_o), was made. These coordinates can be used to determine the jet trajectory and vortex spacing.

The most common measure of this flow is the jet trajectory, the path followed by the jet in the X - Y plane. Typically measured by seeding the jet flow with a visible marker, such as smoke or dye, the trajectory can provide useful dynamical information, such as the transverse force and drag force of the jet (see Margason 1968).

For the present study the trajectory can be quantified by the points (X , Y_o). Noting that there are two values for each cross section (one for the negative and one for the positive vortex) the presently measured trajectories are shown in figure 29.

As indicated earlier, another measure of the jet growth is the separation of the vortex centers. Because of the difficulty of measuring vortex separation using flow

visualization, there are fewer reports of this measure. Vortex separation S is,

$$S(X) \equiv Z_o^-(X) - Z_o^+(X)$$

where the superscript $^-$ and $^+$ refer to the Z_o locations of the negative and positive vortex, respectively. Measured values of S are given in figure 30 .

Two local geometric measures have been made of the transverse jet: vortex size R^* and vortex spacing S. If the spatial distribution of flow properties are similar at all cross sections, the ratio of these two, essentially the aspect ratio, should be constant. As seen in figure 31, this ratio is not constant, given the few available data, for either streamwise position or velocity ratio. In figure 31 it appears that the jet broadens with increasing velocity ratio. Scaling **X** with the global length scale, D, serves only to increase the disparity seen in figure 31.

The impulse of a (two-dimensional) vortex pair is related to the product of the circulation and the separation of the vorticity centroids[9], Saffman (1992). The behavior of the product ($\Gamma_o S$) with streamwise location is shown in figure 32. Since the present results show a slight departure from symmetry, figure 32 shows this quantity for both the negative and positive vortex.

[9] For the present results the vorticity centroid and the location of peak vorticity determined in figures 26 and 27 closely coincide.

Chapter 5
Mean Velocity Measurements

Although considered predominantly a vortical phenomenon, the velocity characteristics of the transverse jet cross section are also of interest. The velocity fields for velocity ratio 10 are provided in this chapter, and the results discussed.

Past studies have reported mean velocity measurements, including those of Fearn & Weston (1974) and Andreopoulos *et al.* (1984) (1985) for measurements in the cross section (*i.e.,* the Y - Z plane), and by those of Andreopoulos *et al.* (1984) (1985), Crabb *et al.* (1981), Chassaing *et al.* (1974), and Keffer & Baines (1963) in the streamwise or axial direction.

The calculated velocity field is

$$\mathrm{v}\,(x, y, z; t) \quad \text{and} \quad \mathrm{w}\,(x, y, z; t) \quad ,$$

where v is the velocity component along the Y axis, and w is the velocity component along the Z axis. The mean velocities, v_o and w_o, can be calculated as

$$\mathrm{v}_o\,(x, y, z) \equiv \overline{\mathrm{v}\,(x, y, z; t)} = \frac{1}{N} \sum_{i=1}^{N} \mathrm{v}\,(x, y, z; i)$$

and

$$\mathrm{w}_o\,(x, y, z) \equiv \overline{\mathrm{w}\,(x, y, z; t)} = \frac{1}{N} \sum_{i=1}^{N} \mathrm{w}\,(x, y, z; i)$$

where the overbar denotes time-averaging, and has been replaced by discrete

averaging on the right hand side of these expressions. For the results in this chapter N = 750 (image pairs) .

The mean velocity fields, v_o and w_o, are shown in figure 33. These correspond to the vorticity fields of figure 20b, and to the conditions in table 4 for velocity ratio of 10 . Just as in the vorticity fields, the evolution of the jet flow can be observed in the velocity fields of figure 33. It is seen that with increasing downstream distance the jet flow penetrates further into the freestream. Likewise, the jet spreads in spatial extent as it evolves downstream.

The magnitude of the maximum velocity in the cross section is determined as

$$\mathbf{V}(x) \quad = \quad \mathbf{MAX} \; [\; ((v_o \; (x, y, z))^2 \; + \; (w_o \; (x, y, z))^2 \;)^{\; 1/2} \;] \quad .$$

This maximum speed is shown in the top of figure 34, showing the functional dependence of $\mathbf{V}(x)$ on streamwise location. As a result of the flow evolution, the velocity decreases with downstream location. Likewise it decays in a nonlinear manner, as expected from theoretical arguments, see Broadwell & Breidenthal (1984). The location of the point of maximum velocity in the cross section is shown in the bottom of figure 34. As expected, the maximum velocity is located at the midpoint between the two vortex centers where the induced velocity from each vortex reinforces each other.

A slight departure from symmetry is noted in the velocity fields of figure 33. This departure was also noted in the associated vorticity fields and is most likely due to the flow condition being only slightly above the critical value of Re, with a slight propensity to form tertiary vortices.

The perturbation velocity, the instantaneous departure from the mean flow, is calculated as:

$$v'(x,y,z;t) = v(x,y,z;t) - \overline{v(x,y,z;t)} = v(x,y,z;t) - v_o(x,y,z)$$

and,

$$w'(x,y,z;t) = w(x,y,z;t) - \overline{w(x,y,z;t)} = w(x,y,z;t) - w_o(x,y,z).$$

From these perturbation velocities estimates of turbulence quantities (mindful that the smallest turbulence scales are not resolved) can be computed using the long data records. The correlation,

$$\overline{v'w'} \equiv \overline{v'(x,y,z;t)\ w'(x,y,z;t)} = \frac{1}{N}\sum_{i=1}^{N} v'(x,y,z;i)\, w'(x,y,z;i)$$

indicative of the degree of turbulence production, is shown in figure 35. It is seen that these distributions are similar to the vorticity distributions in that there is symmetry about the Z/d = 0 midplane. However, there are indications that two correlation maxima exist for each vortex. This is best seen in the cross section at X/d = 86.4 . This particular cross section appears to be least affected by the occurrence of tertiary vortices. In this particular cross section there are two maxima for each vortex, with these peaks being positioned one on top of the other. This behavior is not understood in terms of the vortex pair model of the flow field.

The turbulent fluctuation terms

$$\overline{v'^2} \equiv \overline{v'(x,y,z;t)\ v'(x,y,z;t)} = \frac{1}{N}\sum_{i=1}^{N} v'(x,y,z;i)\, v'(x,y,z;i)$$

and

$$\overline{w'^2} \equiv \overline{w'(x,y,z;t)\ w'(x,y,z;t)} = \frac{1}{N}\sum_{i=1}^{N} w'(x,y,z;i)\, w'(x,y,z;i)$$

can also be computed. These quantities are shown in figures 36 a & b for velocity ratio 10 . Like the $\overline{v'w'}$ distribution, $\overline{v'^2}$ reflects the spatial distribution evident in the mean vorticity field (figure 20b), namely two mirror-image lobes indicative of the vortex pair. The turbulent fluctuation term $\overline{w'^2}$ lacks this spatial distribution. It is suggested that the difference between the quantities $\overline{v'^2}$ and $\overline{w'^2}$ is due to the effect of the vortex array residing at the jet midplane. Owing to the location and spatial arrangement of this vortex array it appears that it contributes to the level of $\overline{w'^2}$ and thereby blurs the distinction between the two streamwise vortices.

Figure 36c shows the peak value of the respective quantities, normalized by the local velocity scale, as a function of streamwise position. In figure 36c, it is noted that the turbulent quantities are approximately twice the magnitude of the $\overline{v'w'}$, indicating that the turbulent motion in the Y and Z directions are not fully correlated. It is also noted that the level of $\overline{w'^2}$ is about 50% larger than the level of $\overline{v'^2}$. As with the distribution in figure 36b, it is suggested that this increase in level is due to the contribution of the vortex array in the wake.

Measurement of turbulent quantities are lesser in extent than measurements for the mean velocities, and have been reported by Andreopoulos *et al.* (1984) (1985), Moussa *et al.* (1977), Crabb *et al.* (1981), and Keffer & Baines (1963) -- although these works are for measurements very near the jet origin and only on the center-plane of the jet.

As there are few published results available for comparison of the present measurements, the results of figures 33 - 36 are provided for future reference both for experimental and numerical studies.

Chapter 6
Concluding Discussion

This work has measured and presented the flow properties of the turbulent transverse jet. These measurements concentrate on the mean jet properties observable in the jet cross section for the reason that, as discussed in chapter 1, the transverse jet is analogous to a force applied transverse to a moving stream. In analogy to a lift force, the resulting flow field is a vortex pair whose axis of vorticity is approximately aligned with the freestream direction.

DPIV provides particle displacements over a two-dimensional image from which the vorticity field is calculated. DPIV has an advantage over single point measurement techniques such as laser doppler velocimetry or hot wire anemometry in providing a measure over a plane as opposed to a point in space. This advantage is even greater in a flow field such as the transverse jet, where the flow geometry does not allow simplification of measurement from a three-dimensional phenomenon to a two-dimensional phenomenon.

DPIV also provides quantitative visualization of the flow field. Seemingly an obvious result of imaging particles, it has provided in the present study the means to recognize and characterize alternate flow regimes that have not been previously reported. The recognition that the transverse jet does not always produce a symmetric vortex pair in the mean flow is a challenge for theoretical understanding of this flow, which to this point regards the vortex pair as the unique solution.

This study has defined to some extent the parameter space over which the mean flow is not a symmetric vortex pair. The existence domain of these alternate states, defined in Re and velocity ratio parameter space, indicates that an increasing value of Re is required with increasing velocity ratio in order to generate a symmetric vortex pair. This behavior indicates that an infinite velocity ratio requires a very large Re to create a typical transverse jet flow, suggesting an interesting boundary between the ordinary jet and the transverse jet: a slight disturbance in the surroundings of an ordinary jet does not immediately result in a transverse jet flow. This is of important practical value since for ordinary jet flow studies much attention is given to the experimental setup to insure that the surroundings are quiet and without any disturbance that might substantially alter the flow.

6.1 Discussion of vorticity

With understanding of the possibility of asymmetric flow, it was critical for the results presented in chapters 4 and 5 that the jet flows studied were at least in the Reynolds number range at which symmetry occurs. This presented a technical challenge. Limited by finite spatial imaging resolution and the challenges of cross correlating convecting flow fields, it was at the limit of current capabilities to insure, for all values of velocity ratio studied and presented in chapters 4 and 5, that a sufficiently high Re was provided. This requirement was easily achieved for the lowest velocity ratio (5) because of the relatively low value of Reynolds number required, and most difficult to achieve for the highest velocity ratio studied (20) due to the concomitantly higher Reynolds number required. It is evident that the Reynolds number for these results is just at or slightly above the critical value for steady symmetric flow. This

resulted from experimental limitations of implementing DPIV, especially finite spatial resolution as discussed above.

This difficulty is reflected in the results, and most easily observed in the mean vorticity fields of figure 20. The mean vorticity field shown for velocity ratio 5 shows the greatest degree of symmetry and regularity, while the mean vorticity field for 20 is showing some evidence of asymmetry, although to a small degree compared to those flows described in chapter 3. This asymmetry is appreciated by viewing figure 20c. The negative vortex, that residing in + Z/d domain, shows a slight elongation most notable at lower vorticity (contour) levels. This results from a slight propensity of the flow, at this Re, to show intermittent tertiary-vortex behavior, *i.e.,* at this Re the negative vortex showed an intermittent tendency to split into two vorticities, which was readily noted in reviewing the complete data record. The resulting mean vorticity in figure 20c is the average of a mostly symmetric vortex pair averaged with an occasional splitting of the negative vortex. Such intermittence was not noted for the velocity ratio 5 case, and the data for velocity ratio 10 shows a behavior somewhat between that for velocity ratio 5 and 20.

A similar asymmetry is noted in the peak vorticity values shown in figure 21. For velocity ratio 5, the peak values for the positive and negative vorticity are close in magnitude, while a large difference is seen for velocity ratio 20.

The measurements of circulation herein are the first using DPIV. Measurements using hot-wire anemometry along the jet center-plane at Z = 0 were made by Fearn & Weston (1974). From these measurements the authors inferred vortex circulation based upon certain assumptions of vorticity distribution and vortex separation. The present results do not rely upon any such assumptions.

The ability to map the vorticity distribution to a Gaussian distribution, shown in chapter 4, aids in both the experimental interpretation of the data and in theoretical understanding. As shown in figure 23, the distribution of circulation within each mean vortex fits a Gaussian distribution in square-root of the vortex area. This makes possible the correct determination of total circulation as well as vortex size. The success of this mapping aids the understanding of the interaction of the two vortices as seen in figure 28.

In chapter 4 the data is presented with spatial variables normalized by **d**, the jet diameter. Scaling spatial variables with the global length scale, **D**, the principal vorticity measures of the flow field, namely circulation, vortex size, and the product (Γ_o S^*) are shown in figures 37, 38, and 39a. The jet trajectory from figure 29, and vortex spacing from figure 30 are also scaled with D and shown in figure 40. The trajectory in figure 40 is the most frequently reported property of the transverse jet, and for reference the trajectory measure made by Pratte & Baines (1967) is shown in figure 40 as a lightly shaded curve. The discrepancy between the present results and that of Pratte & Baines is most likely due to the difference between measuring jet trajectory from flow visualization and from the present quantitative results.

It is noted that in figure 38 that the measurements of vortex size R^* do not lie on a single curve, while measurements of vortex separation in figure 40 do fall onto a single curve when normalized by the global length scale D. This discrepancy seems related to the fact that cross sectional dimensions depend upon the velocity ratio as shown in figure 31. Figure 40 suggests that the vortex separation is the more appropriate measure of local jet size.

Figures 39a and 39b show the impulse normalized by the Jet Momentum Flux,

using a unit length and $\frac{1(unit\ length)}{u_\infty}$ as length and time scales respectively.[10] Figure 39a provides the impulse assuming the vortices to be symmetric, while figure 39b utilizes a direct determination of impulse[11]. Both figures show a value at or near unity for all streamwise locations, indicating conservation of impulse. The discrepancies from unity are attributed to several factors. Clearly for the mean vorticity fields of figures 20a-c that are not symmetric the measurement of impulse in figure 39a is invalid. Further, the results of figure 39a depend upon the value Γ_o (which may be too low, see previous discussion). Likewise, for those measurement domains in figures 20a-c that do not encompass the entire vortex results in an incomplete integral evaluation in figure 39b.

Acknowledging some presence of flow field asymmetry, the results for normalized circulation[12] in figure 41 are given as the average of the measured values for the positive and negative vortex. Since the mean flow does not show the presence of tertiary vortices, this average is intended to be the truest measure of circulation.

6.2 Discussion of velocity

The velocity fields described in chapter 5 show many of the hallmarks of the vortex pair behavior evident in the results of chapter 4. Provided the mean flow field is a symmetric vortex pair, the peak mean velocity measured in the cross section is

[10] This grouping of parameters does not rely explicitly upon a length scale.

[11] Use is made of equation 3.10.15 from Saffman (1992). If the vortex pair is assumed symmetric, the impulse is determined from the product of circulation and (centroid) separation. In figure 39b, a direct computation of Saffman's equation 3.10.15 is made over the entire measurement domain.

[12] The normalized circulation $\frac{\rho_\infty \overline{\Gamma_o}}{\rho_{jet}\ u_{jet}^{\ 2}\ A_{jet}\ \frac{1}{u_\infty D}}$ reduces to $\frac{\rho_\infty^{\ 1/2}\ \overline{\Gamma_o}}{\rho_{jet}^{\ 1/2}\ u_{jet}\ A_{jet}^{\ 1/2}}$.

found on or near the jet center-plane at Z = 0 where the strongest induced velocity results. This suggests that many of the vortex pair properties measured by DPIV can be determined by pointwise measurement of the center-plane velocity.

It is now understood that the jet flow is not composed only of the region called the jet body. In addition to the jet body, a vortex array resides in and is centered about the plane Z = 0. These vortices are aligned approximately along the Y - axis, and flow visualization shows that these vortices span from the wall or surface at Y = 0 to, through, and beyond the outer boundary of the jet body.

The similar appearance between the vortex array and the vortex wake behind a two-dimensional cylinder has prompted the name vortex wake. However, significant differences exist between a cylinder wake and the vortex array. The most striking difference is the longevity of the vortices. Flow visualization shows that the vortex array persists longer in the streamwise direction (when measured in distance normalized with the diameter) than a cylinder wake. First suggested by Kuzo & Roshko (1984), this longevity may be due to vortex stretching by the induced velocity of the jet body, which results in an increased velocity associated with the vortex filament (see Saffman 1992), enabling the observed longevity.

6.3 Concluding remarks

This study has provided insights into the transverse jet which are important both for theoretical understanding and practical application.

Contributing to the fundamental understanding of this flow, this study has verified that, provided the Reynolds number is sufficiently high, the transverse jet

mean flow consists of a pair of symmetric diffuse vortices. These vortices have been shown to have a Gaussian spatial distribution. The impulse of these vortices has been measured for three velocity ratios.

The demonstrated existence of alternate mean flow states bridges the gap between theoretical understanding and practical application. The very existence of these alternate mean flows challenges the theoretical understanding of this flow -- as at present analytical descriptions involve only a symmetric vortex pair. Additionally, the existence of these alternate states introduces another design parameter for practical applications.

The existence and mapping in parameter space of the alternate mean flow states for the transverse jet provides guidance for effective practical use of transverse jets. As described in chapter 1, transverse jets are used for a multitude of applications involving mixing, dispersion, and pressure control over adjacent surfaces. This work has demonstrated that the jet can exist in several alternate flow states, depending upon the value of Re. Therefore, in addition to the design parameters of Re, velocity ratio, diameter, and trajectory, there is the additional parameter of mean flow state.

This is of importance for many applications. Although no measurement was made of the different mixing characteristics of a symmetric vortex pair versus the unsteady-asymmetric or steady-asymmetric flow state, the existence of tertiary vortices suggests differences in mixing characteristics. If such differences are substantiated, it should be possible to selectively use transverse jets for mixing.

Consider the example of film cooling, where transverse jets (typically an array of jets in tandem) are used to cool a downstream surface. A typical application is in combustion processes. This cooling of the downstream surface is a scouring of the

boundary layer by the induced flow of the transverse jet that augments the convective heat transfer from the wall to the outer stream. The reader is referred to the extended discussion in Goldstein (1971) for a review of this technology. The flow fields in figure 15 indicate that at or near the critical value of Re a tertiary vortex appears in the flow near the surface. It is anticipated that the closer proximity of the tertiary vortices to the wall (as evident from the lower trajectory of these vortices) will have a stronger "film cooling" effect than the highly symmetric vortex pair flow state. As typical applications involve high speed flows but minute jet orifices, it is feasible that a design can be tuned to operate in a steady state by selecting a value of Re such that a steady-asymmetric flow state with tertiary vortices exists.

Another example is the application of transverse jets for aerodynamic control over surfaces. These jet flows are used for flow attachment and control over surfaces when operating at high angles of attack. Flow unsteadiness is often reported in this application. Considering the operating range -- typically at high Reynolds number, but also at high values of velocity ratio (unlike film cooling) -- the value of the critical Re for transverse jets can range possibly to tens of thousands. If a transverse jet is inadvertently used in the unsteady - asymmetric flow state, which has been shown in chapter 3 to be highly unsteady with dynamic shifting of the flow pattern from side to side, then the resulting pressure on the control surface will also be unsteady. In addition, unsteadiness is always to be expected resulting from the fluctuations inherent in the vortex array.

A final example, of more immediate application to GALCIT related research is the findings of Fric & Roshko (1994). In studying the wake vortices, it was found that certain flow conditions were difficult to visualize (Roshko 1995). With the jet

operating in an unsteady-asymmetric flow state the location of the vortex array is also unsteady, making Eulerian (smoke) seeding of the vortex array difficult. This observation may also account for the variations in shedding frequency measured by Moussa *et al.* (1977), what the authors call the "two regimes" because of the difficulty in making measurements using a stationary probe in an unsteady flow. Further investigation is required to substantiate this, however, knowledge of the alternate mean flow states has a most practical application in this case.

Velocity Ratio	**Re**	**d** *inch*	$\mathbf{u_{jet}}$ $\frac{cm}{\text{sec}}$	$\mathbf{u_\infty}$ $\frac{cm}{\text{sec}}$	*Figures*
5	6138	0.30	80.6	16.0	6, 7, 20a, 21, 23, 24, 25, 26, 27, 29, 30, 31, 32, 37, 38, 39, 40, 41
10	2079	0.093	88.0	8.9	8a, 11, 12a-c, 15, 16, 17,
10	4371	0.093	185.	18.1	8a, 13, 14a-c, 15, 16, 17,
10	7250	0.093	307.	30.9	8b, 9, 10a-c, 15, 16, 17,

TABLE 6. Cross reference of experimental settings ($\nu_{jet} = \nu_\infty = 0.01 \frac{cm^2}{\text{sec}}$).

Velocity Ratio	**Re**	**d** *inch*	$\mathbf{u_{jet}}$ $\frac{cm}{sec}$	$\mathbf{u_\infty}$ $\frac{cm}{sec}$	*Figures*
10	9993	0.191	206.	20.8	6, 7, 8b, 17, 20b, 21, 23, 24, 25, 26, 27, 29, 30, 31, 32, 33, 34, 35, 36a, 36b, 36c, 37, 38, 39, 40, 41
20	13,087	0.093	554.	27.7	6, 7, 20c, 21, 23, 24, 25, 26, 27, 29, 30, 31, 32, 37, 38, 39, 40, 41

TABLE 6 *(continued).* **Cross reference of experimental settings.**

References

Abrahmovich, G.N. (1963) **The Theory of Turbulent Jets**. M.I.T. Press, Cambridge MA.

AGARD (Cantwell, B. et.al. editors) (1993) Computational and Experimental Assessment of Jets in Cross Flow. *AGARD Conference Proceedings 534* , Neuilly Sur Seine, France.

Andreopoulos, J. (1985) On the structure of jets in a crossflow. *J. Fluid Mechanics* **157**, 163-197.

Broadwell J.E. & Breidenthal R.E. (1984) Structure and Mixing of a Transverse Jet in Incompressible Flow. *J. Fluid Mechanics* **148**, 405-412.

Callagan, E.E. & Ruggeri, E.S. (1948) Investigation of the penetration of an air jet directed perpendicularly to an air stream. *N.A.C.A. TN 1615.*

Chassaing P., George J., Claria A. & Sananes F. (1974) Physical characteristics of subsonic jets in a cross-stream. *J. Fluid Mechanics* **62** *(1)*, 41-64.

Crabb, D., Durao, D.F.G. & Whitelaw, J.H. (1981) A Round Jet Normal to a Crossflow. *Trans ASME* **103** March.

Durando, N.A. (1971) Vortices induced in a jet by a subsonic crossflow. *AIAA Journal*, **9** 325-327.

Fearn, R. & Weston, R.P. (1974) Vorticity associated with a jet in a cross flow. *AIAA Journal* **12**, 1666-1671.

Foss, J.F. (1980) Interaction Region Phenomena for the Jet in a Cross-Flow Problem. *SFB 80/E/161* Universtat Karlsruhe.

Fric T.F. & Roshko A. (1994) Vortical structures in the wake of a transverse jet. *J. Fluid Mechanics* **279** 1-47.

Gharib, M (1983), The Effect of Flow Oscillations on Cavity Drag and a Technique for its Control. *Ph.D. thesis*, California Institute of Technology, Pasadena, CA.

Goldstein, R.J. (1971) Film Cooling. *Advances in Heat Transfer,* **7** 321-379.

Hinze, J.O. (1975) **Turbulence**. McGraw-Hill (second edition).

Jordinson, R. (1956) Flow in a Jet Directed Normal to the Wind. *ARC Report R&M 3074.*

Kamotani, Y. & Greber, I. (1974), Experiments on a turbulent jet is a cross flow. *AIAA Journal* **10**, 1425-1429.

Keffer J.F. & Baines W.D. (1963) The round turbulent jet in a cross-wind. *J. Fluid Mechanics* **15** 481-496.

Kuzo, D.M. & Roshko, A. (1984) Observations on the wake region of the transverse jet. *Bulletin of the American Physical Society* **29**, 1536.

Lamb, H. (1945) **Hydrodynamics**. Dover Publications.

Le Grives, E. (1977) Mixing process induced by the vorticity associated with the penetration of a jet into a cross flow. *T.P. No. 1977 - 2 (CIMAC).*

Liepmann, H.W. & Roshko, A. (1957) **Elements of Gasdynamics**. John Wiley & Sons.

Margason, R.J. (1968) The Path of a Jet Directed at Large Angles to a Subsonic Free Stream. *NASA TN D-4919.*

McMahon H.M., Hester D.D. & Palfrey J.G. (1971) Vortex shedding from a turbulent jet in a cross-wind. *J. Fluid Mechanics* **48** *(1)* 73-80.

Moussa Z.M., Trischka J.W. & Eskinazi S. (1977) Mixing of a round jet with a cross-flow. *J. Fluid Mechanics* **80** *1*, 49-80.

Pratte, B.D. & Baines, W.D. (1967) Profiles of a round turbulent jet in a cross flow. **92** *HY6* 5556-5564 November (see also *corrections in* **93** *HY3* 815-824 May).

Roshko, A (1995) *Private communication in laboratory.*

Ruggeri, R.S., Callagan, E.E. & Bonden, C.T. (1950) Penetration of Air Jets Issuing from Circular, Square and Elliptical Orifices Directed Perpendicularly to an Air Stream. *NACA TN 2019.*

Saffman, P.G. (1992), **Vortex Dynamics**. Cambridge University Press.

Snel, H. (1974) A model for the calculation of the properties of a jet in a cross flow. *National Aerospace Laboratory NRL (The Netherlands)* **NRL TR 74080U**.

Townsend, A.A. (1956), **The Structure of Turbulent Shear Flow**. Cambridge University Press.

Willert, C.E. & Gharib, M. (1991), Digital Particle Image Velocimetry. *Experiments in Fluids* **10**, 181-193.

Willert, C.E. (1992), The Interaction of Modulated Vortex Pairs with a Free Surface. Ph.D. Thesis, Dept. of Appl. Mech. Eng. Sci., Univ. of California, San Diego.

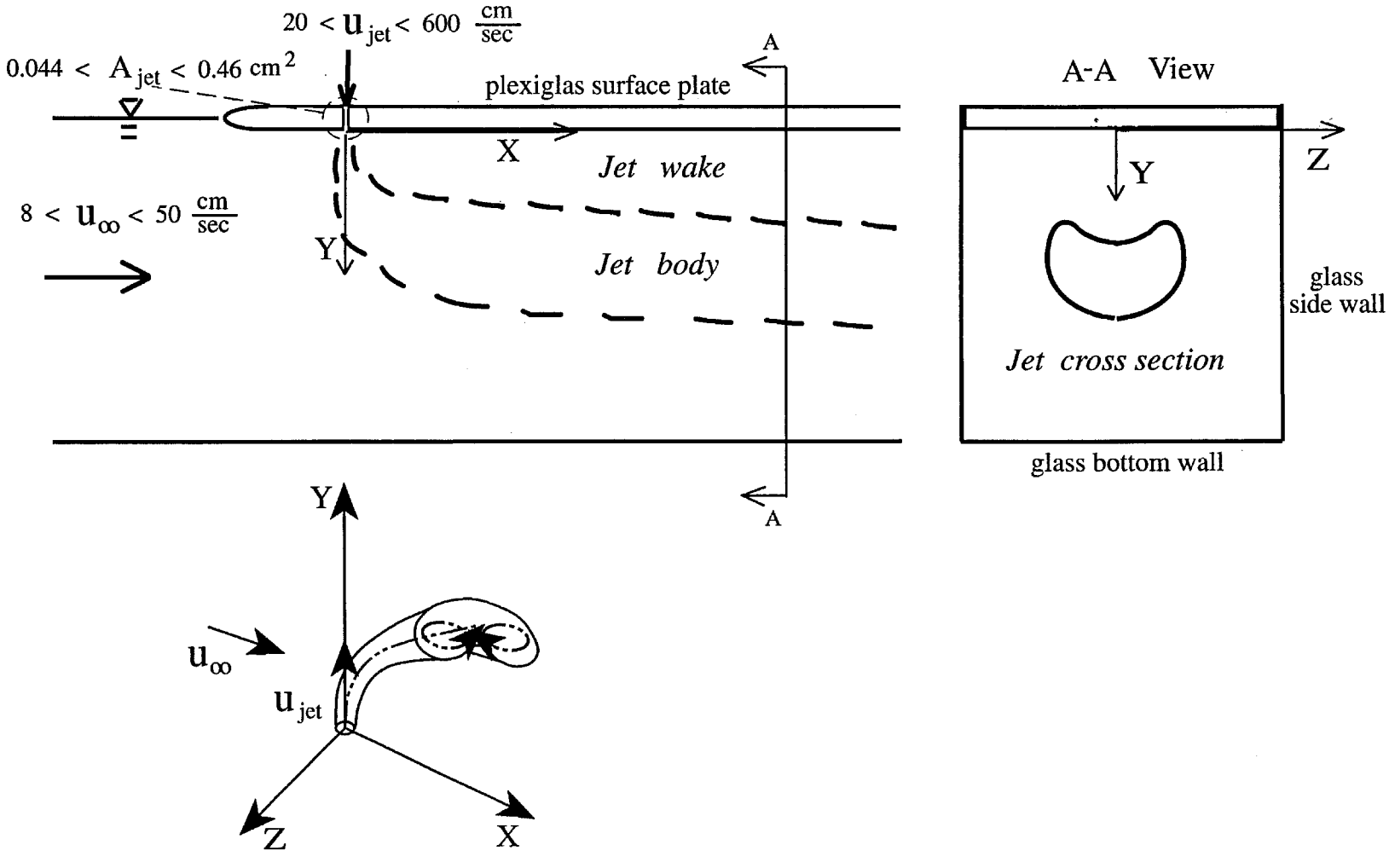

Figure 1. Side and cross section views of a turbulent transverse jet with defined coordinate system. A perspective view of the transverse jet is shown at bottom.

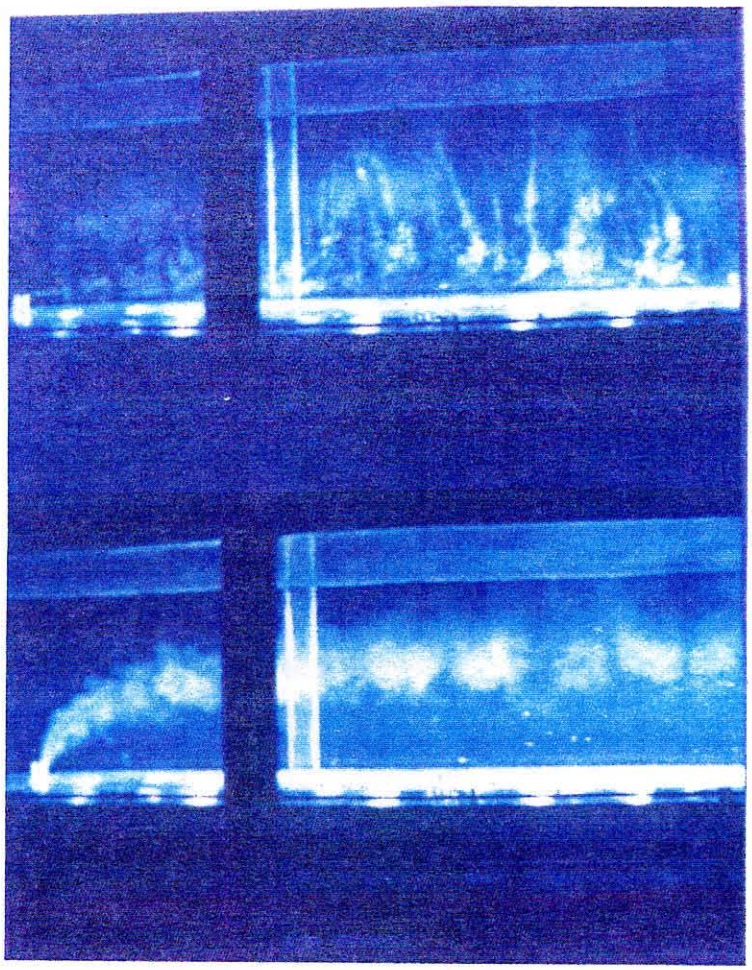

Figure 2. Visualization of the vortex array. Bottom image shows jet body flow visualization: top image shows vortex array visualization. Flow is from left to right.

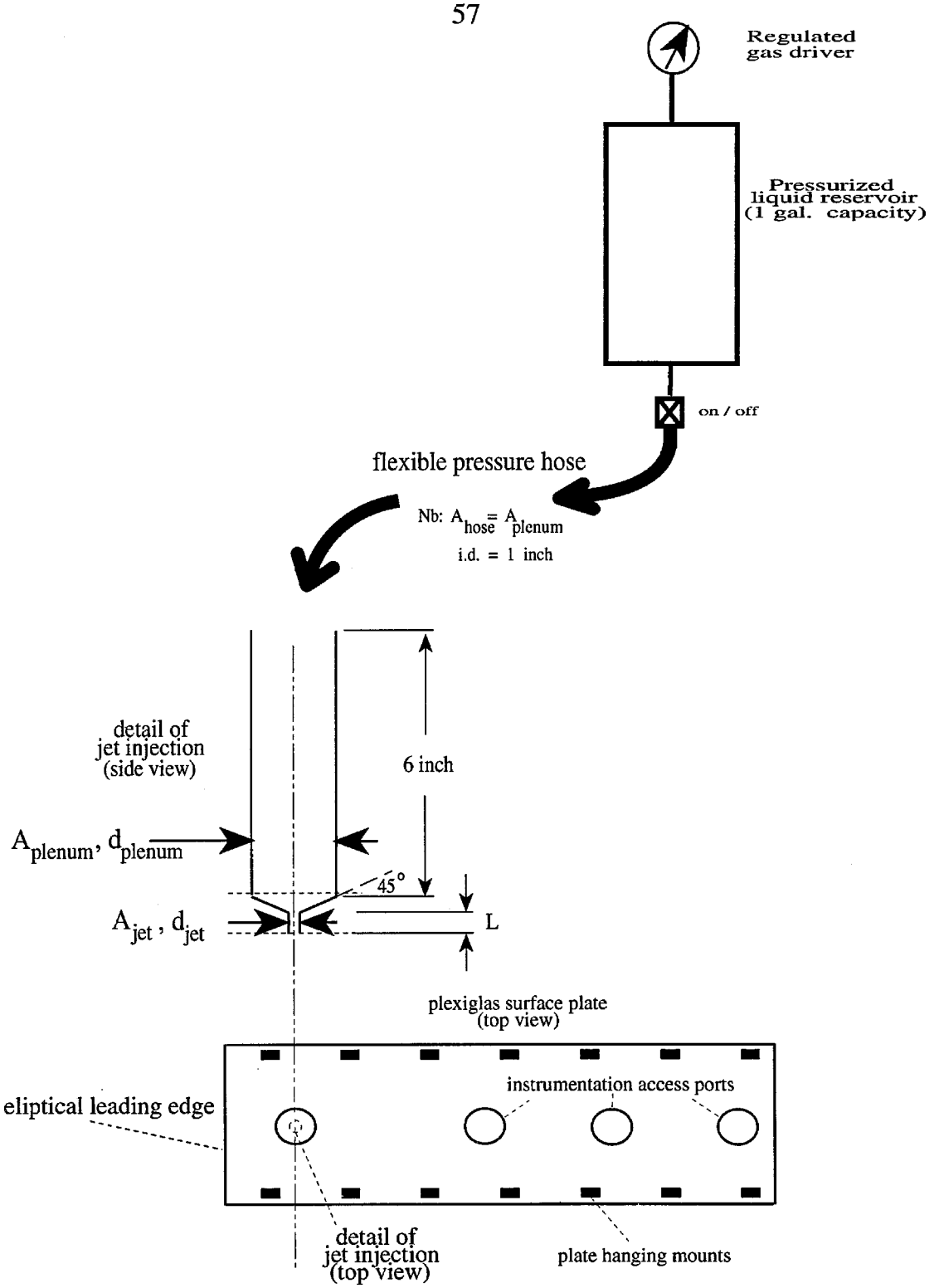

Figure 3. Jet supply and injection. A liquid reservoir and gas driver provide flow to the jet plenum and nozzle via a flexible pressure hose. The jet nozzle is flush mounted to the first port of the plexiglas surface plate.

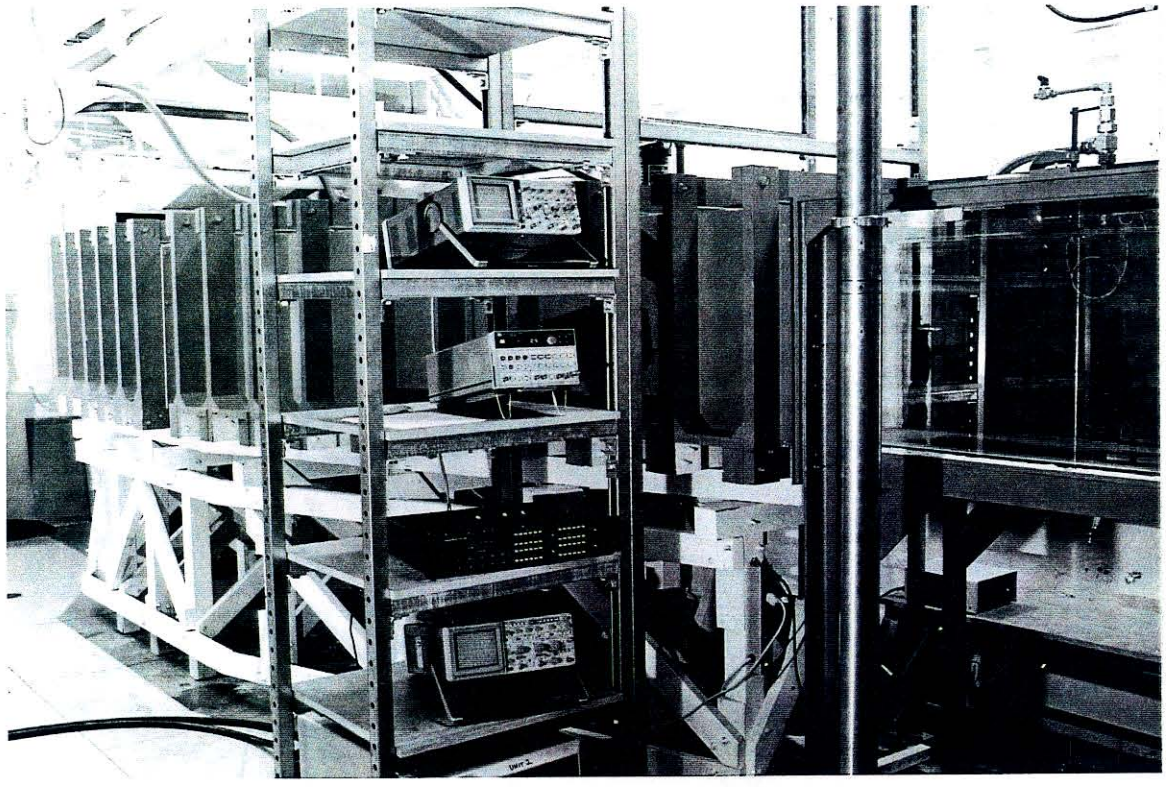

Figure 4. Photograph of laboratory.

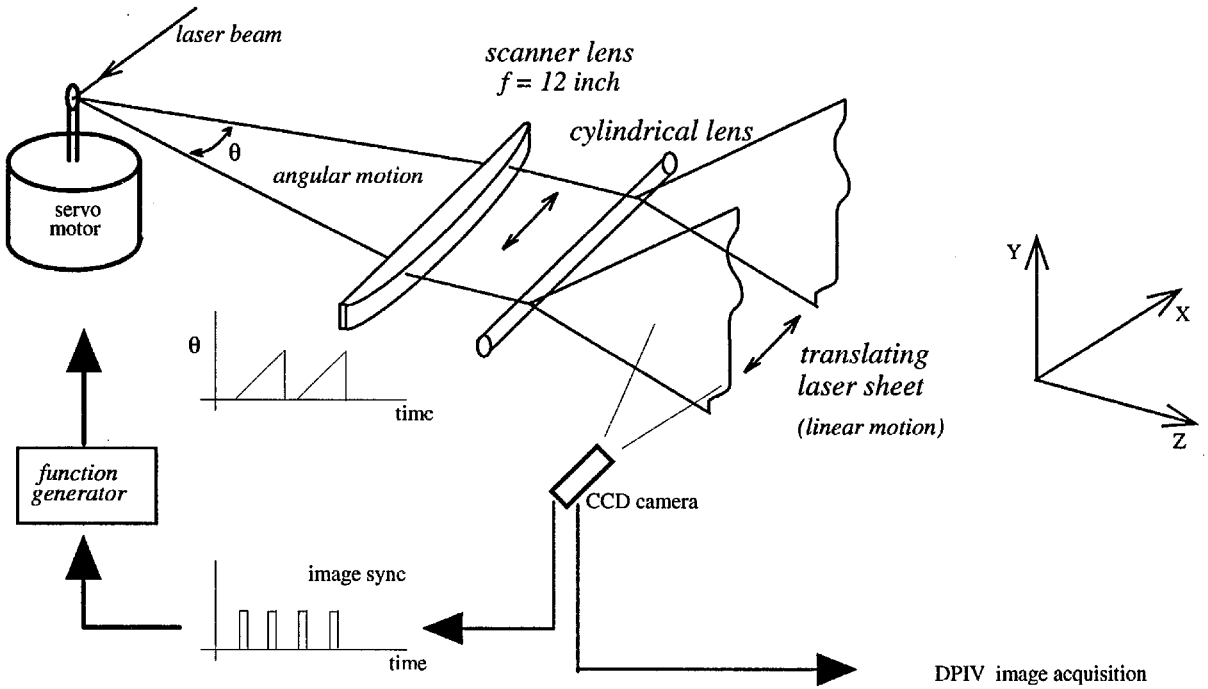

Figure 5. Optical scanning setup for convecting flow.

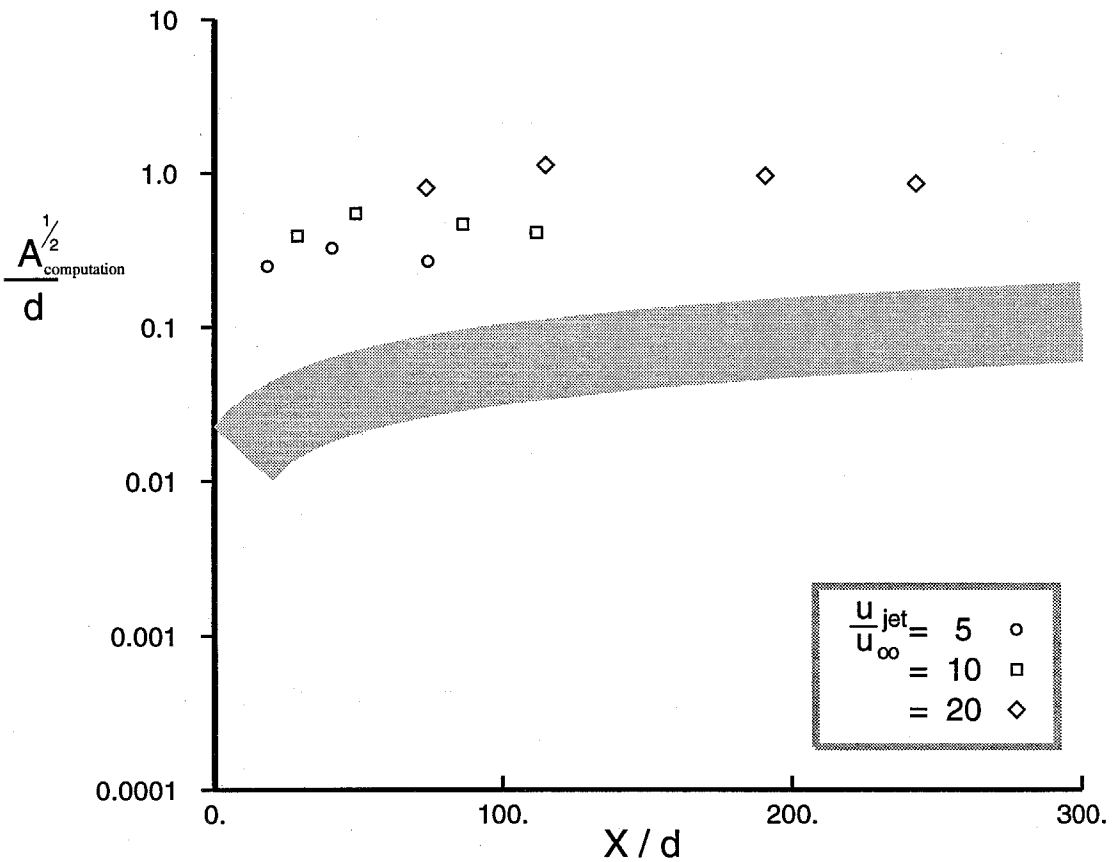

Figure 6. Spatial resolution of DPIV. The estimated Kolmogorov range is shown in shaded region.

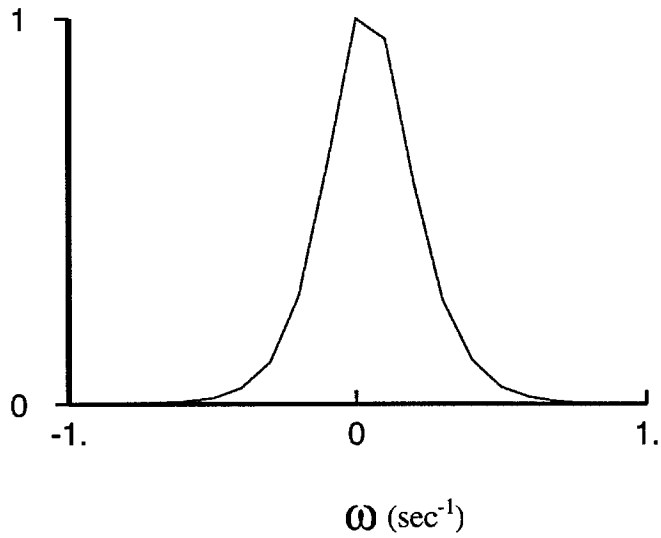

Figure 7. Histogram distribution of measured freestream vorticity: 95% of the freestream vorticity is less than 0.6 (sec-1) in magnitude.

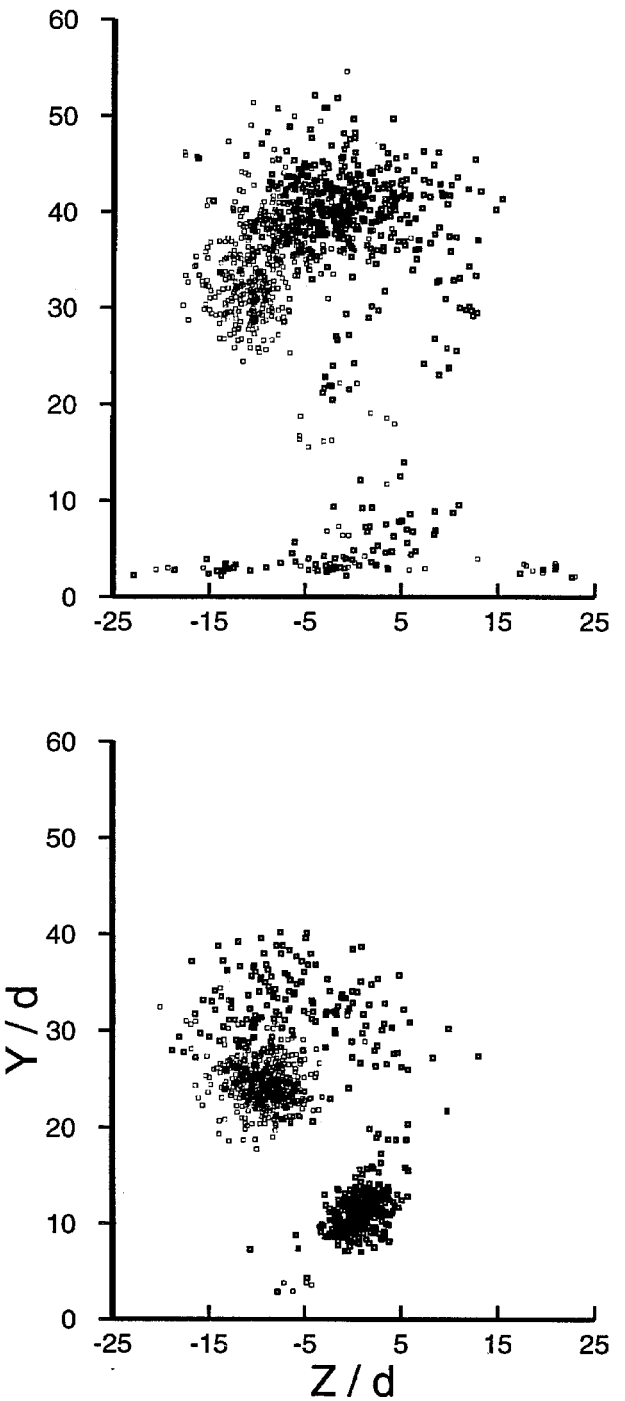

Figure 8a. Loci plot of peak vorticity: Re = 2079 at X/d = 124 (top), and Re = 4371 at X/d = 115 (bottom).

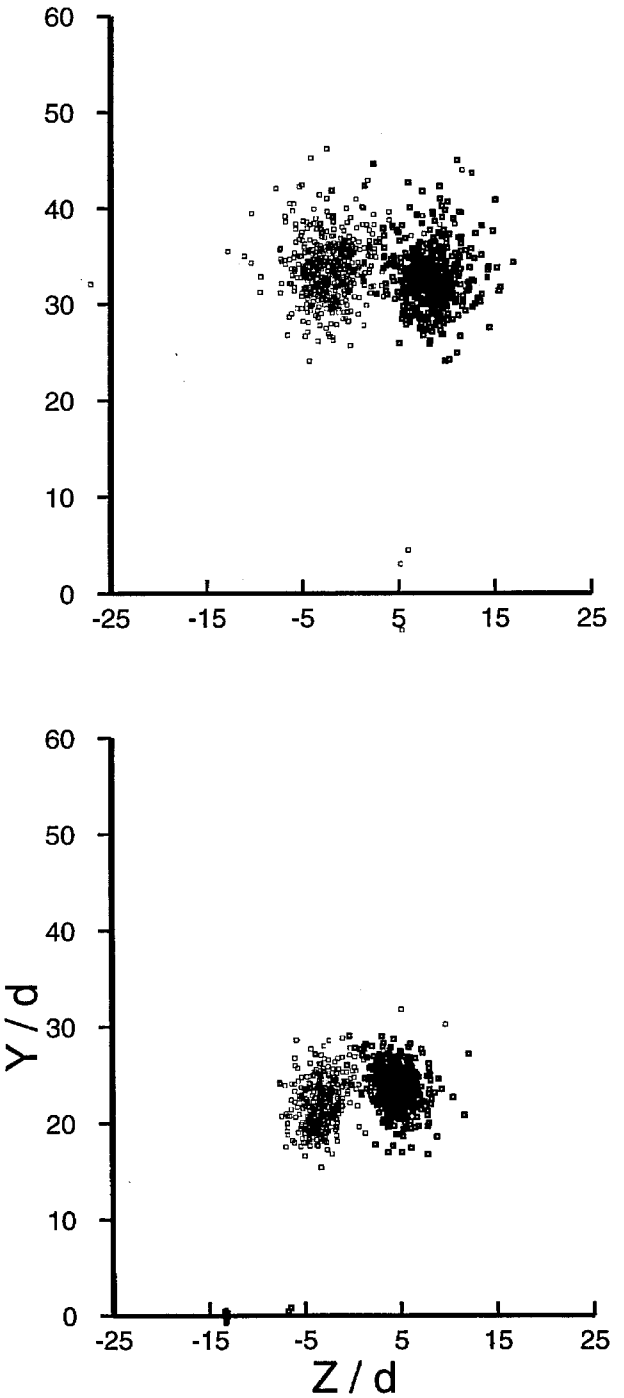

Figure 8b. Loci plot of peak vorticity: Re = 7250 at X/d = 113 (top), and Re = 9993 at X/d = 49 (bottom).

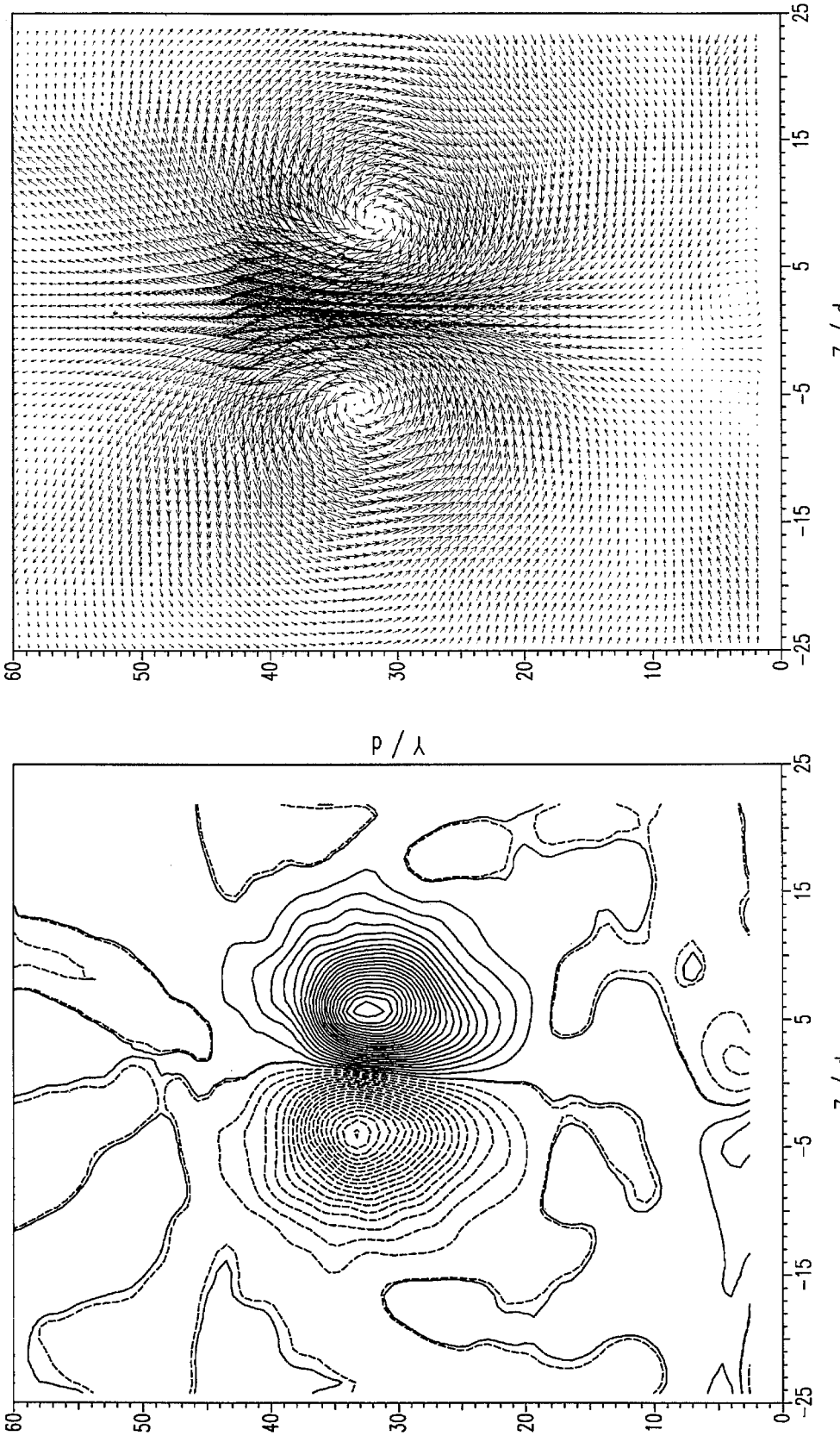

Figure 9. Mean vorticity and velocity fields, velocity ratio 10, Re = 7250 at X/d = 113 .

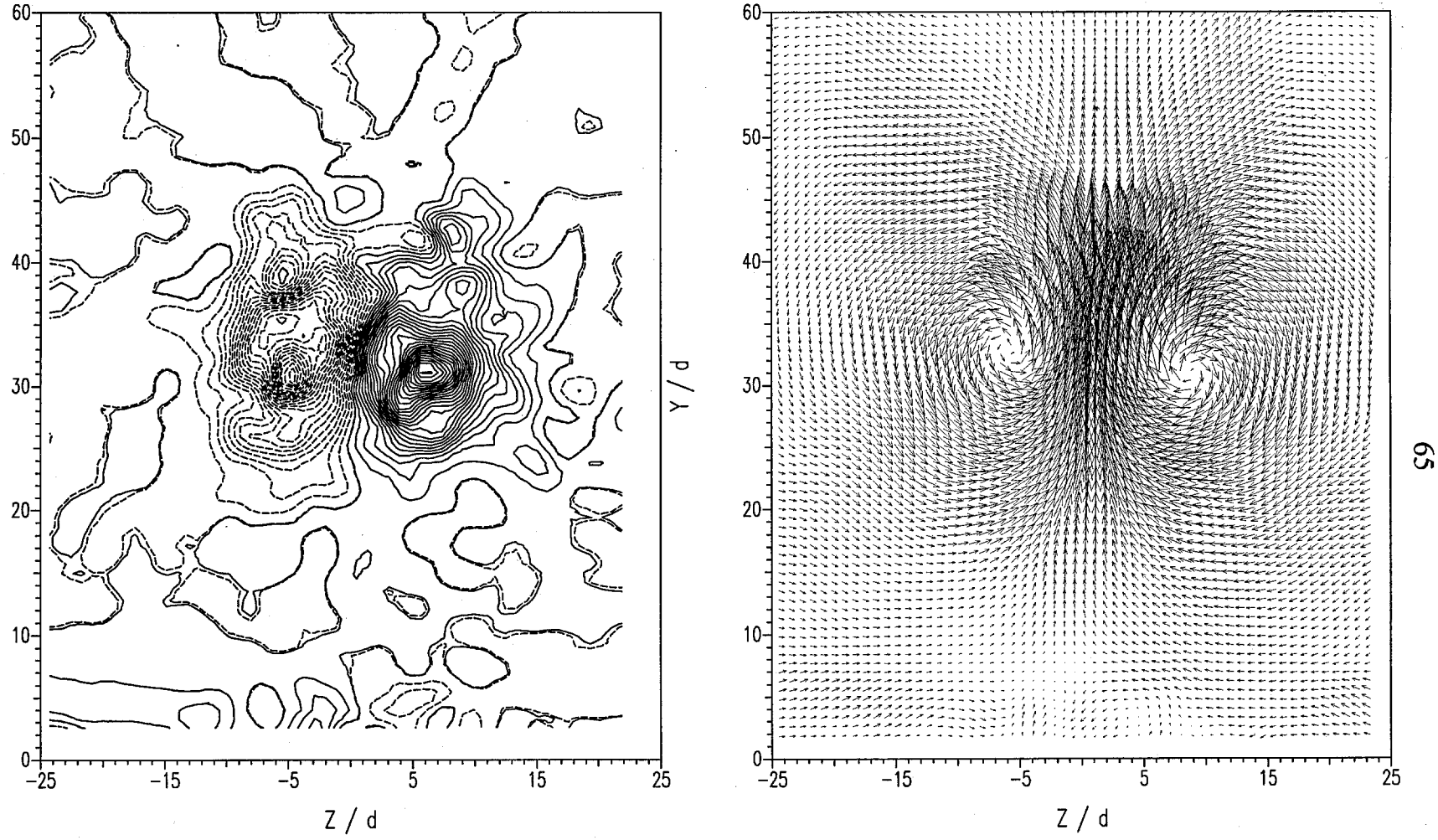

Figure 10a. First sequential (1 sec) average of vorticity and velocity fields, velocity ratio 10, Re = 7250 at X/d = 113 .

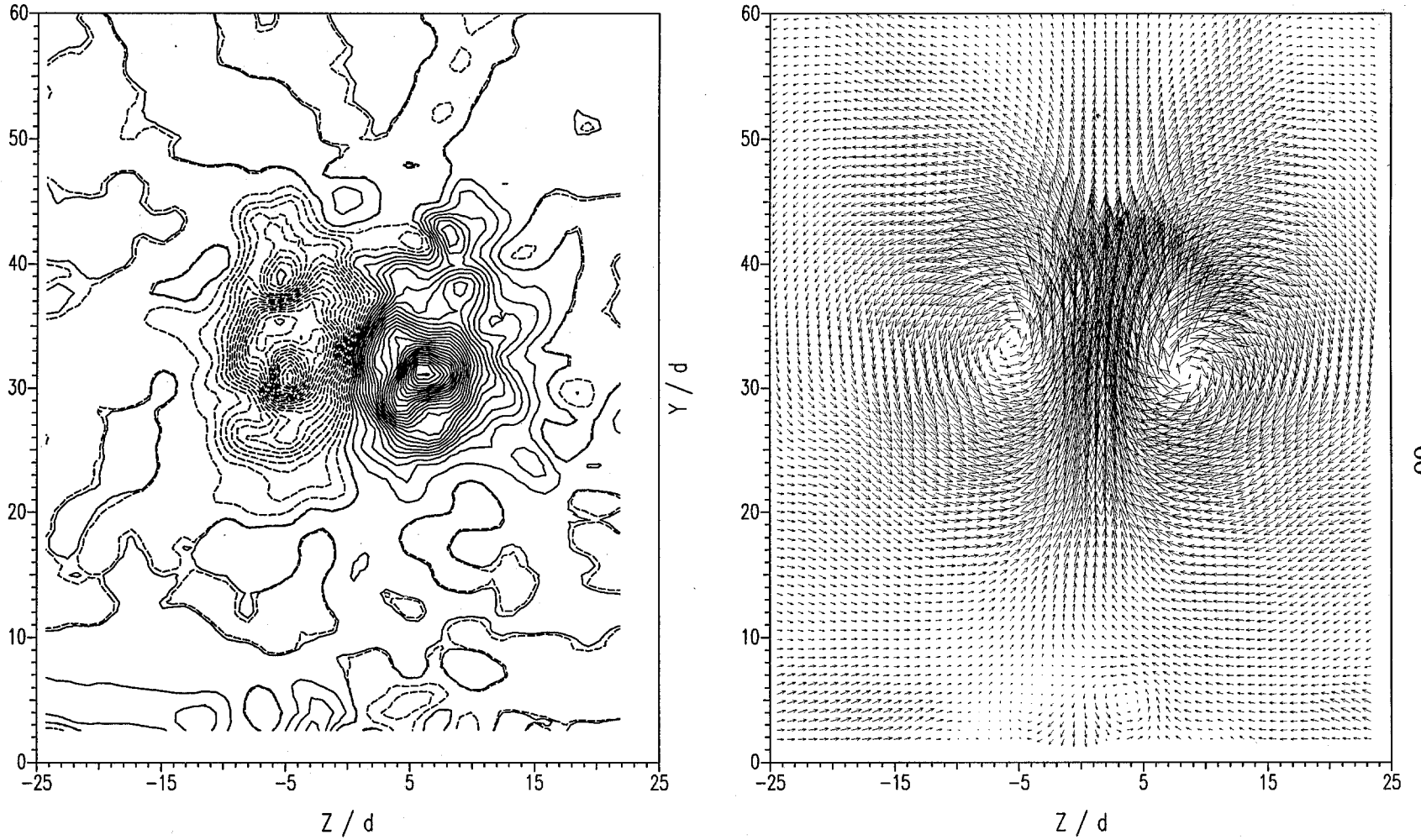

Figure 10b. Second sequential (1 sec) average of vorticity and velocity fields, velocity ratio 10, Re = 7250 at X/d = 113.

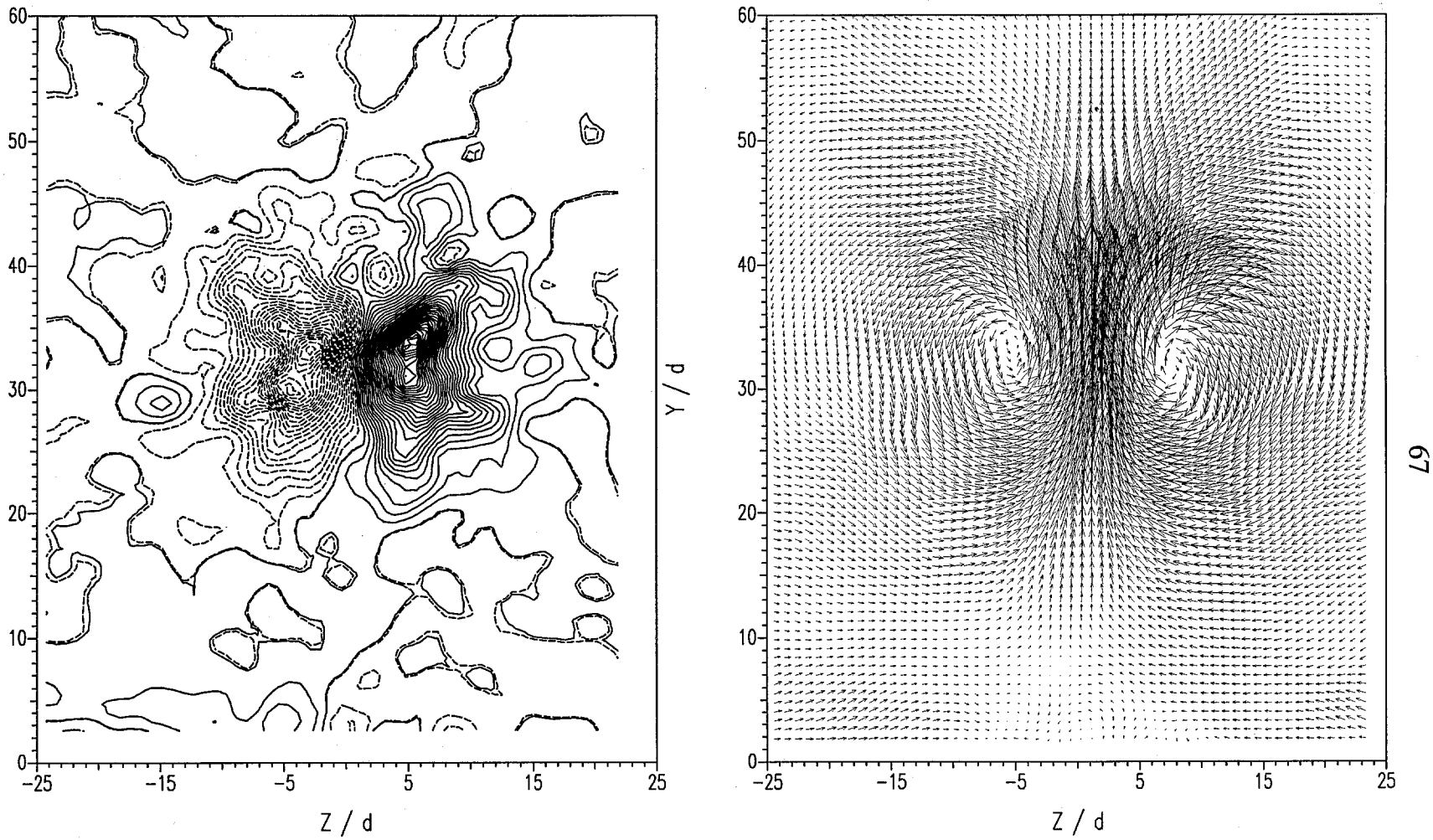

Figure 10c. Third sequential (1 sec) average of vorticity and velocity fields, velocity ratio 10, Re = 7250 at X/d = 113.

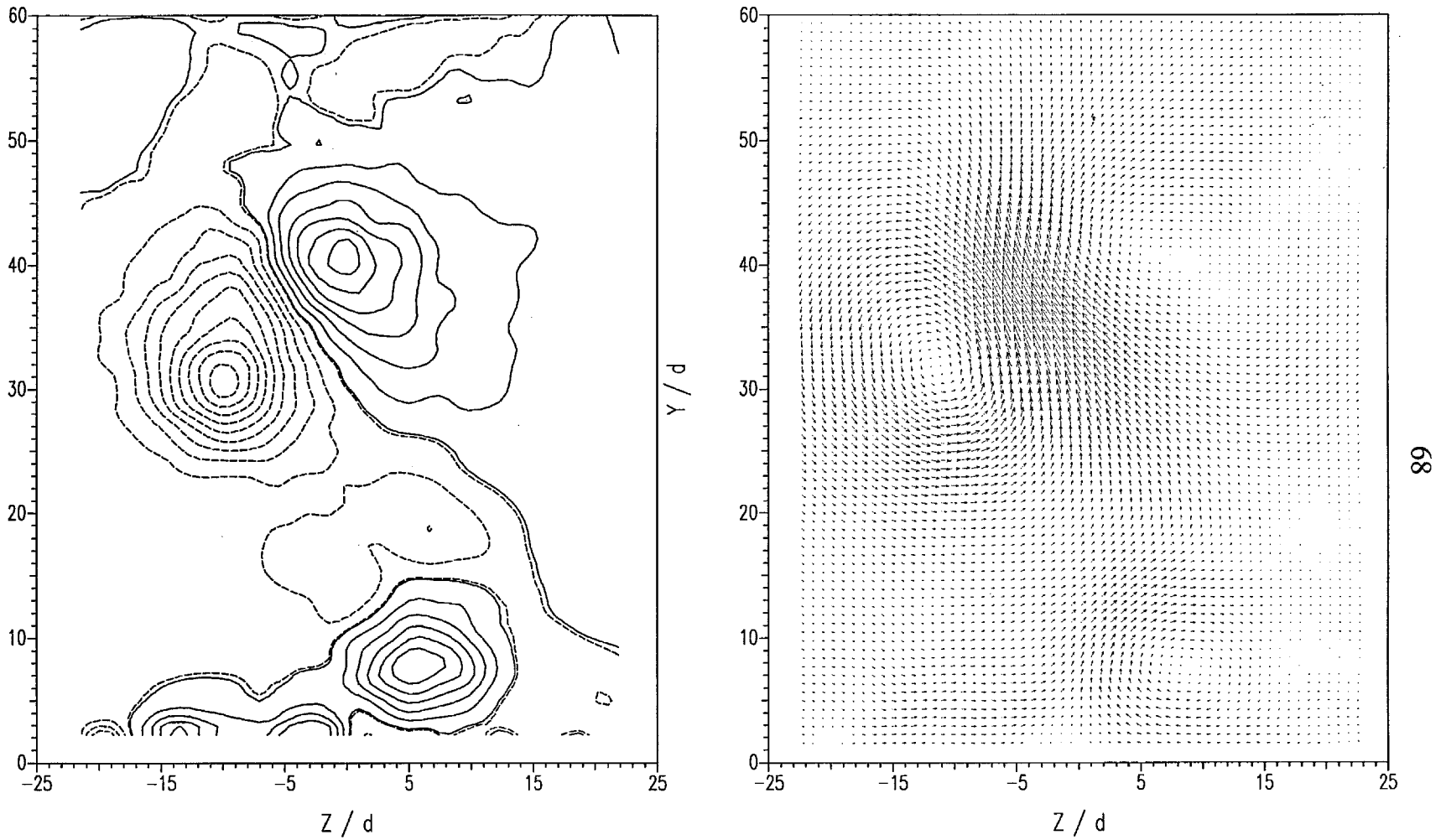

Figure 11. Mean vorticity and velocity fields, velocity ratio 10, Re = 2079 at X/d = 124 .

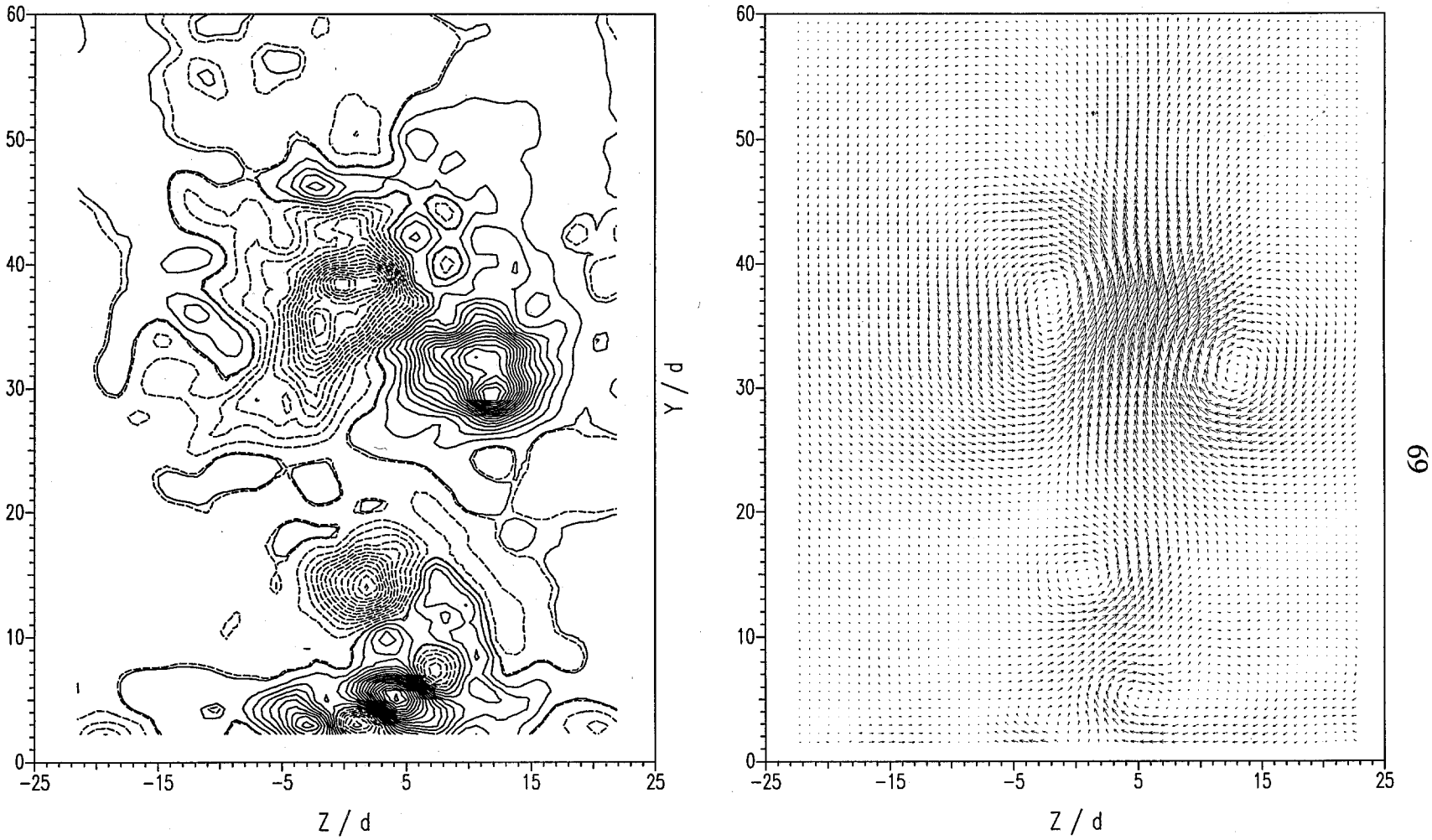

Figure 12a. First sequential (1 sec) average of vorticity and velocity fields, velocity ratio 10, Re = 2079 at X/d = 124.

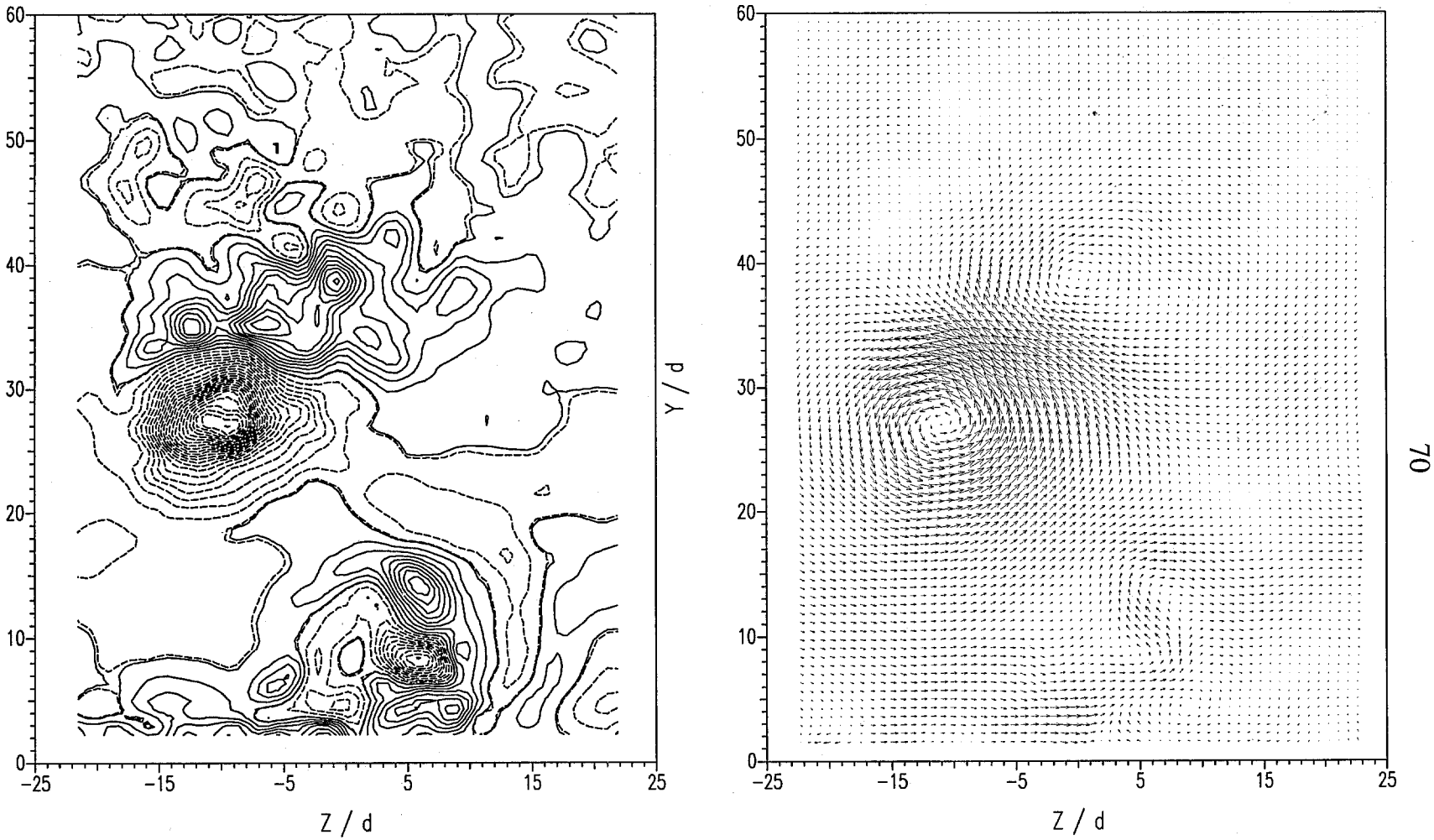

Figure 12b. Second sequential (1 sec) average of vorticity and velocity fields, velocity ratio 10, Re = 2079 at X/d = 124.

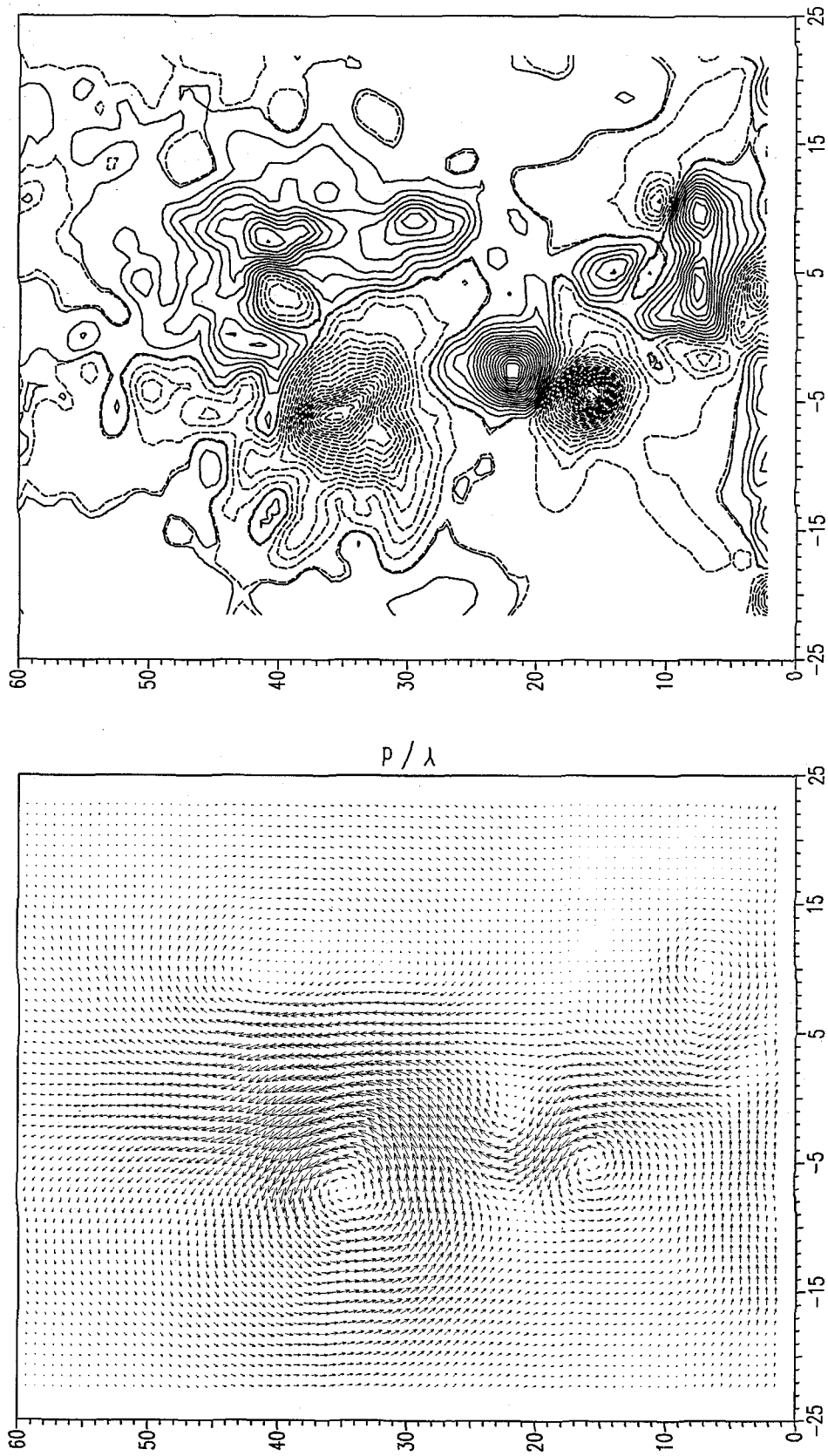

Figure 12c. Third sequential (1 sec) average of vorticity and velocity fields, velocity ratio 10, Re = 2079 at X/d = 124 .

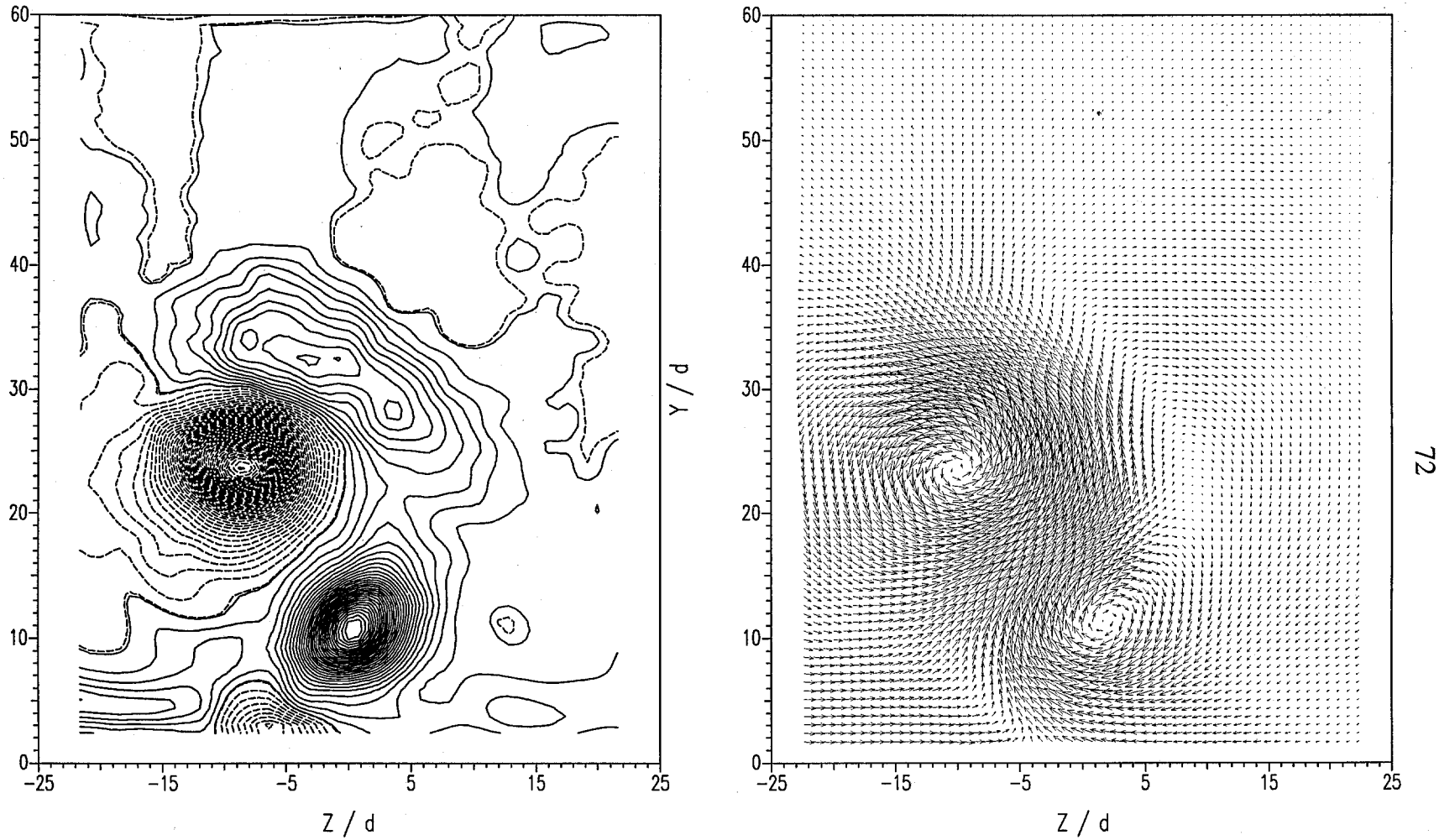

Figure 13. Mean vorticity and velocity fields, velocity ratio 10, Re = 4371 at X/d = 115 .

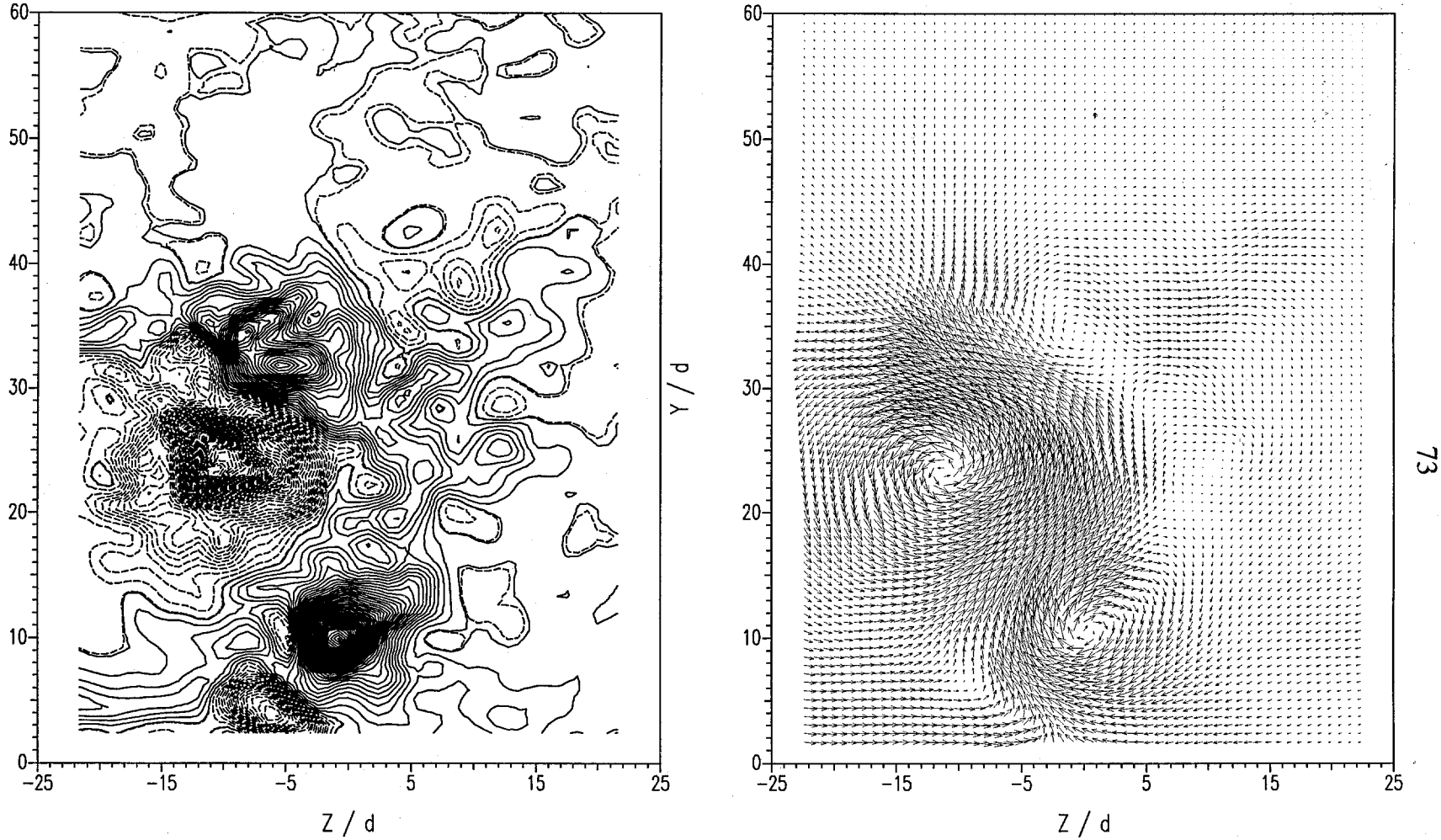

Figure 14a. First sequential (1 sec) average of vorticity and velocity fields, velocity ratio 10, Re = 4371 at X/d = 115.

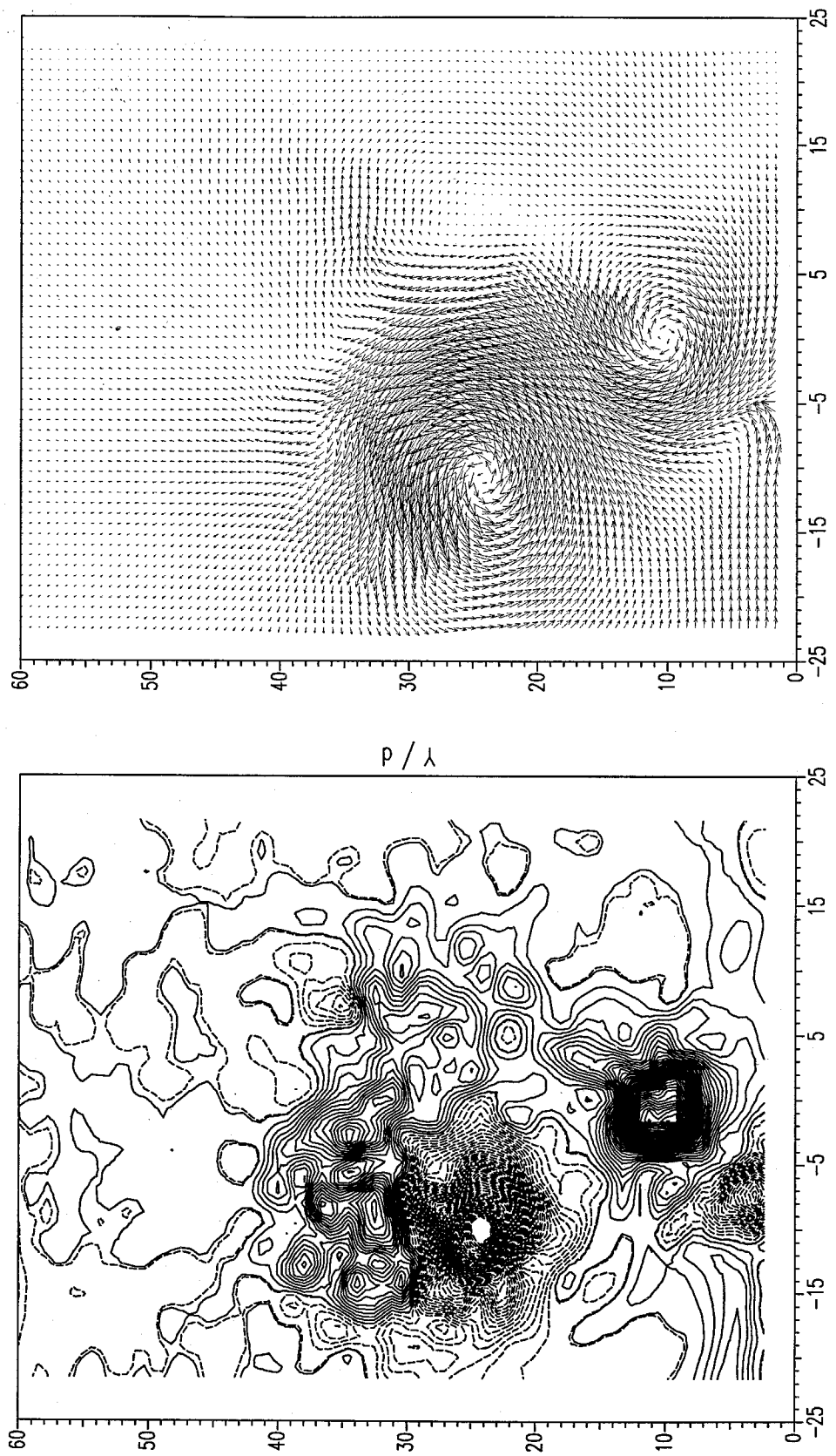

Figure 14b. Second sequential (1 sec) average of vorticity and velocity fields, velocity ratio 10, Re = 4371 at X/d = 115.

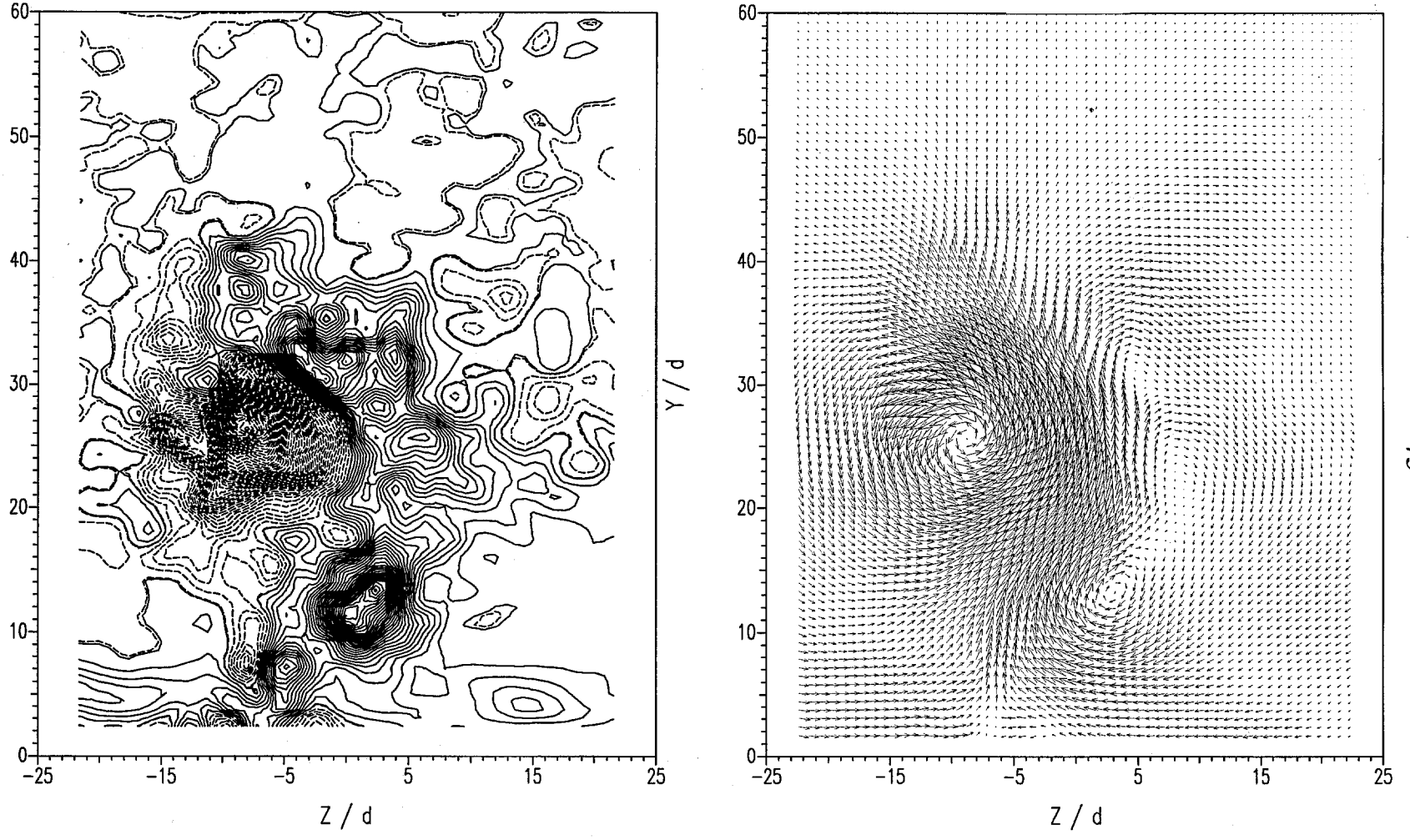

Figure 14c. Third sequential (1 sec) average of vorticity and velocity fields, velocity ratio 10, Re = 4371 at X/d = 115.

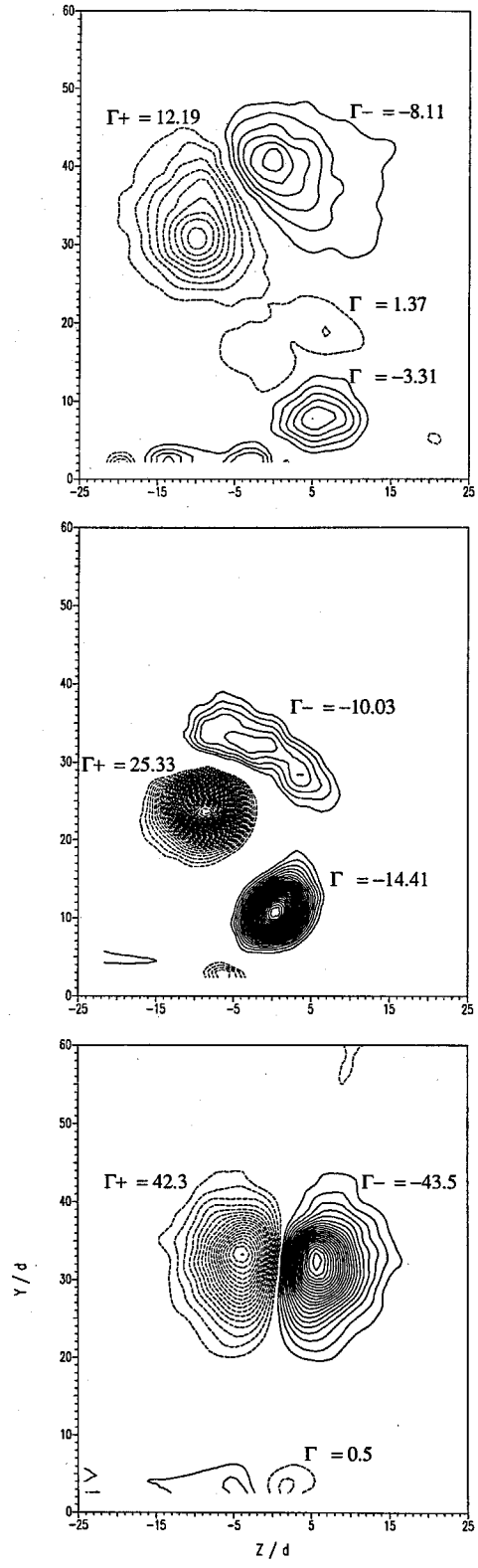

Figure 15. Measured values of circulation (in units: cm^2/sec) for the mean vorticity fields of figures 9, 11, and 13.

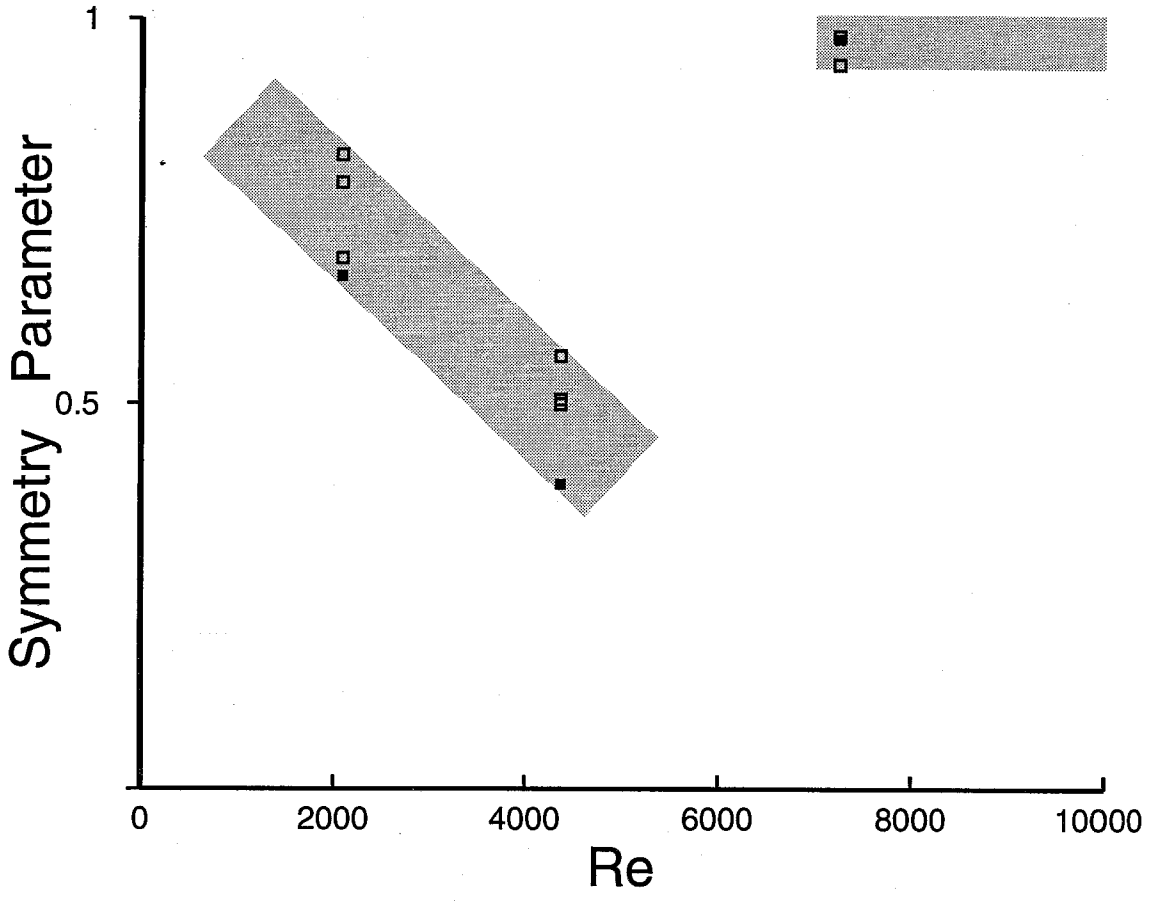

Figure 16. Symmetry Parameter for velocity ratio 10, as a function of Re.

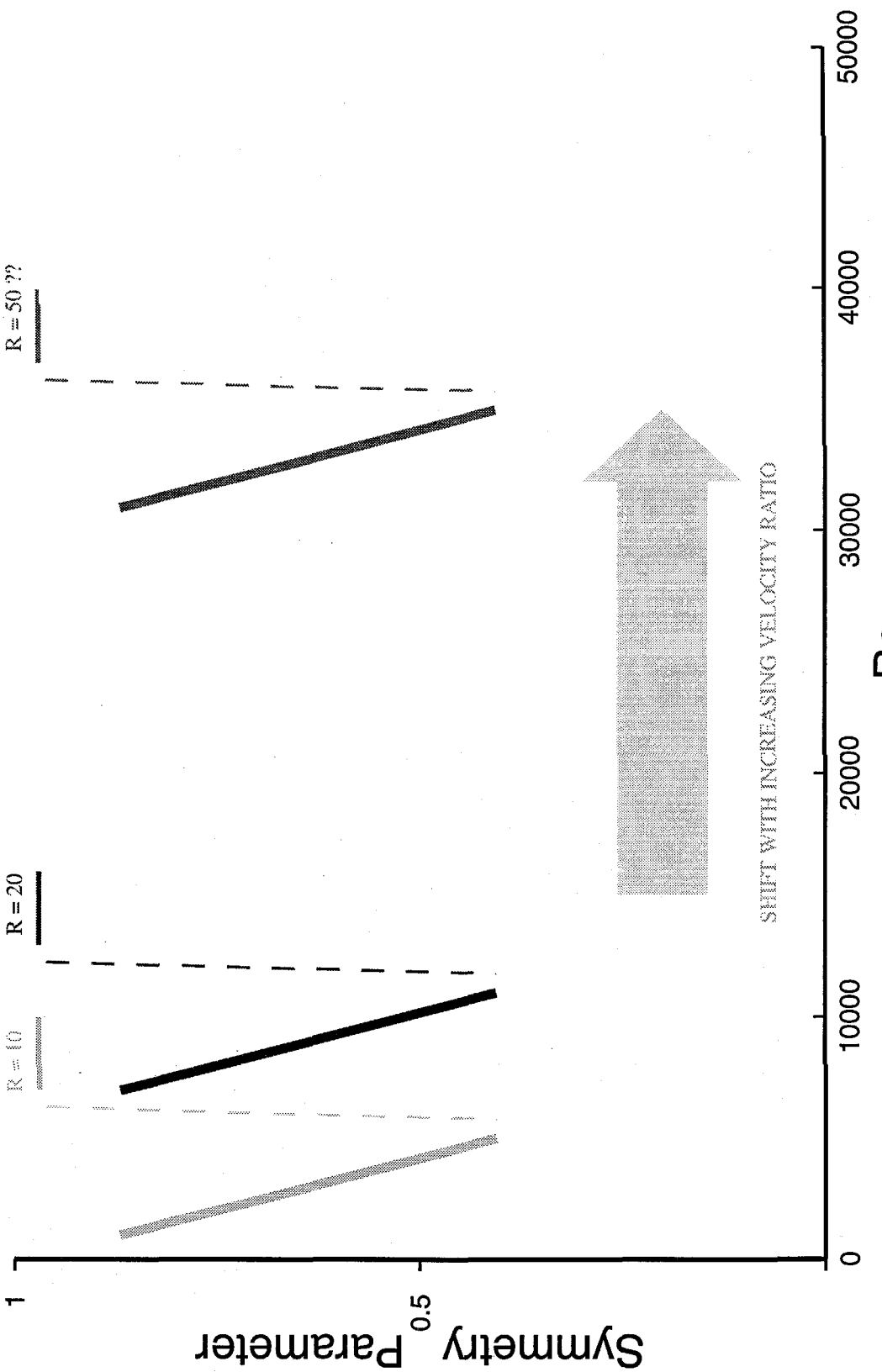

Figure 17a. Symmetry Parameter behavior with velocity ratio.

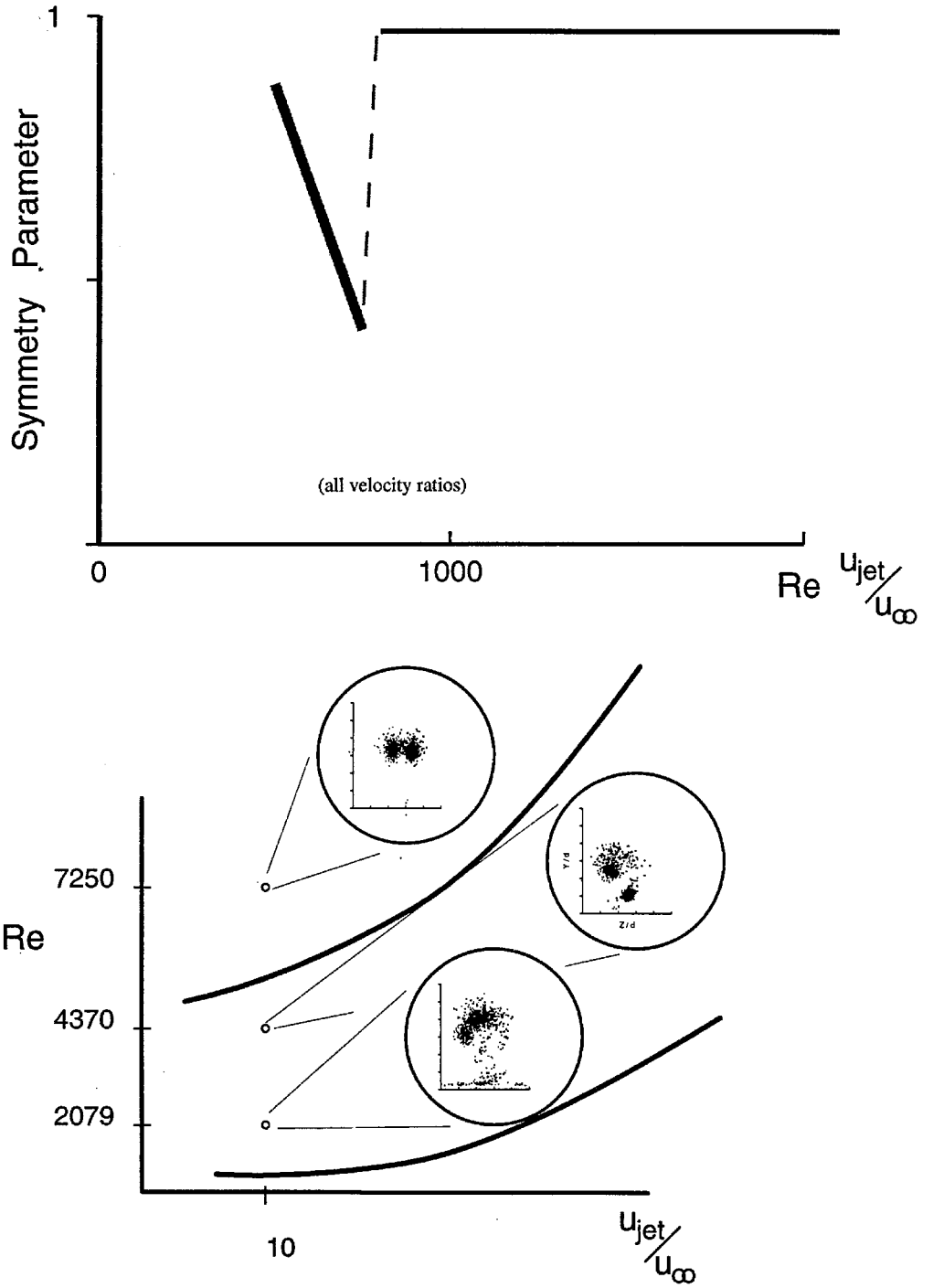

Figure 17b. Different aspects of the alternate mean flow states: (top) rescaling the abscissa with the velocity ratio; (bottom) the existence domain in velocity ratio - Re space.

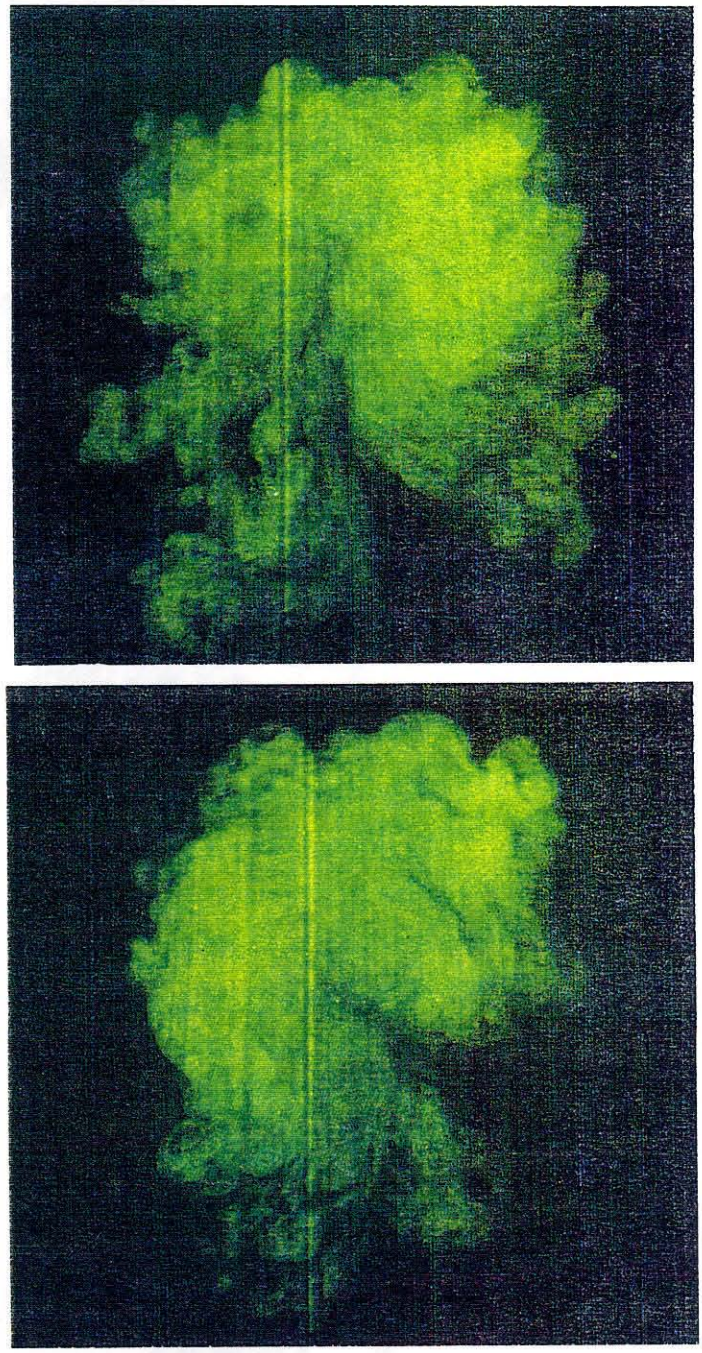

Figure 18. Flow visualization of the transverse jet in an unsteady asymmetric flow state. These cross section views, using LIF and taken in quick succession, show the unsteady behavior of the primary vortices. As little flow marker is entrained by the tertiary vortices, evidence of their presence is not obvious.

Figure 19. LIF visualization of a transverse jet in the side view. Tertiary vortices roll up before the vortex pair, and can be noted in this view on the jet center plane residing at a lower trajectory.

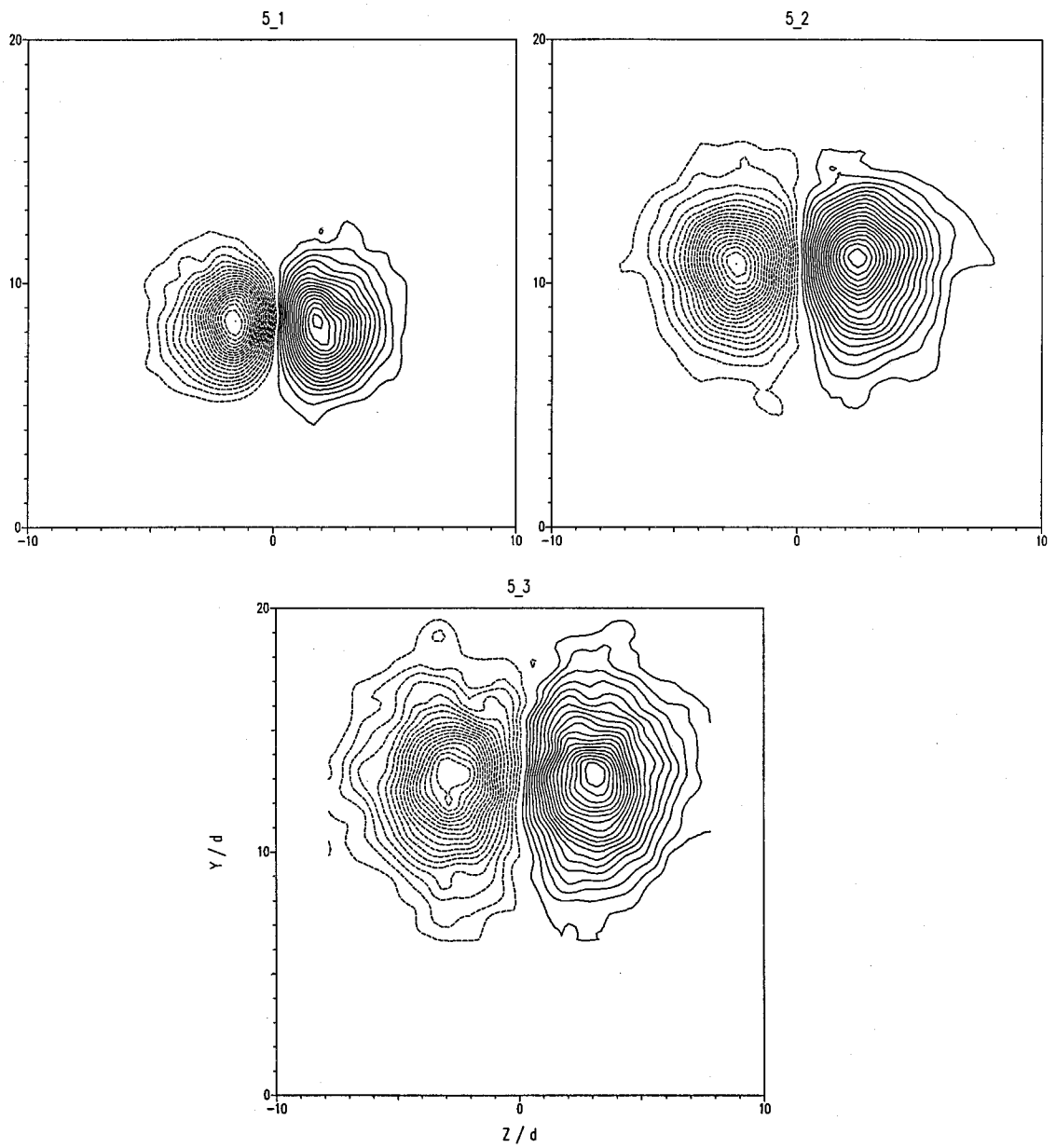

Figure 20a. The mean vorticity field in the cross section for velocity ratio 5: 5_1 X/d = 18.3 ; 5_2 X/d = 40.8 ; 5_3 X/d = 74.2 .

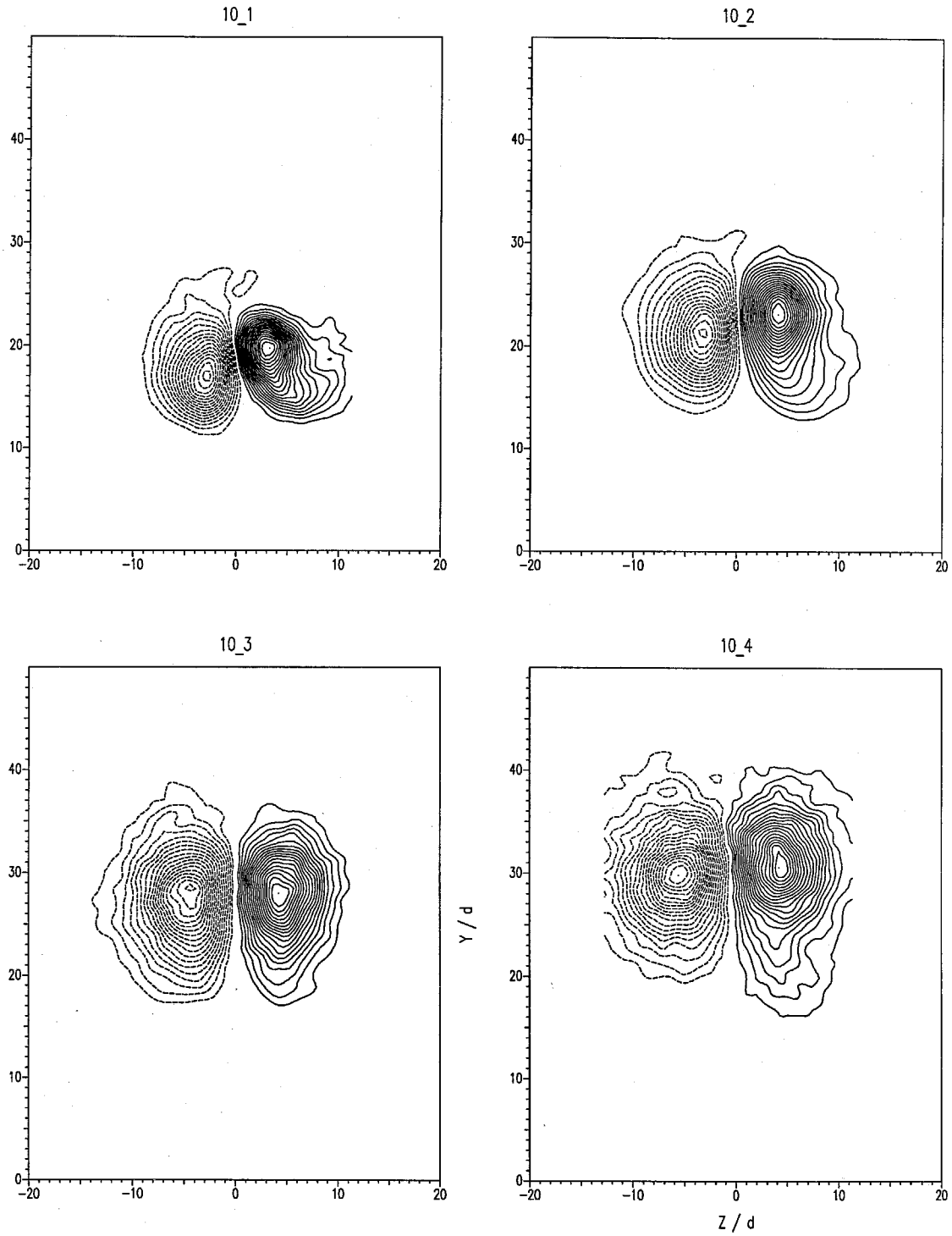

Figure 20b. The mean vorticity field in the cross section for velocity ratio 10:
10_1 X/d = 28.8 ; 10_2 X/d = 49.2 ; 10_3 X/d = 86.4 ; 10_4 X/d = 112.

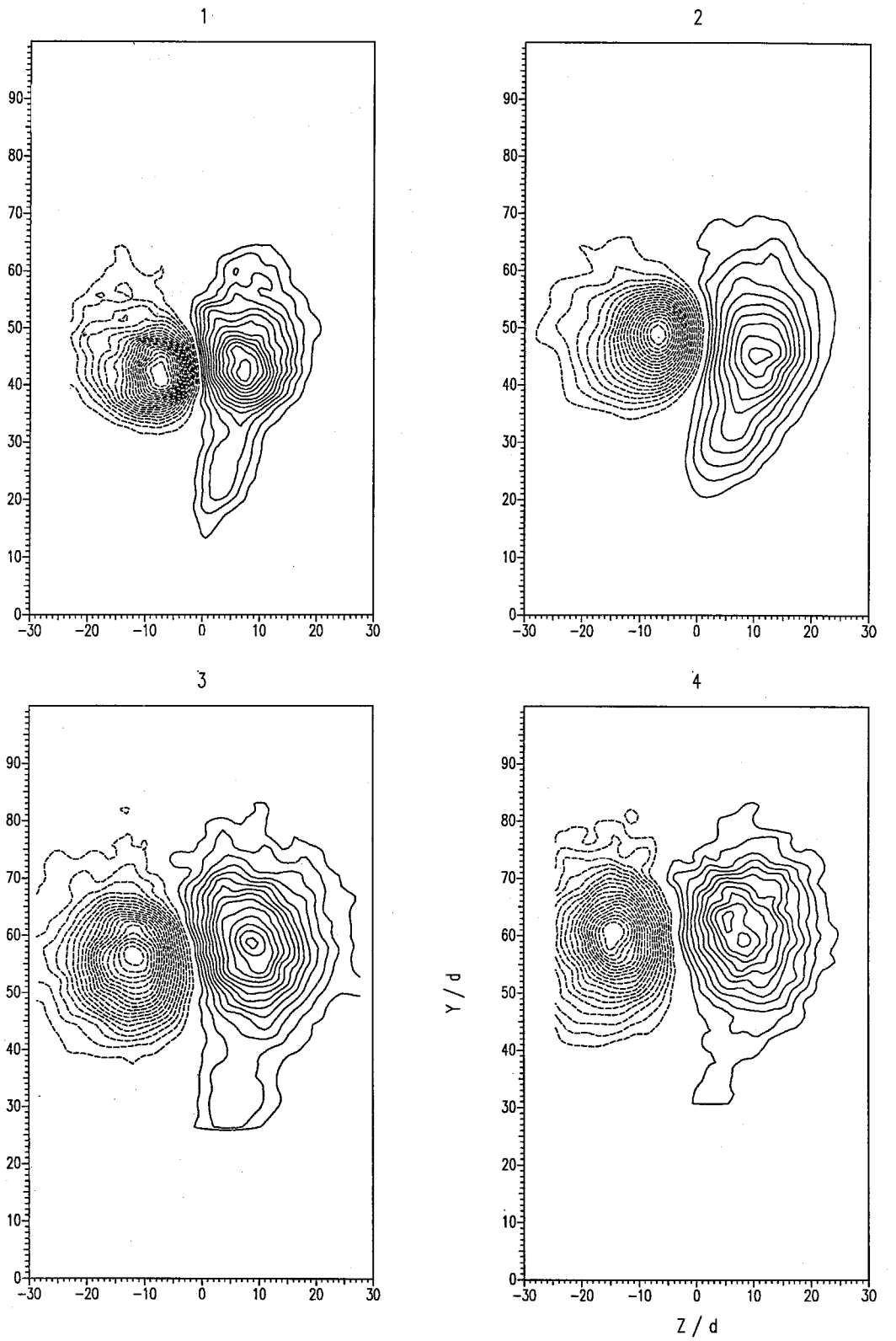

Figure 20c. The mean vorticity field in the cross section for velocity ratio 20: 1 X/d = 73.7 ; 2 X/d = 115. ; 3 X/d = 191. ; 4 X/d = 243.

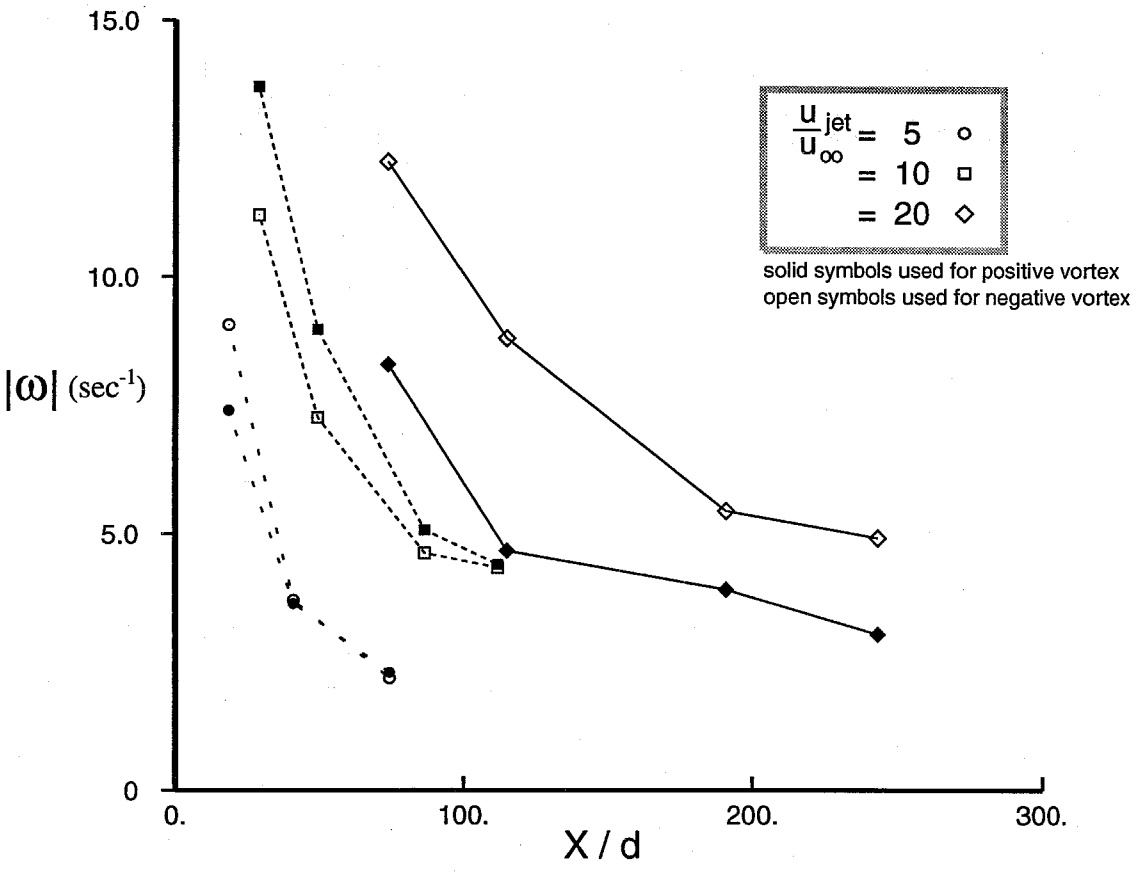

Figure 21. Measured peak vorticity magnitude in the cross section.

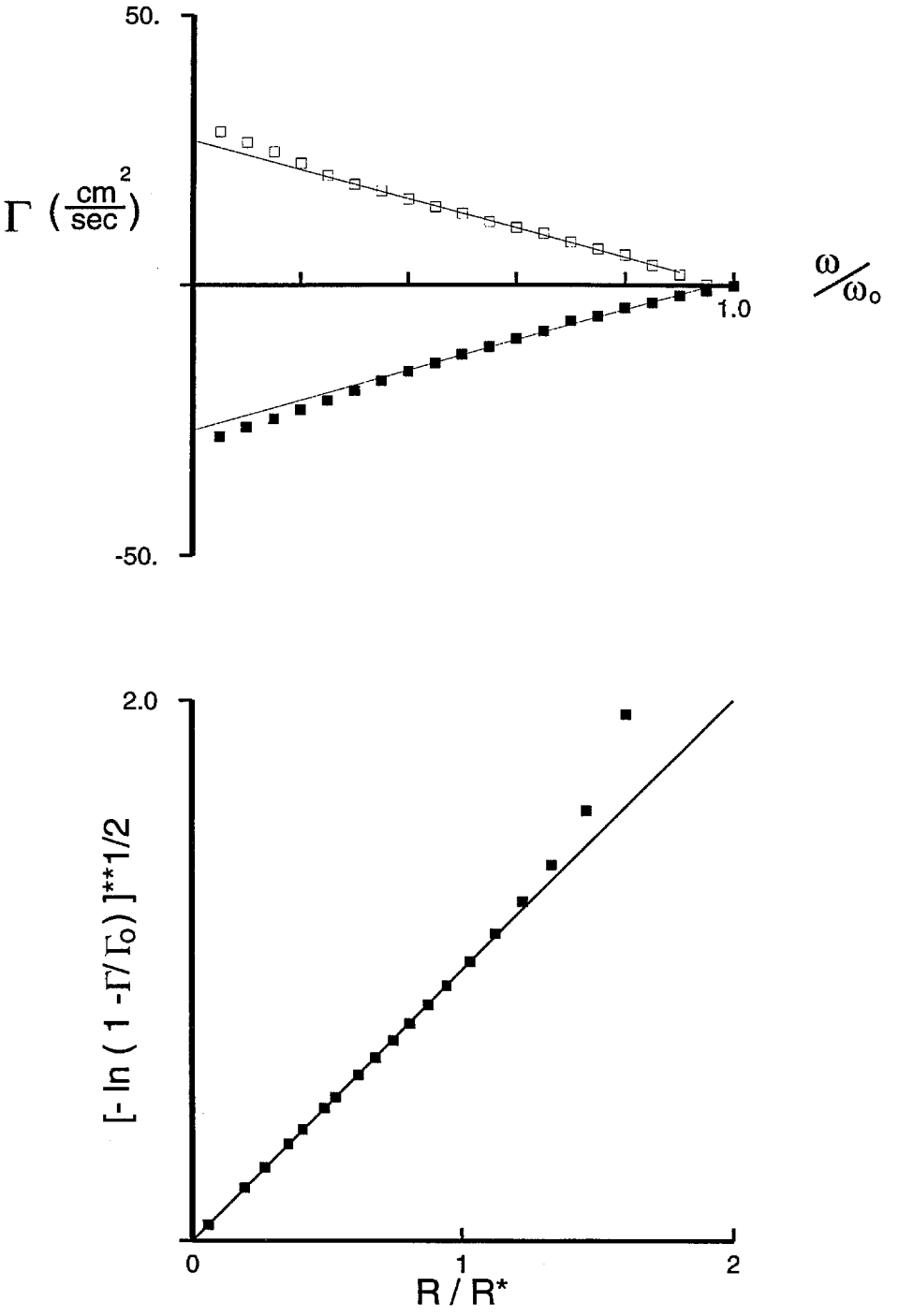

Figure 22. A typical circulation distribution within a vortex.

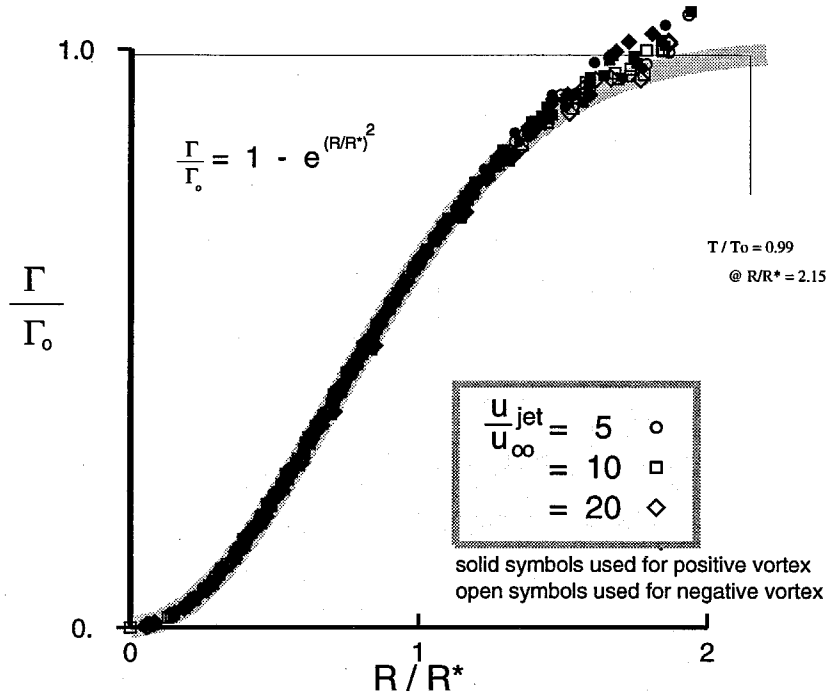

Figure 23. Variation of measured vortex circulation with equivalent radius.

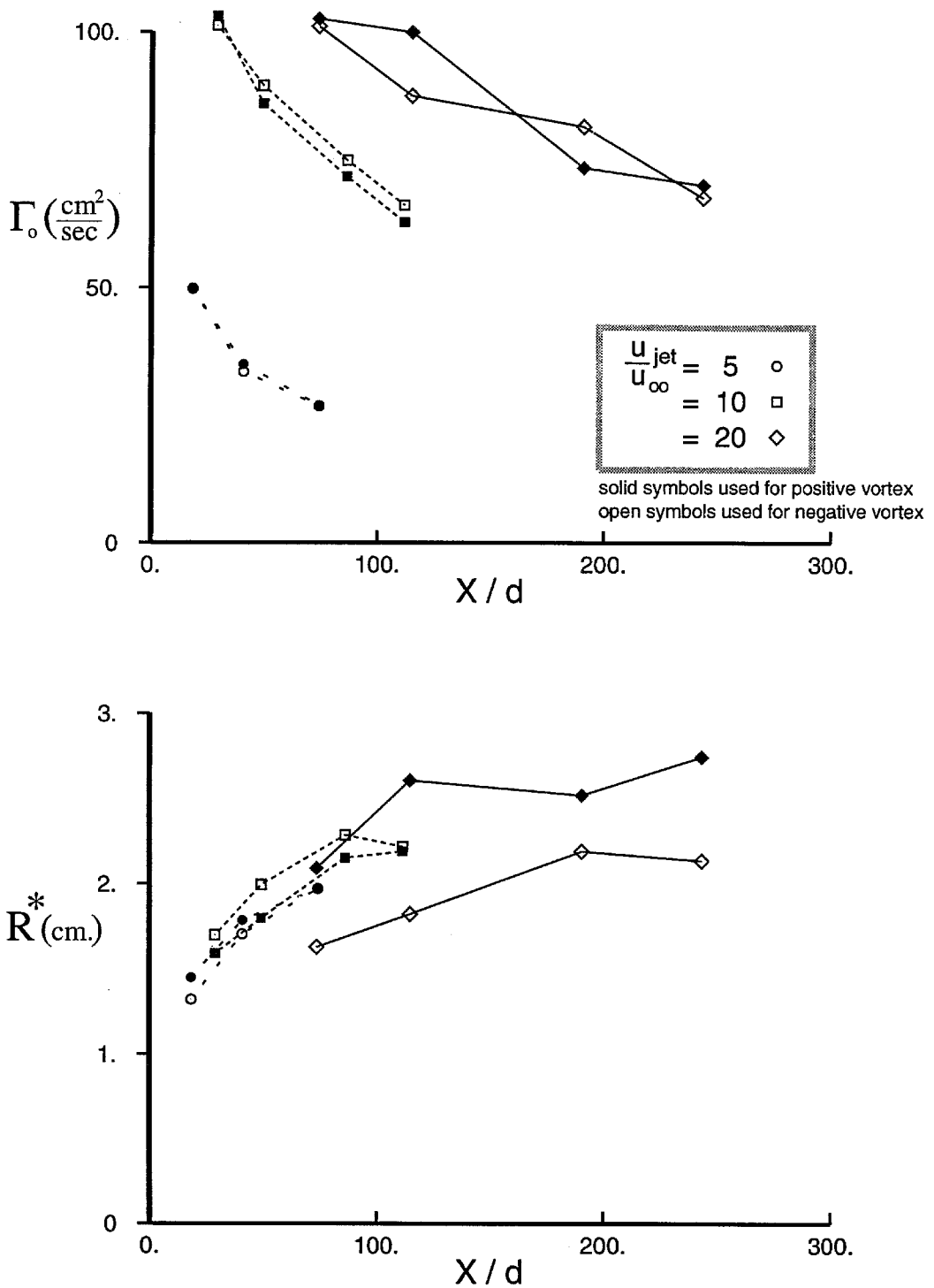

Figure 24. Measured values of circulation (top) and size (bottom).

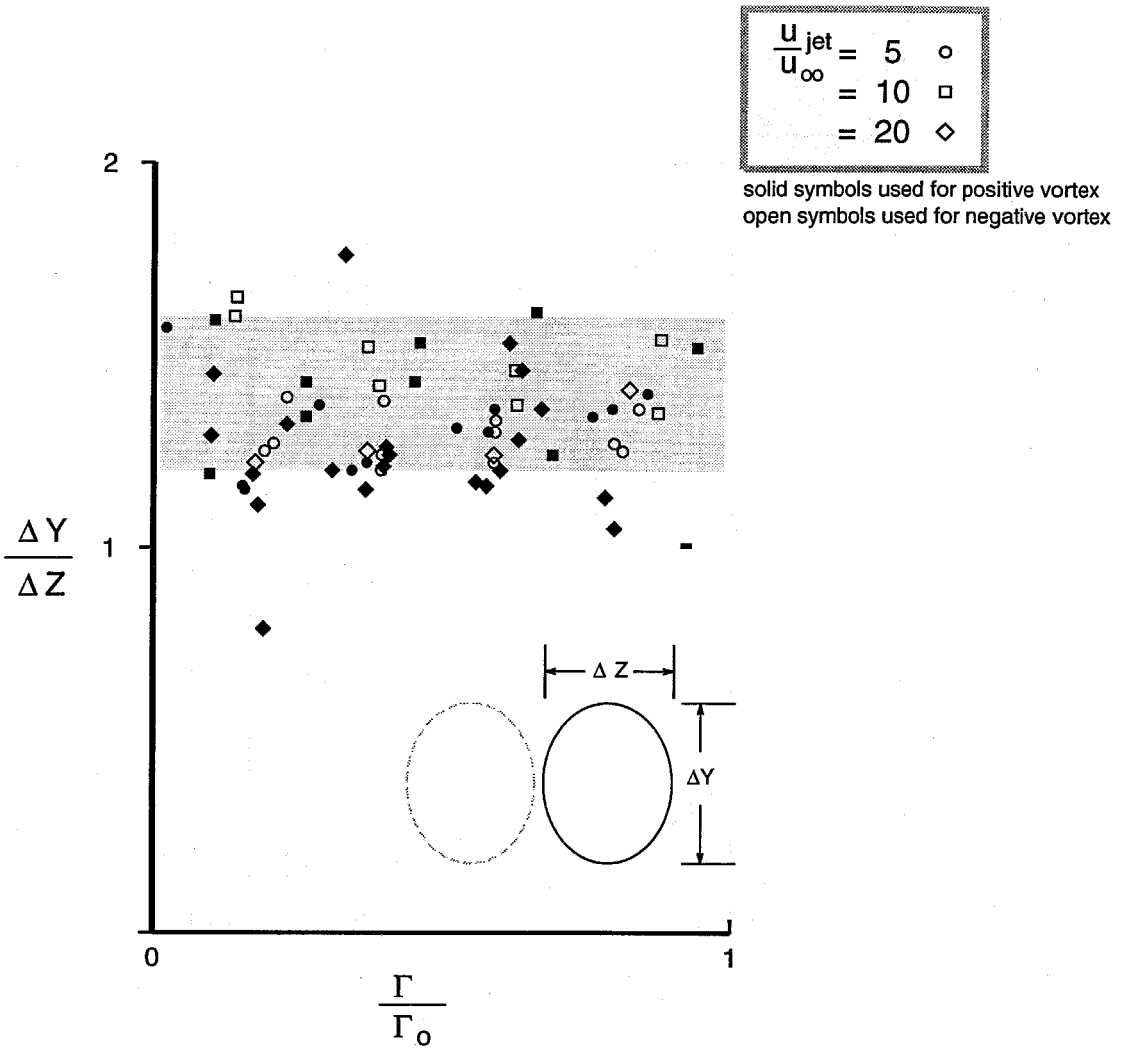

Figure 25. Measured eccentricity of vortex area.

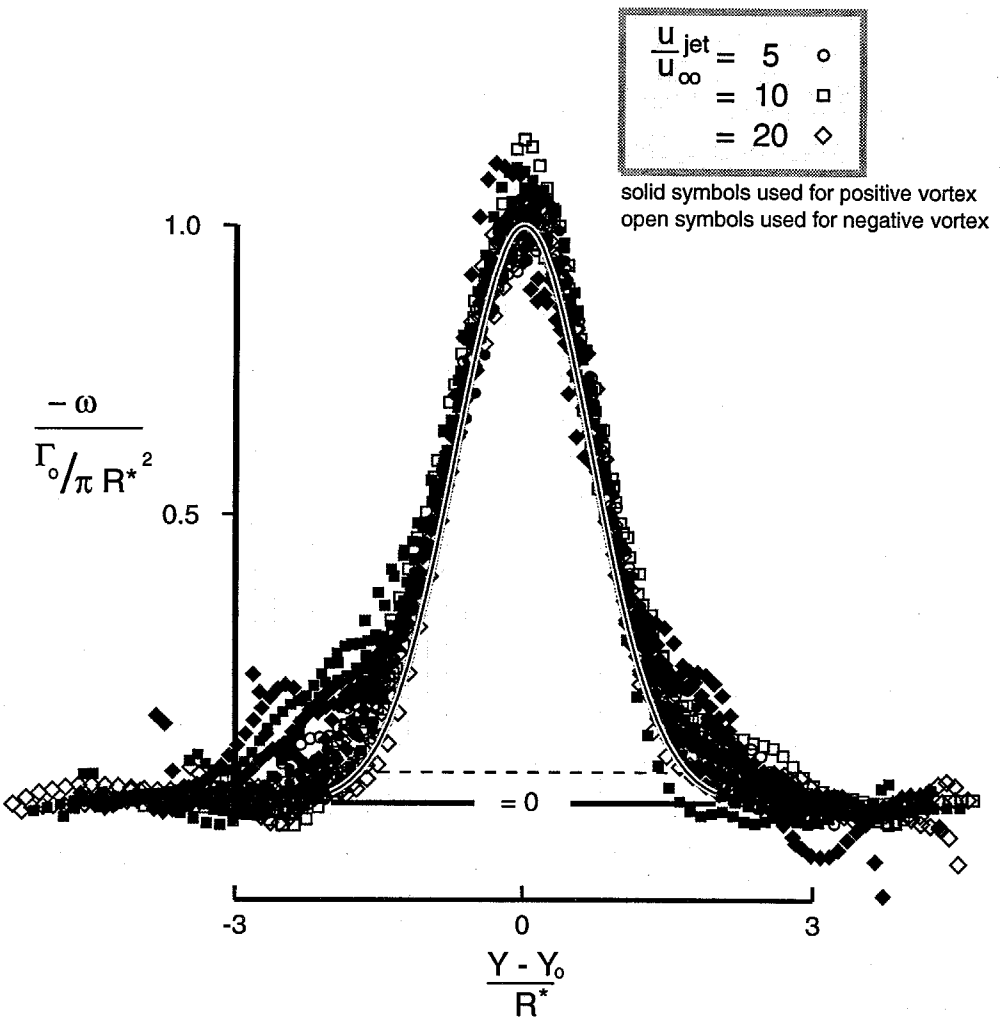

Figure 26. Measured vorticity distribution along Y - axis.

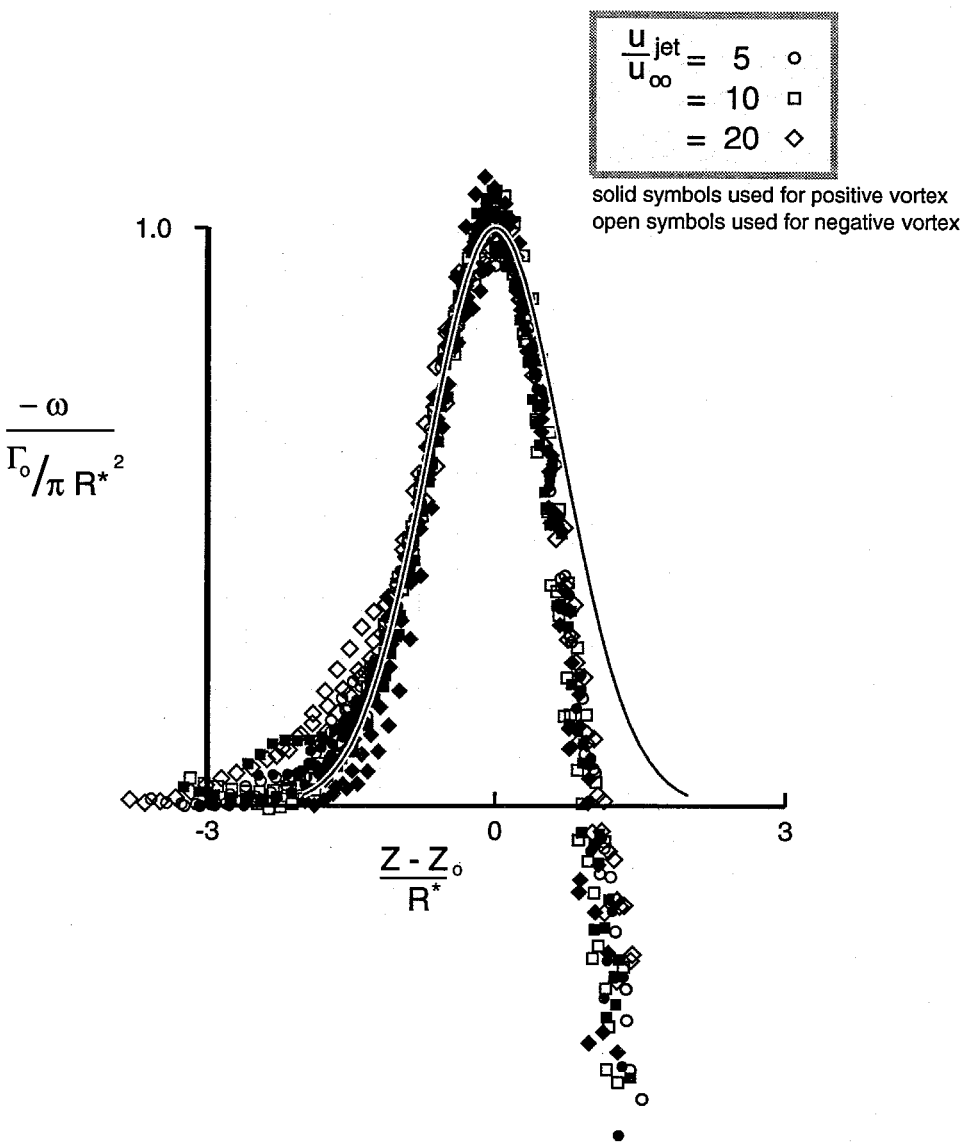

Figure 27. Measured vorticity distribution along Z - axis.

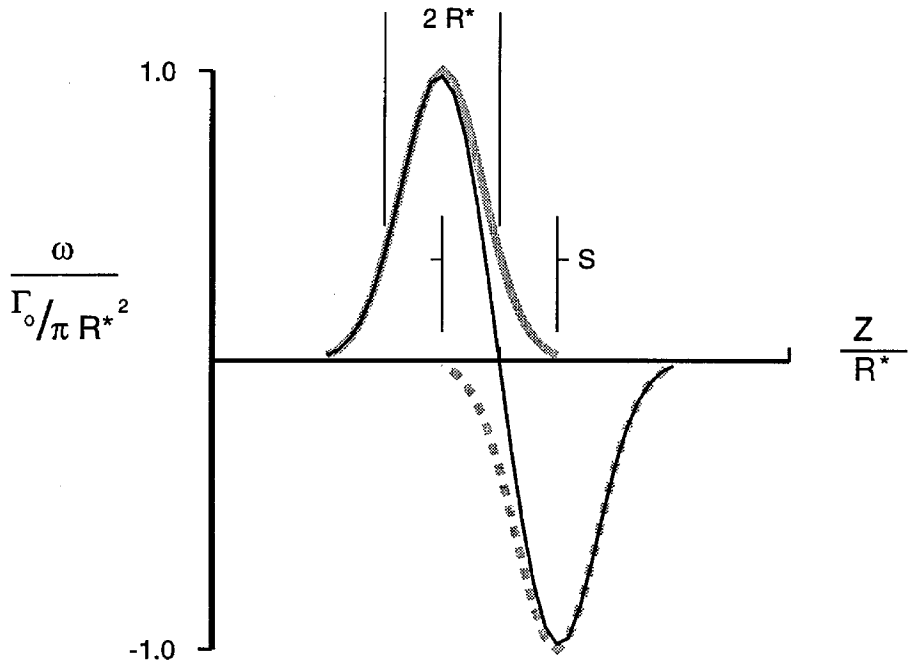

Figure 28. The superposition of two Gaussian vorticity fields.

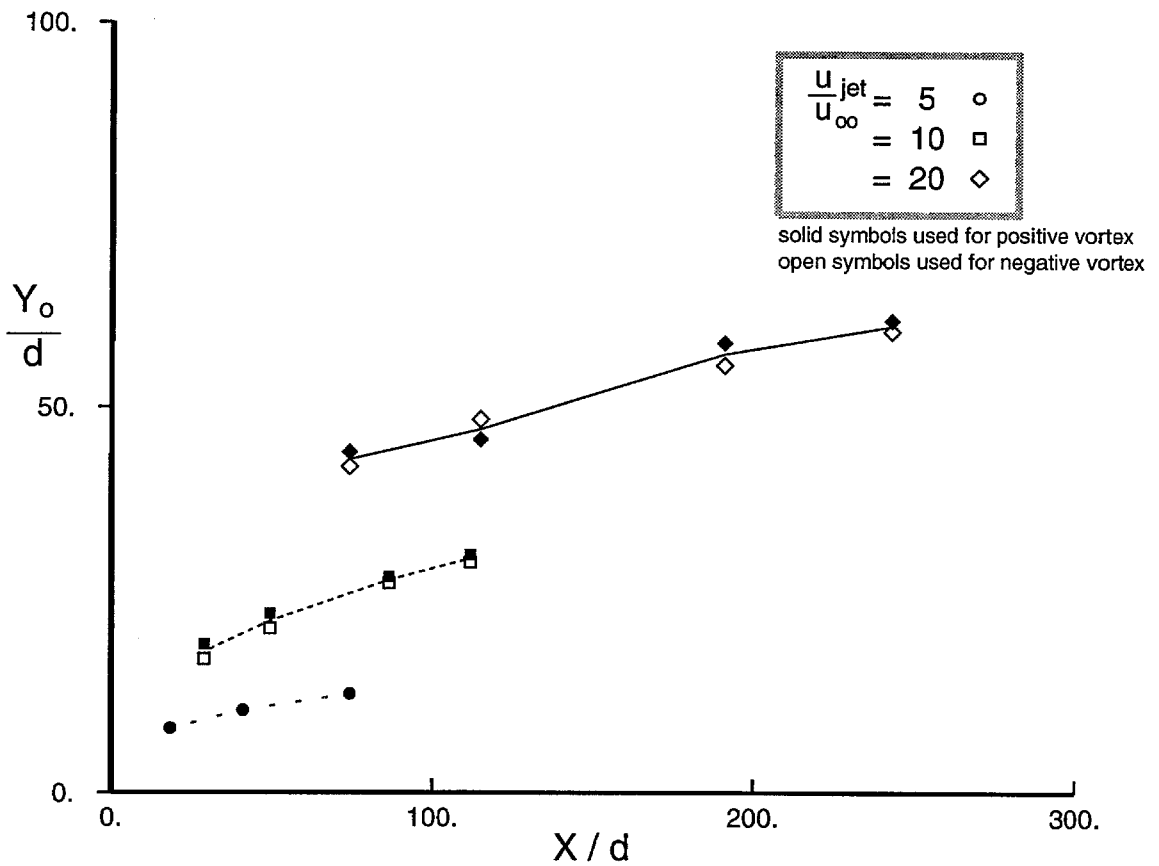

Figure 29. Measurements of Yo -- the jet trajectory.

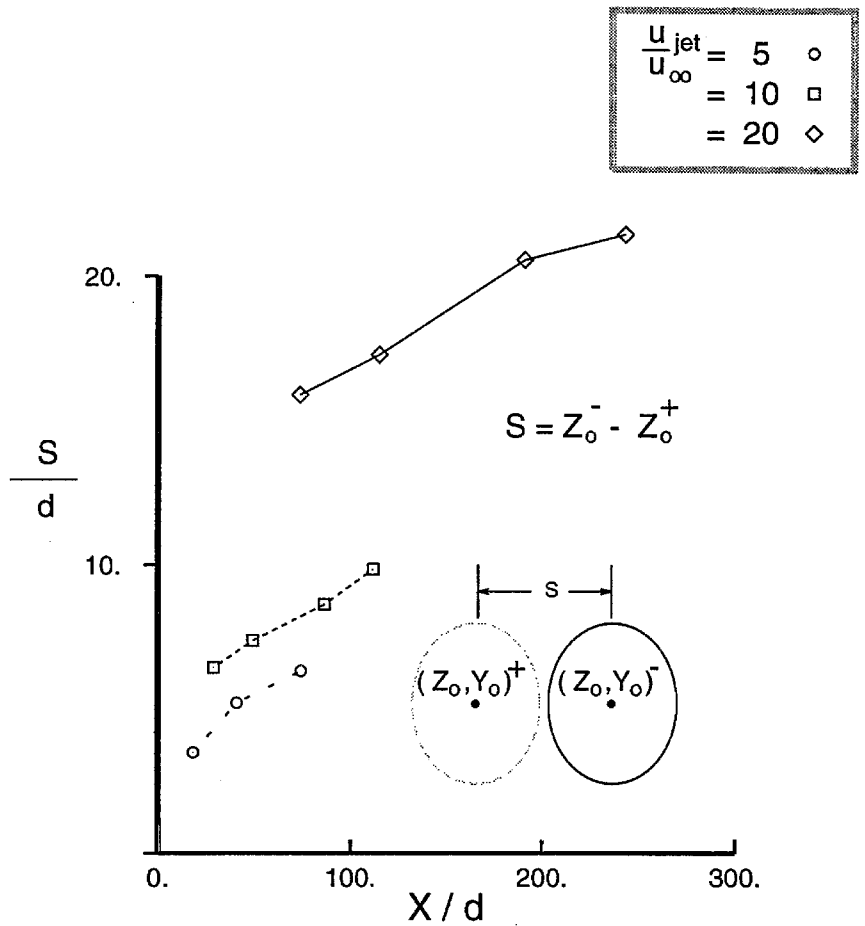

Figure 30. Measurement of vortex separation.

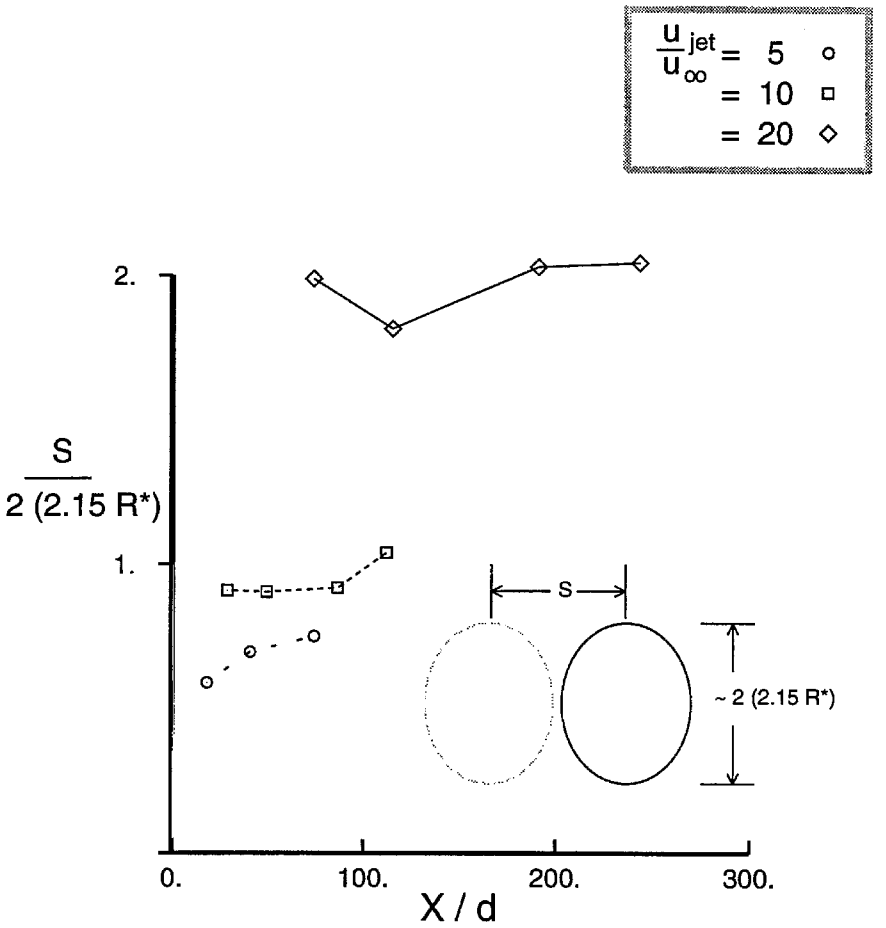

Figure 31. Test for geometric similitude.

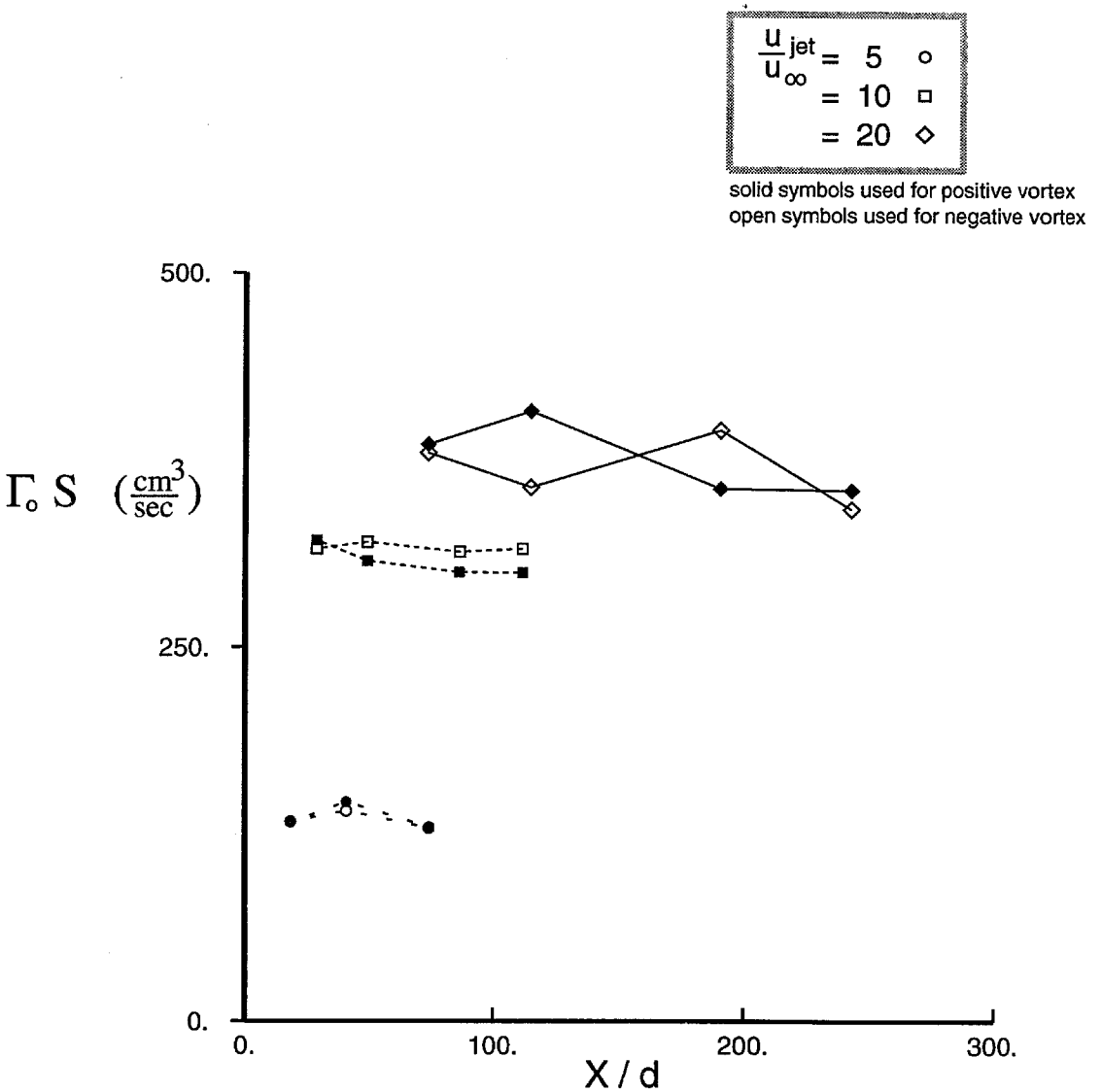

Figure 32. Plot of $\Gamma_o S$ versus streamwise distance.

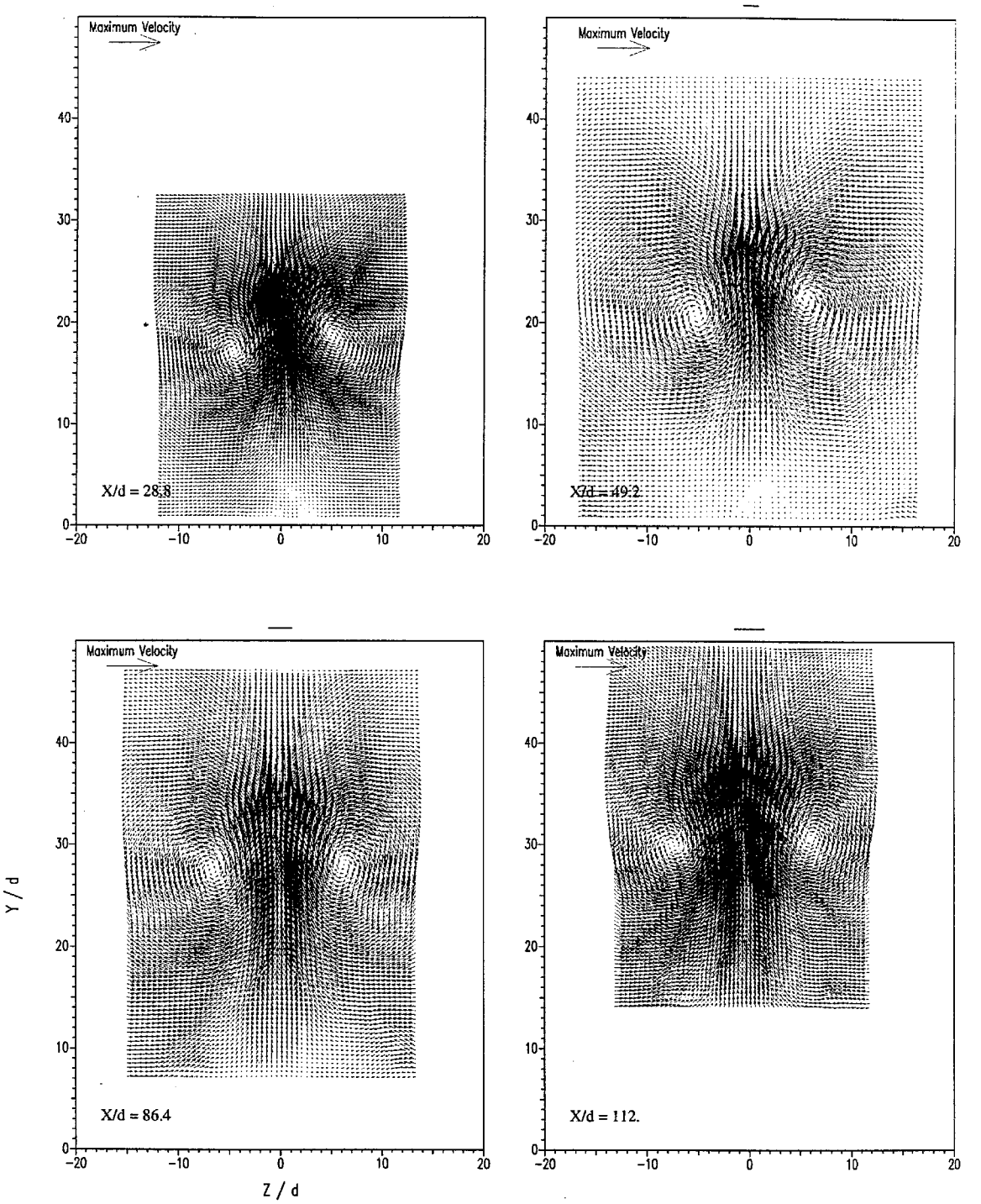

Figure 33. Mean velocity fields for velocity ratio 10.

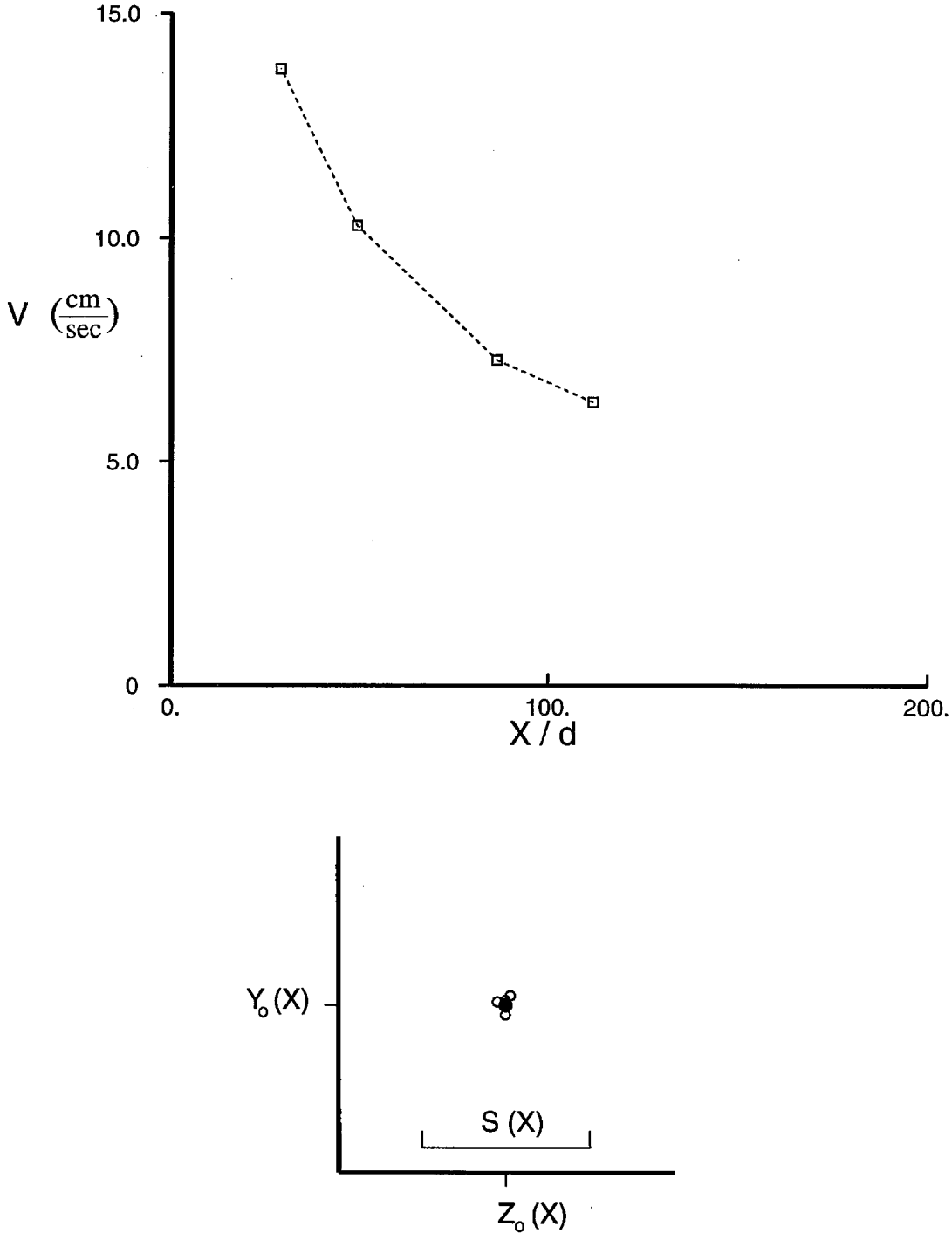

Figure 34. Measured values of V(x) (top). The location, in the cross section, of the point of maximum velocity (bottom). Locations shown as open circles, while the midpoint between the two streamwise vortices shown as a solid circle.

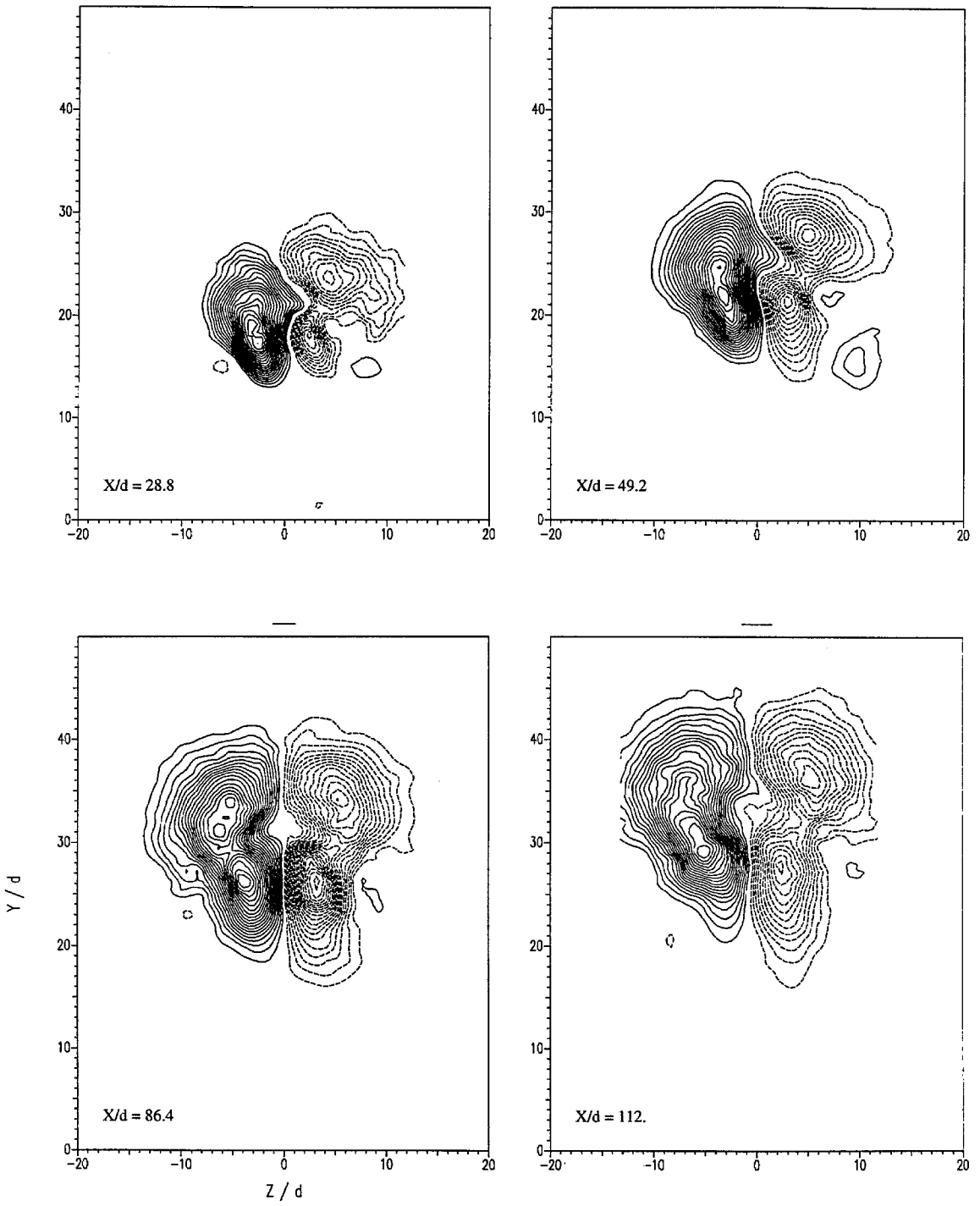

Figure 35. Correlation $\overline{v'w'}$ distribution for velocity ratio 10.

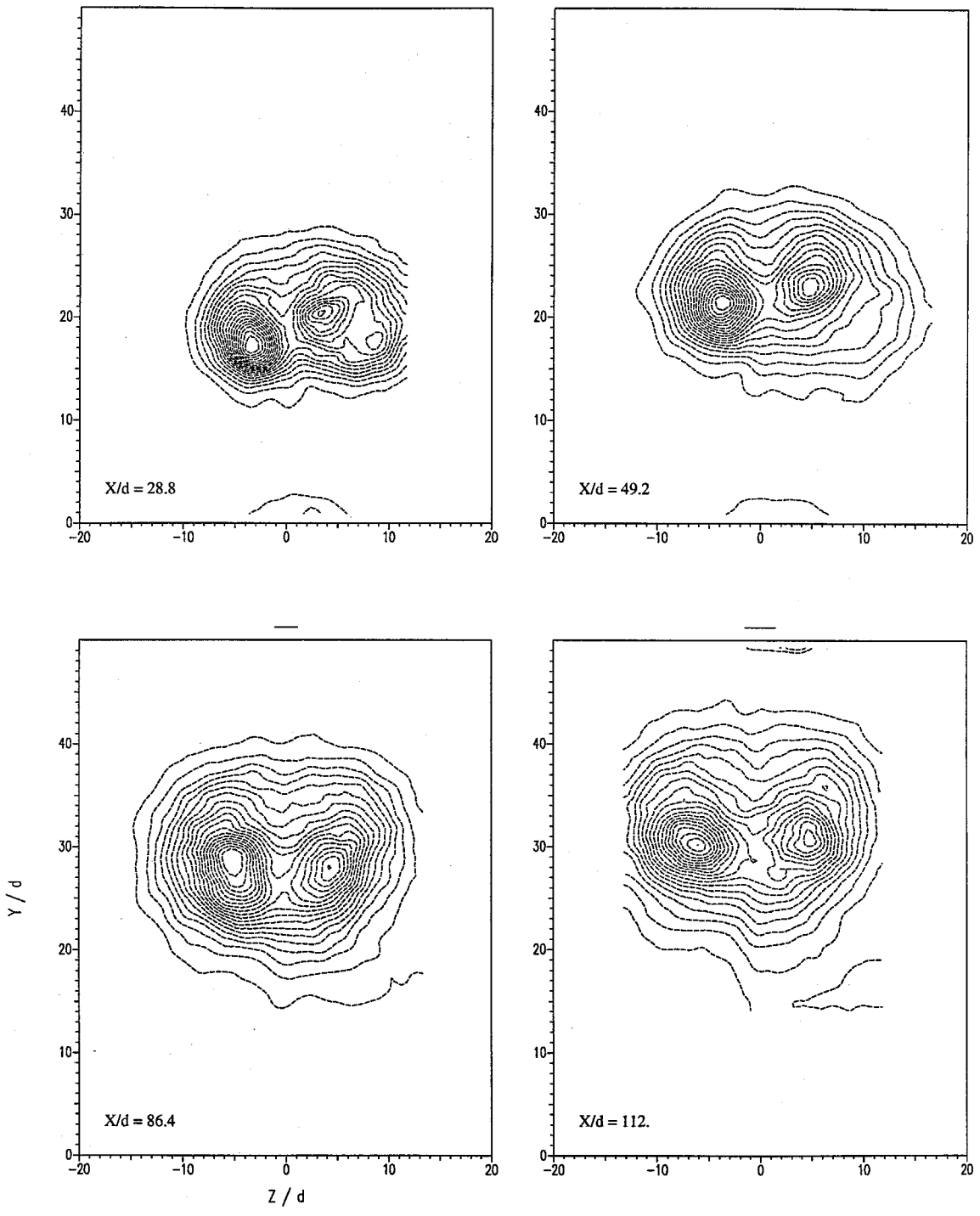

Figure 36a. Distribution of $\overline{v'^2}$ for velocity ratio 10.

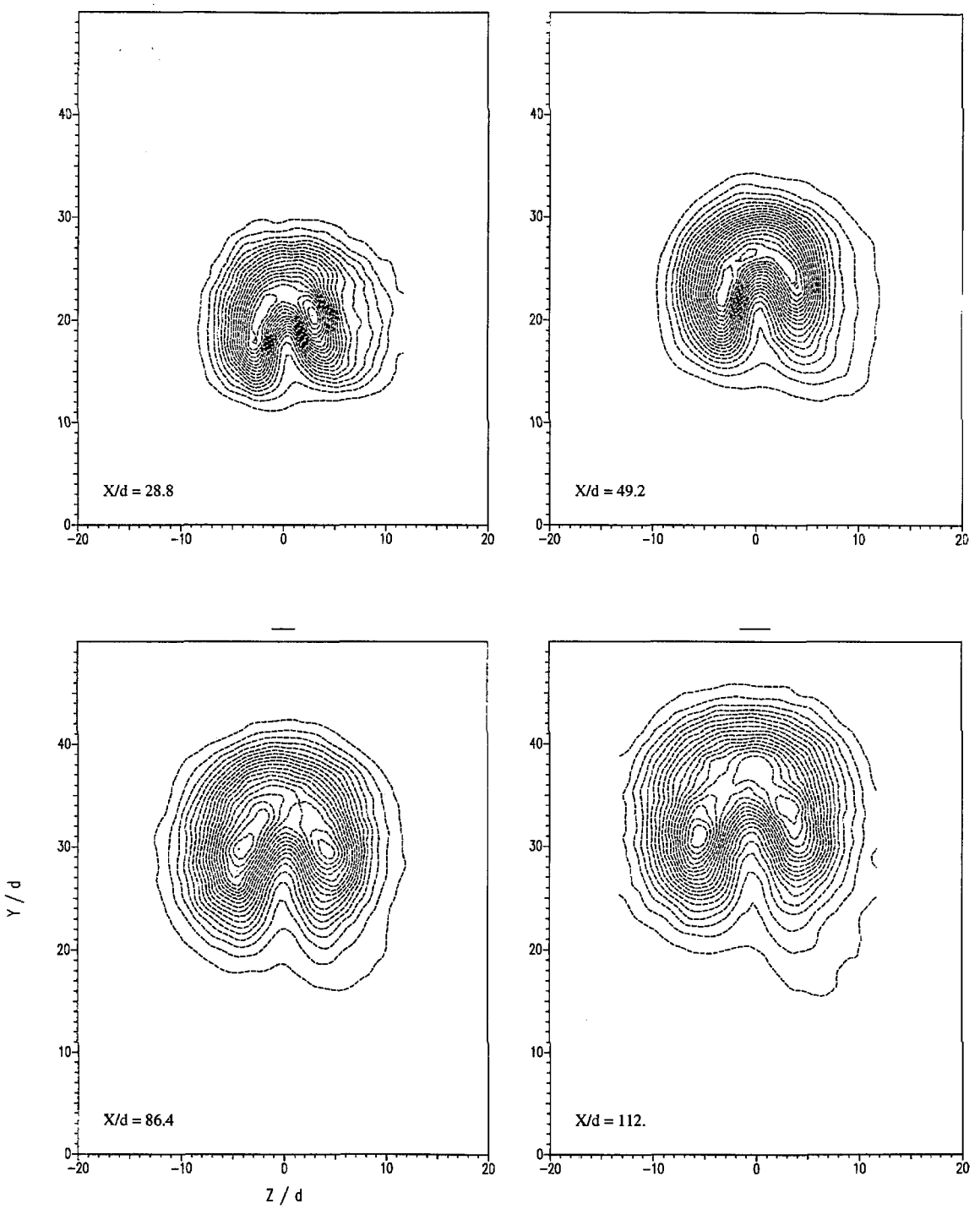

Figure 36b. Distribution of $\overline{w'^2}$ for velocity ratio 10.

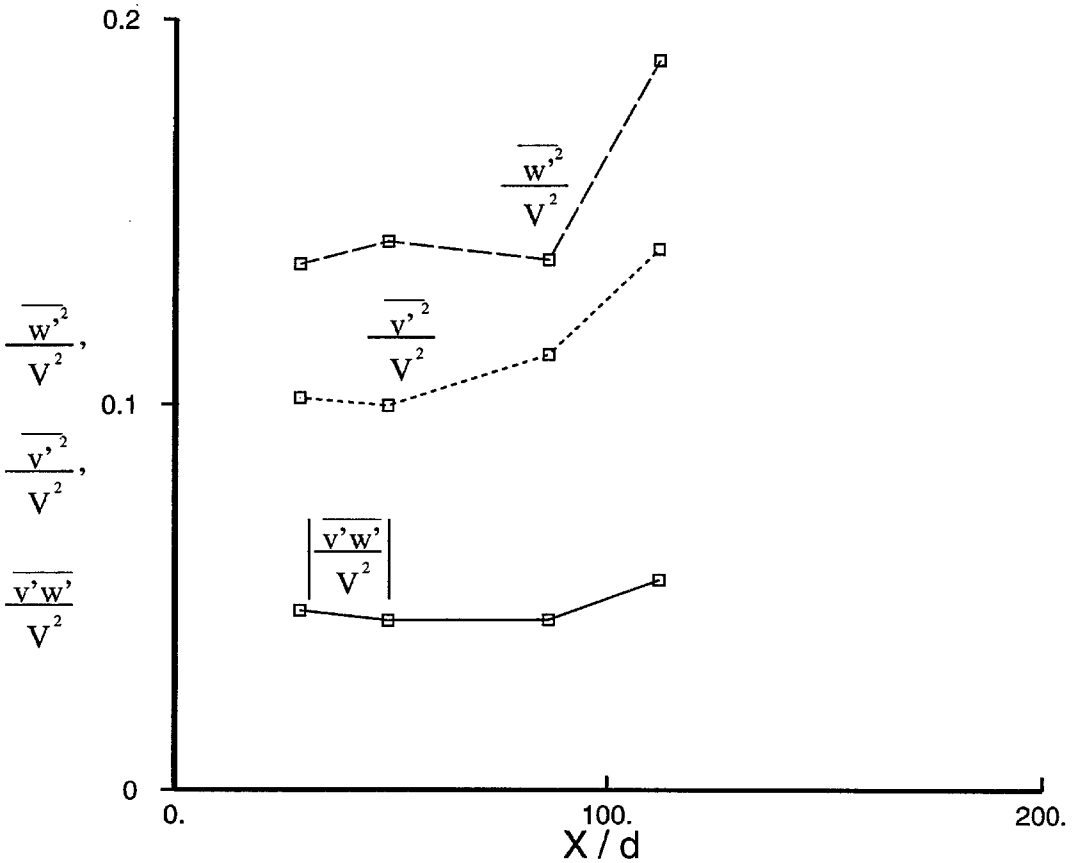

Figure 36c: Peak values of turbulence quantities in the cross section.

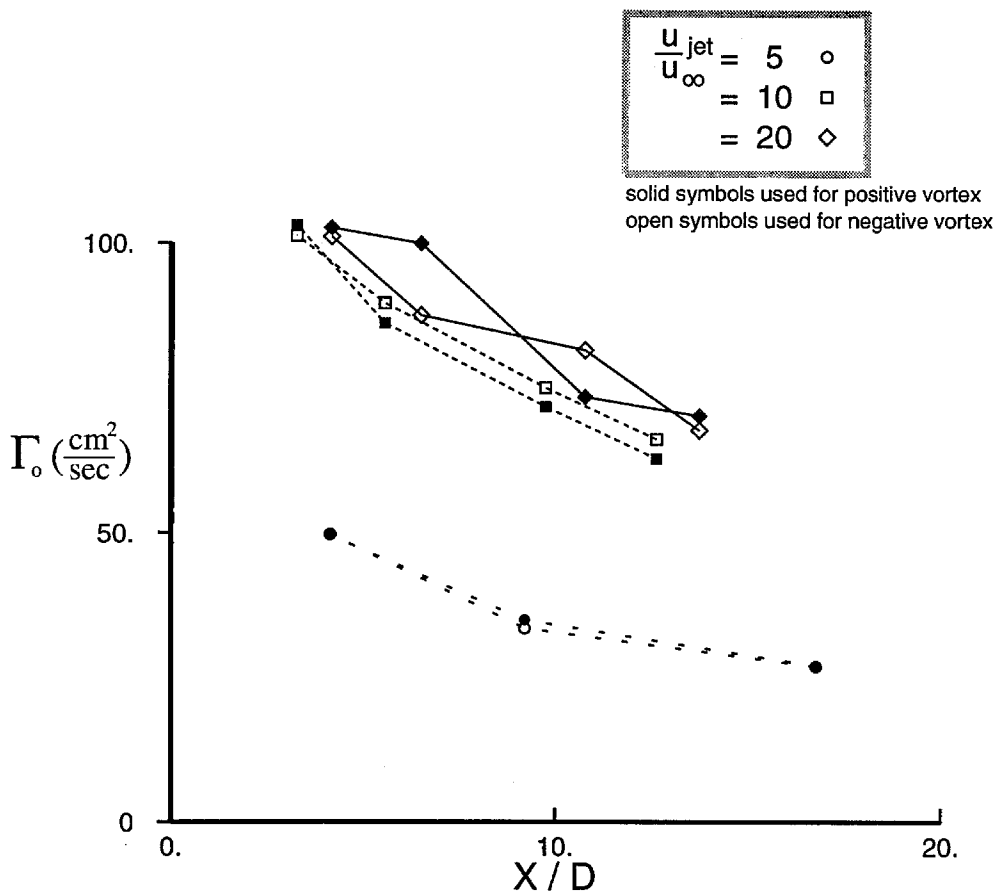

Figure 37. Circulation as a function of X/D .

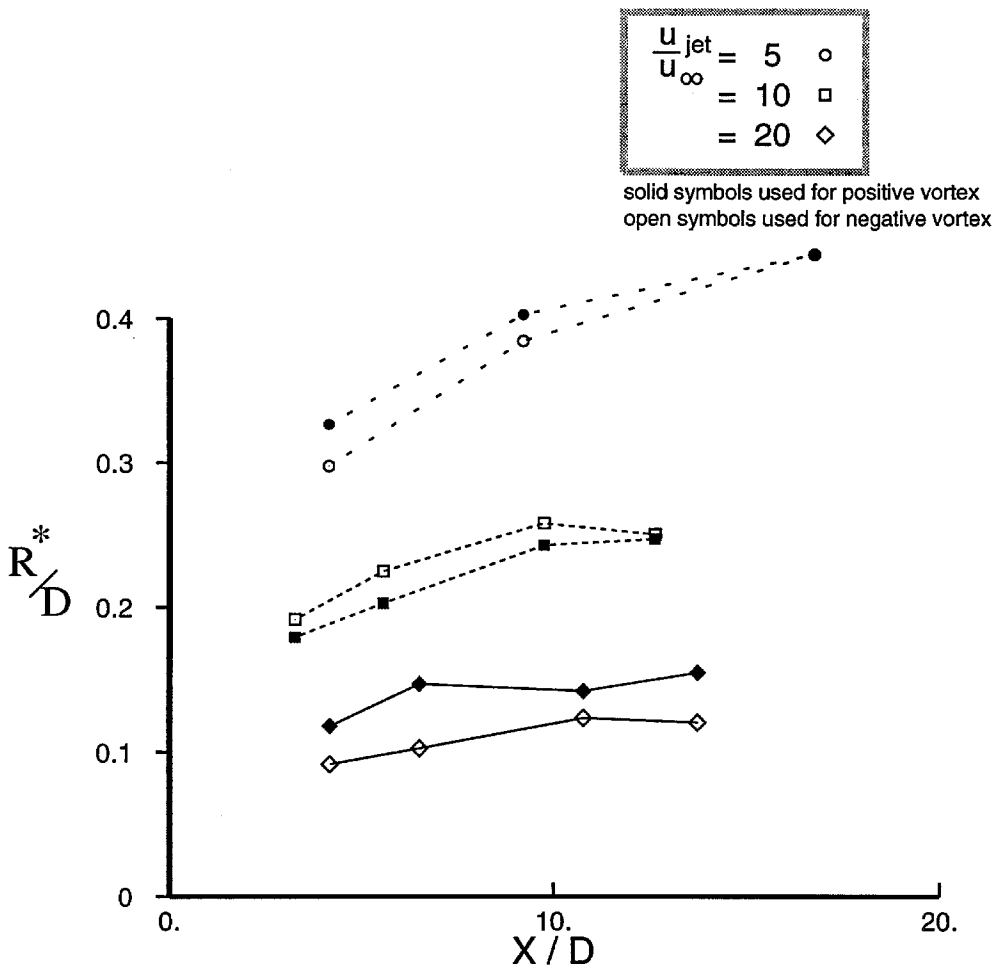

Figure 38. Normalized vortex size.

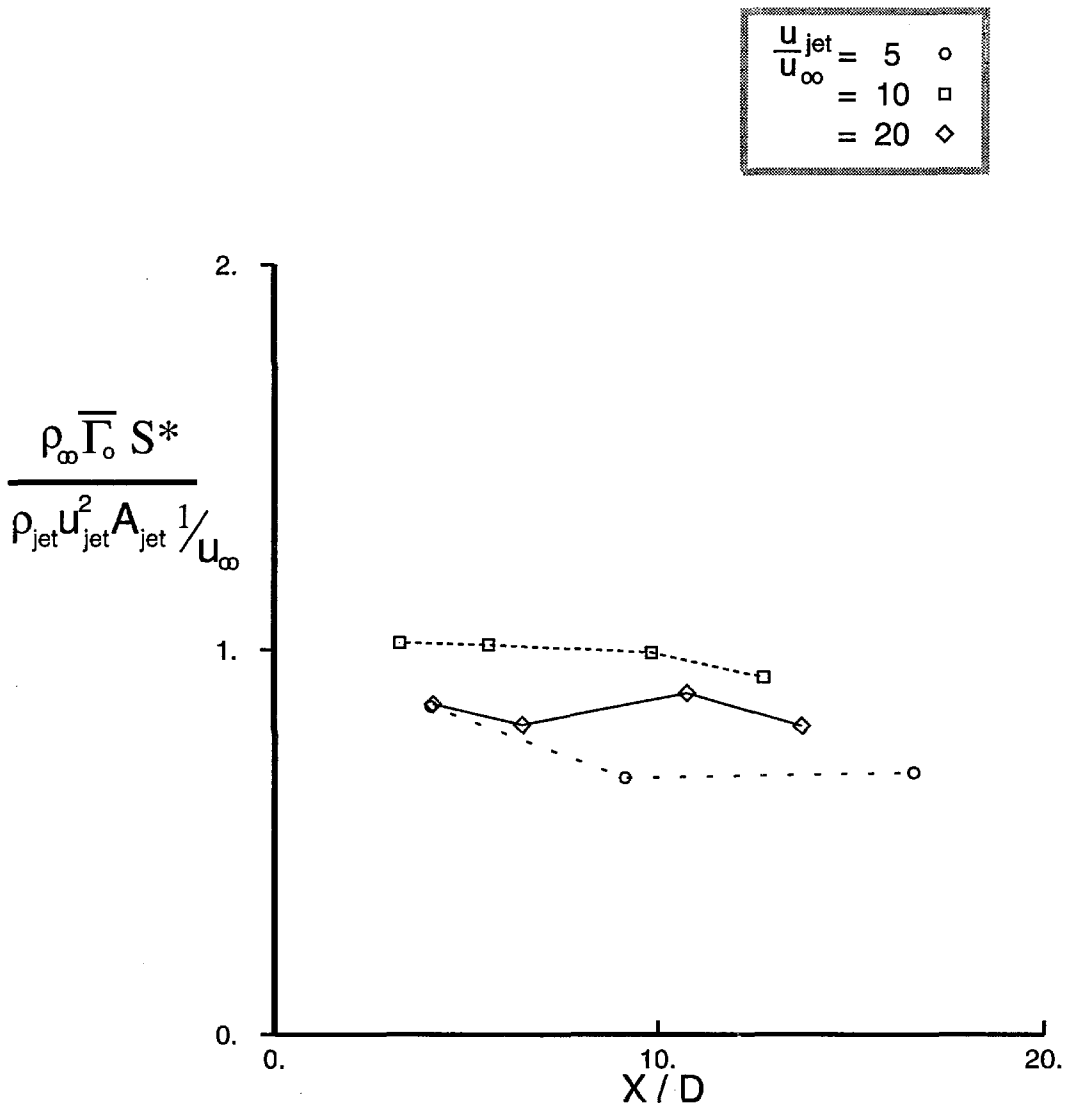

Figure 39a. Normalized jet impulse, estimated as the product of (average) circulation and the separation (S*) of the positive and negative vorticity centroids.

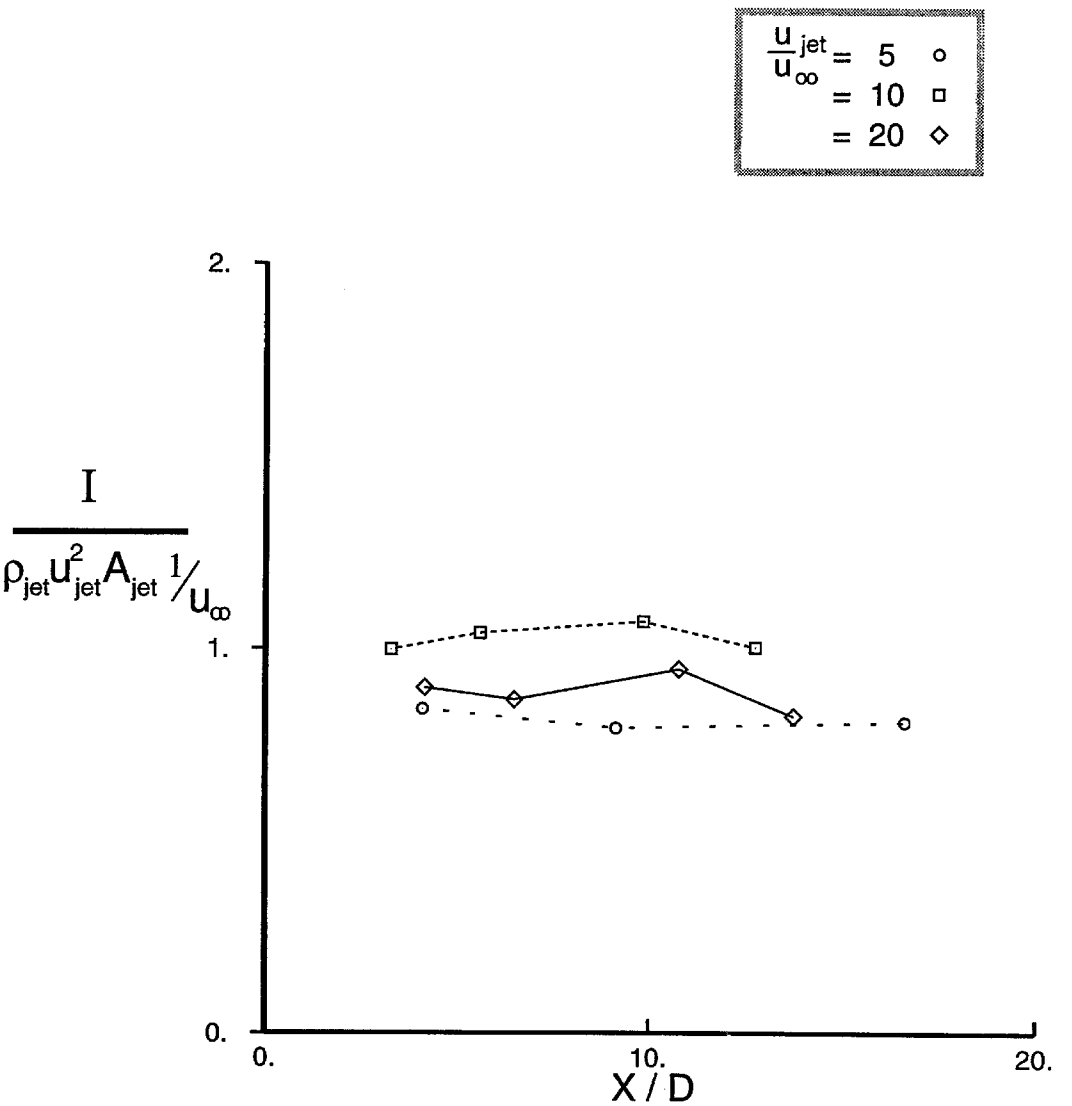

Figure 39b. Normalized jet impulse, evaluated by direct integration over entire measurement domain.

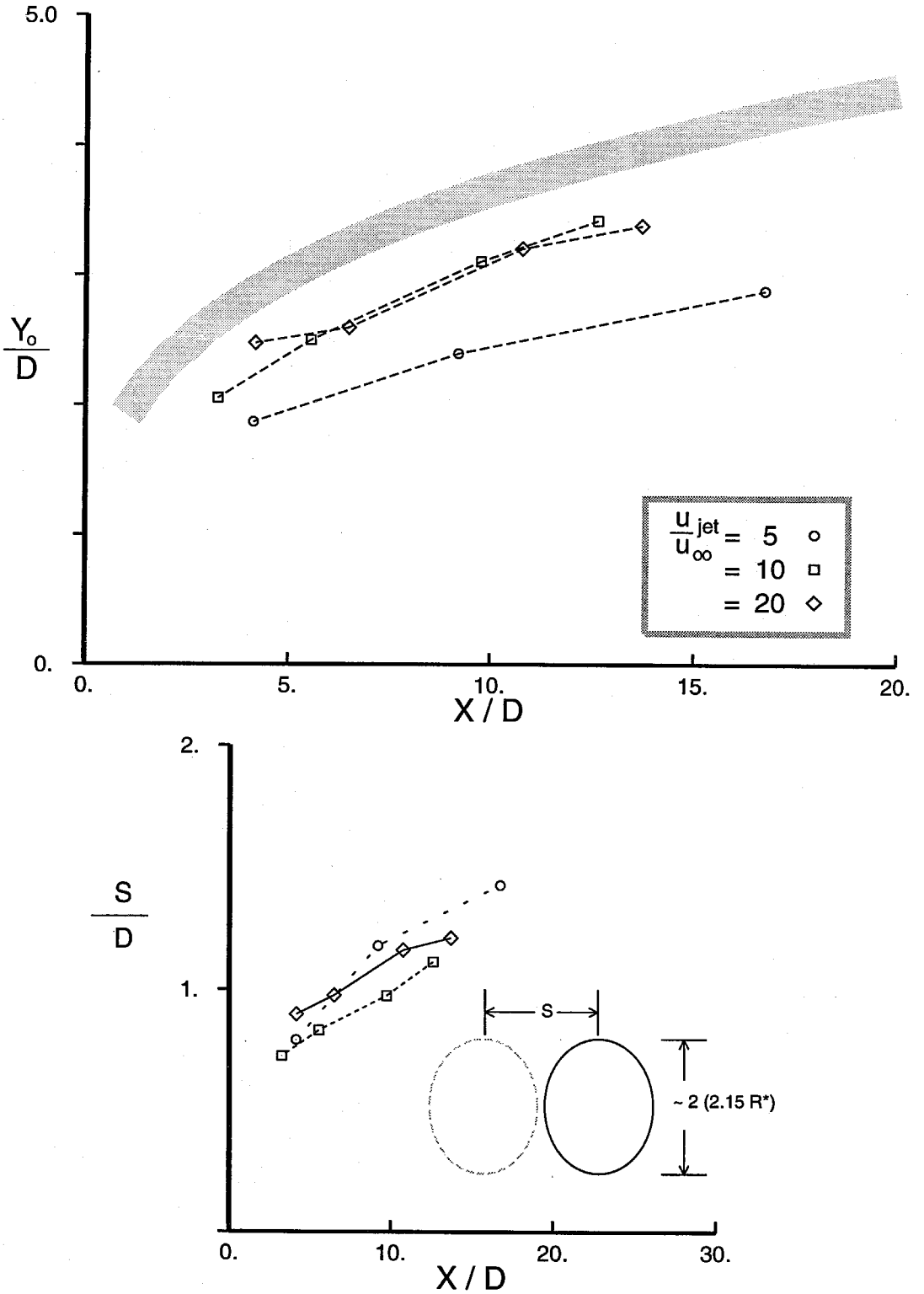

Figure 40. Jet trajectory and vortex separation in global variables.

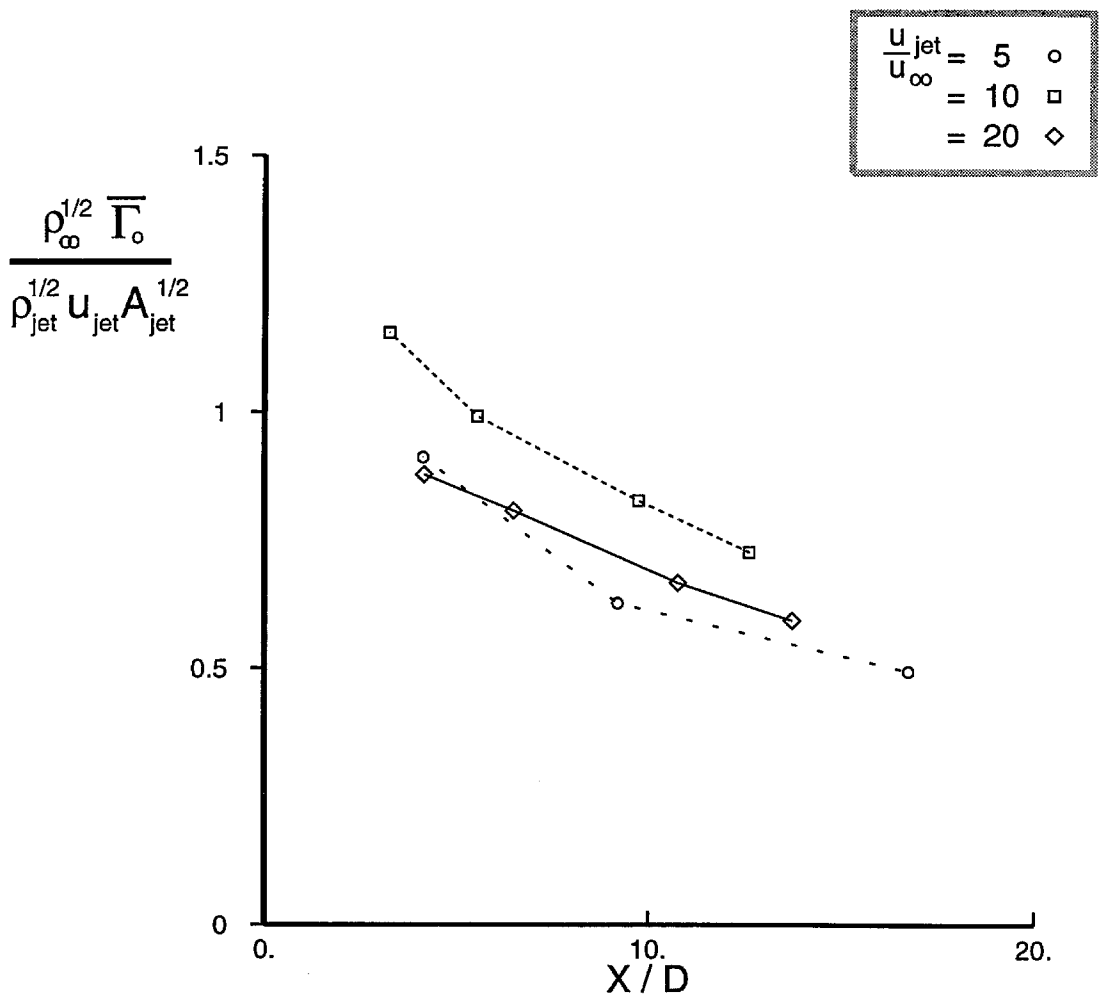

Figure 41. Normalized average circulation.